

Technical University of Munich  
Physics Department

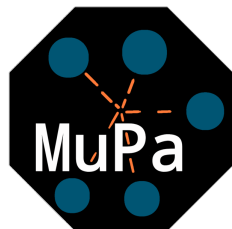
Master's Thesis

---

**Analyses of  
Symmetry Plane Correlations  
in Pb–Pb Collisions at 2.76 TeV  
with ALICE at the LHC**

---

by  
Marcel Lesch



September 2021

Themensteller: Dr. Ante Bilandzic  
Supervisor: Dr. Ante Bilandzic  
Abgabedatum: 30. September 2021

*“Everything is Gaussian if you’re brave enough”*  
*-Me*



# Abstract

With the advent of large-scale, high-energy particle accelerators like the Relativistic Heavy Ion Collider (RHIC) or the Large Hadron Collider (LHC), the study of ultrarelativistic heavy-ion collisions became feasible. Such collisions are of particular interest, as they produce an extreme state of matter of deconfined quarks and gluons, called the quark–gluon plasma. This state of matter is characterized by the collective phenomena of the produced particles and its behaviour resembles the properties of a perfect liquid. The study of these collective phenomena are nowadays to a great extent built on the so-called flow amplitudes  $v_n$  and symmetry planes  $\Psi_n$ . Both of these quantities are used as two distinct degrees of freedom in the Fourier series expansion, which is utilized to parametrize the anisotropic distribution of azimuthal angles of the produced particles. While analysis techniques for the flow amplitudes  $v_n$  have advanced over the past years, the observables used for measuring symmetry planes  $\Psi_n$  are often plagued by built-in biases.

After a short explanation of heavy-ion collisions and the phenomenon of anisotropic flow as a transfer of anisotropy from coordinate to momentum space via thermalized medium, this thesis discusses a recently developed analysis technique for the measurement of symmetry plane correlations. This so-called Gaussian Estimator is shown to reduce the bias present in the previous approaches, and thus providing a more precise technique for the studies of symmetry plane correlations. In addition to that, a new conceptual approach of utilizing cumulants of symmetry planes is presented as well.

Employing the newly developed Gaussian Estimator, the first experimental results of symmetry plane correlations are presented for Pb–Pb collisions at  $\sqrt{s_{NN}} = 2.76$  TeV. The data used in this analysis has been recorded by the ALICE experiment in 2010. With simulated data from the HIJING Monte Carlo generator, it is shown that this analysis technique is not biased by contributions from few particle correlations and is thus only sensitive to the collective evolution of the system. In addition to this, a careful analysis of systematic effects on the analysis is conducted. The final experimental results are compared to state-of-the-art theoretical predictions for the initial coordinate space provided by the T<sub>R</sub>ENTo model and for the momentum space obtained with iEBE-VISHNU. Together with these predictions, an interpretation of the results in terms of linear and non-linear response is given.



# Contents

<b>1</b>	<b>Introduction</b>	<b>1</b>
1.1	The Standard Model . . . . .	1
1.2	Quantum chromodynamics . . . . .	2
1.3	Quark–gluon plasma . . . . .	4
1.4	Heavy-ion collisions . . . . .	5
<b>2</b>	<b>Flow</b>	<b>9</b>
2.1	Anisotropic flow . . . . .	9
2.1.1	Description of the initial state . . . . .	9
2.1.2	Description of the final state . . . . .	11
2.1.3	From initial to final state: linear and non-linear response . . . . .	12
2.2	From azimuthal angles to flow observables . . . . .	13
2.3	Multiparticle correlation techniques . . . . .	15
2.3.1	Single-event averages . . . . .	15
2.3.2	All-event averages . . . . .	16
2.4	Flow vs non-flow . . . . .	17
2.5	Summary of important experimental results in flow . . . . .	18
<b>3</b>	<b>Theoretical models</b>	<b>21</b>
3.1	Glauber model . . . . .	21
3.1.1	MuPa Glauber model . . . . .	22
3.1.2	Centrality determination . . . . .	23
3.2	T <sub>RENT</sub> o . . . . .	23
3.3	iEBE-VISHNU . . . . .	24
3.4	HIJING . . . . .	25
<b>4</b>	<b>Experimental setup</b>	<b>27</b>
4.1	LHC . . . . .	27
4.2	ALICE . . . . .	28
4.2.1	ITS . . . . .	30
4.2.2	TPC . . . . .	30
4.2.3	V0 . . . . .	31
<b>5</b>	<b>New technical developments for symmetry plane correlations</b>	<b>33</b>
5.1	New estimator for SPC . . . . .	33
5.1.1	Ideal measurement of SPC . . . . .	33
5.1.2	Gaussian Estimator . . . . .	34
5.1.3	Validation of the Gaussian Estimator . . . . .	36
5.2	Cumulants of SPC . . . . .	39

5.2.1	Conceptual introduction to cumulants . . . . .	39
5.2.2	Cumulant formalism according to Kubo . . . . .	39
5.2.3	New formalism for cumulants of SPC . . . . .	41
<b>6</b>	<b>Experimental data analysis</b>	<b>47</b>
6.1	Event selection . . . . .	47
6.1.1	Primary vertex selection . . . . .	47
6.1.2	Triggering, centrality and multiplicity selection . . . . .	49
6.1.3	Removal of the high multiplicity outliers . . . . .	50
6.2	Track selection . . . . .	50
6.2.1	Reconstruction selection . . . . .	51
6.2.2	Kinematic cuts . . . . .	52
6.3	Weights . . . . .	54
6.4	Final quality assurance . . . . .	55
6.5	Non-flow estimation . . . . .	57
6.6	Statistical errors . . . . .	58
6.7	Systematic checks . . . . .	60
<b>7</b>	<b>Experimental results and discussion</b>	<b>63</b>
<b>8</b>	<b>Summary</b>	<b>71</b>
<b>A</b>	<b>Basics of flow</b>	<b>73</b>
A.1	Proof of $\langle \exp[in(\varphi - \Psi_n)] \rangle = v_n$ . . . . .	73
A.2	Importance of the isotropy condition . . . . .	74
A.3	P.D.F. characteristics . . . . .	75
<b>B</b>	<b>Supplements for new formalisms for SPC</b>	<b>77</b>
B.1	Choice of correlators in the GE . . . . .	77
B.1.1	Correlators between two symmetry planes . . . . .	78
B.1.2	Correlators between three symmetry planes . . . . .	79
B.2	Cumulant properties of CSC . . . . .	79
B.2.1	Statistical independence . . . . .	80
B.2.2	Reduction . . . . .	80
B.2.3	Semi-invariance . . . . .	80
B.2.4	Homogeneity . . . . .	80
B.2.5	Multilinearity . . . . .	80
<b>C</b>	<b>Non-flow studies</b>	<b>81</b>
<b>D</b>	<b>Statistical error propagation</b>	<b>85</b>
D.1	Errors of one-dimensional variables . . . . .	85
D.2	General error propagation . . . . .	87
D.3	SPC specific error propagation . . . . .	89
<b>E</b>	<b>Supplements data analysis</b>	<b>91</b>
E.1	Run-by-run trending . . . . .	91
E.2	Comparison of statistical errors . . . . .	92
E.3	Systematic Errors . . . . .	96

**F Supplements experimental results** **103**  
F.1 Comparison between ALICE and ATLAS data . . . . . 103



# Chapter 1

## Introduction

### 1.1 The Standard Model

<sup>1</sup>Introduced in the 1970s, the Standard Model (SM) of particle physics is currently the most successful model in describing the interaction of particles (despite missing gravity). Its elementary constituents are the quarks, leptons and mediator particles (see Fig. 1.1). The quarks and leptons are fermions with spin  $\frac{1}{2}$ . There exist six different leptons, which

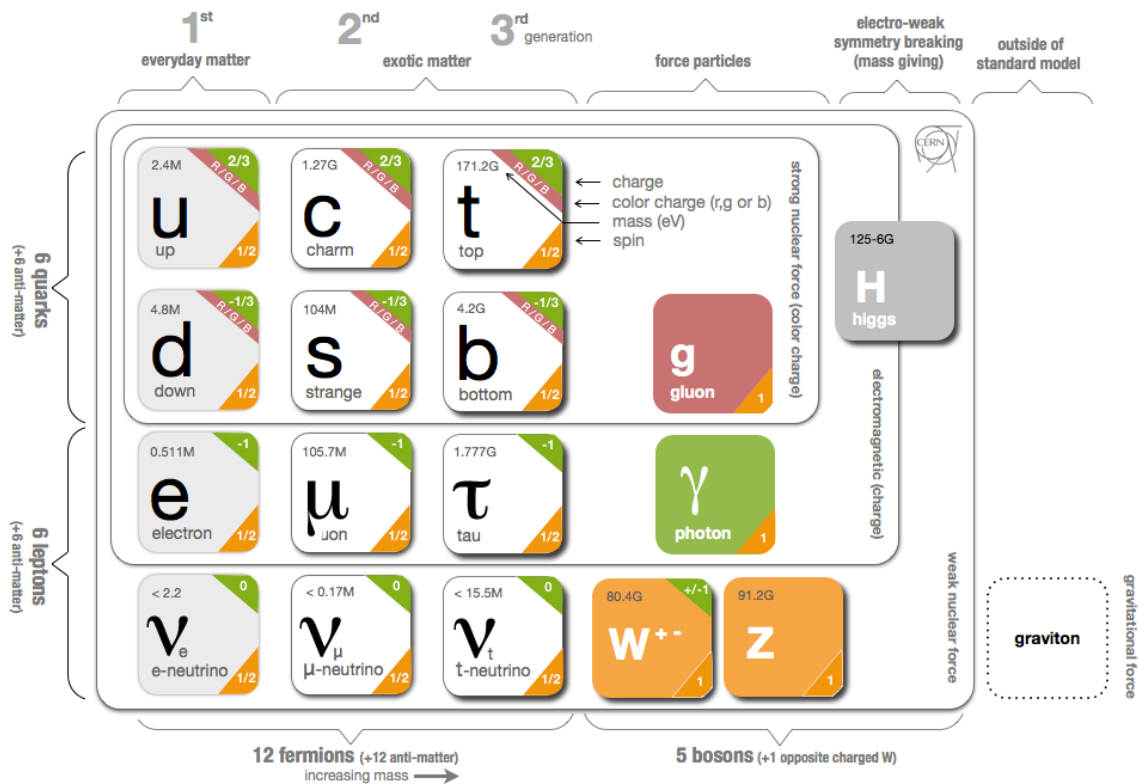


Figure 1.1: Overview of the Standard Model of Particle Physics, taken from [2].

are classified by their charge  $Q$  and their leptonic number (the electron  $L_e$ , muon  $L_\mu$  and tau  $L_\tau$  number). The six flavours of quarks are classified by their charge  $Q$  as well as their strangeness  $S$ , charm  $C$ , beauty  $B$  and truth  $T$ . In total, the fermions of the SM are combined into three generations (also called families). Each generation consists of a

<sup>1</sup>Unless indicated otherwise, this section is based on [1].

quark with charge  $\frac{2}{3}$ , a quark of charge  $-\frac{1}{3}$ , a lepton with charge  $-1$  and its corresponding neutrino - a massless, uncharged lepton. As such, the first family consists of the up quark  $u$  (charge  $\frac{2}{3}$ ), the down quark  $d$  (charge  $-\frac{1}{3}$ ), the electron  $e$  (charge  $-1$ ) and the electron neutrino  $\nu_e$ . In the same ordering, the second generation is made up of the charm quark  $c$ , the strange quark  $s$ , the muon  $\mu$  and the muon neutrino  $\nu_\mu$ , while the third generation consists of the top quark  $t$ , the bottom quark  $b$ , the tau  $\tau$  and the  $\tau$  neutrino.

For each quark and lepton, there exists a corresponding antiparticle with a reversed sign for the charge as well as for the leptonic number in case of leptons. Considering the quarks, their respective antiparticles have opposite strangeness, charm, beauty and truth. Therefore, the SM considers in total 12 different leptons as well as 12 different quarks.

The interactions of these particles are described via the exchange of the mediators, which are bosons with spin 1. The photon  $\gamma$  is the mediator of the electromagnetic force, while the  $W^+$ ,  $W^-$  and  $Z^0$  bosons are the exchange particles for the weak interaction. The strong force, which will be explained in more detail in Sec. 1.2, has the so-called gluons  $g$  as carriers. Additionally, since its experimental discovery in 2012 by the CMS and ATLAS Collaborations at CERN [3, 4], the in 1964 proposed Higgs boson  $H^0$  [5, 6, 7, 8] has officially been confirmed as a part of the SM. This spin 0 particle, describes how all the fundamental particles within the SM obtain their mass.

Despite its great successes, it is known that the SM is not complete. For instance, gravity — which is one of the four fundamental forces — is not included in the SM. Other phenomena that are not described by the SM are the neutrino oscillations (which can be explained by a non-zero neutrino mass [1]) or the so-called Dark Matter, whose existence is indirectly observed by the measurement of rotation curves of galaxies (see e.g. [9]).

## 1.2 Quantum chromodynamics

<sup>2</sup>Within the SM, the strong nuclear force is on its most fundamental level described by *quantum chromodynamics* (QCD). The name “chromodynamics” is a reference to the associated charge of the strong force — the so-called *color*. Quarks carry a single positive color charge, which can take one of three possibilities (red, blue or green), while antiquarks carry a single negative color, also called anticolor (anti-red, anti-blue or anti-green). As the color is a conserved quantity in QCD, the gluons have to carry away the color difference when a quark changes its color within a strong interaction. Therefore, gluons have to carry both a color and an anticolor, and are as such bicolored.

Due to this non-zero color charge that the gluons carry, they can themselves interact with other gluons and even form particles consisting purely of gluons, which are called glueballs. A recent study [10] reported the discovery of the odderon - a exclusive three-gluon state that was predicted in 1973 [11].

In addition to the formation of glueballs, the gluon-gluon self-interactions have further consequences for the strong interaction. Due to these, virtual gluon-loops can form between the main interaction vertices of strongly interacting particles. This ultimately leads to the *running of the strong interaction constant*  $\alpha_s$ , which was theoretically studied in [13, 14, 15] and awarded the Nobel prize in 2004. It describes that  $\alpha_s$  is small (i.e. the strong interaction is weak) at small separation distances  $R$  (or equivalently high energies) and becomes stronger with increasing distance  $R$  (or at lower energies, see Fig. 1.2). This phenomenon is called *asymptotic freedom* and it is contrary to the effects observed in the electromagnetic interaction, which is described by quantum electrodynamics (QED). In

---

<sup>2</sup>Unless indicated otherwise, this section is based on [1].

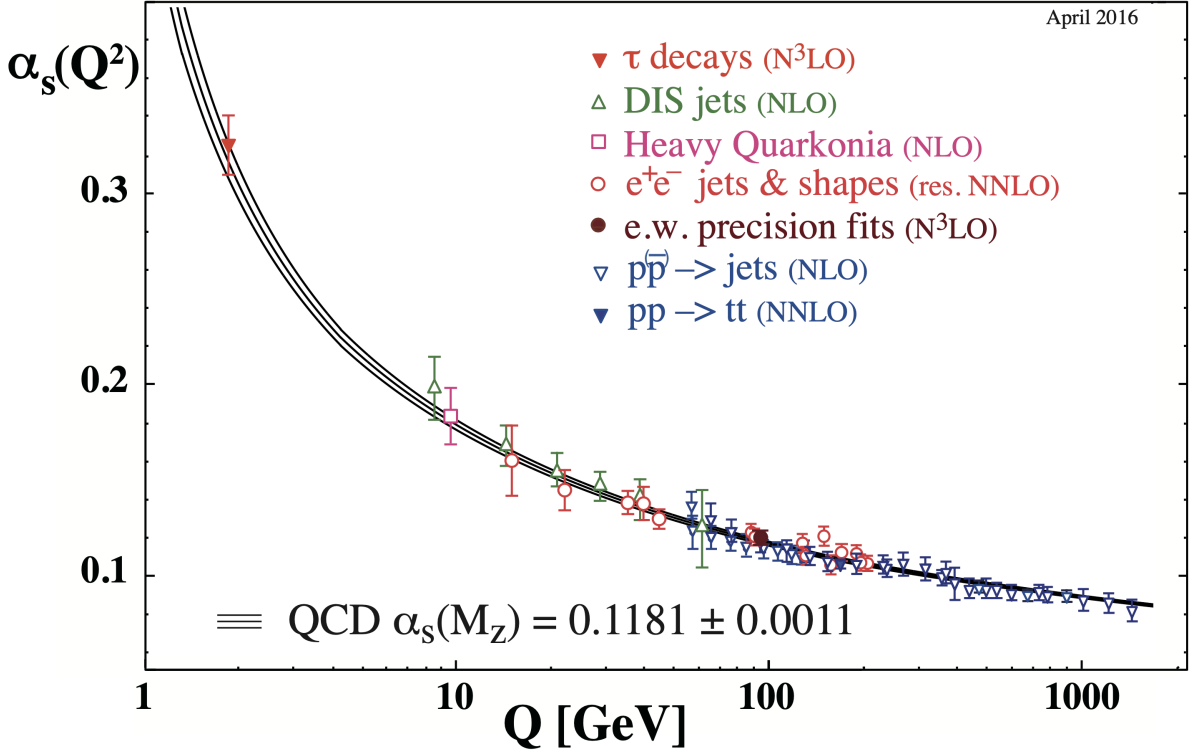


Figure 1.2: Strong coupling constant  $\alpha_s$  as a function of the energy scale  $Q$ , taken from [12].

QED, virtual electron-positron loops lead to a screening effect of the charges and therefore to a depletion of the electromagnetic constant with rising distance. While virtual quark–antiquark pairs lead to a similar depletion of  $\alpha_s$  with increasing distance due to screening effects of the color, the described gluon loops drive  $\alpha_s$  up at the same time and dominate the effect, leading to the increase of  $\alpha_s$  with increasing  $R$ . An additional phenomenon associated with the strong force is the *confinement*, which describes that, in nature, only color-neutral particles can be observed. As such, quarks can be found in either a color-neutral quark–antiquark state, which is called a meson, or in a color-neutral state of three quarks, a so-called baryon. Consequently, quarks can never be observed isolated. These phenomena of the strong force are mathematically described by the QCD Lagrangian density [16]

$$\mathcal{L} = \bar{\psi}_i (i\gamma_\mu \mathcal{D}_{ij}^\mu - m\delta_{ij}) \psi_j - \frac{1}{4} \mathcal{F}_{\mu\nu\alpha} \mathcal{F}^{\mu\nu\alpha}. \quad (1.1)$$

Equation (1.1) contains the quark field  $\psi_i$  and the corresponding quark mass  $m$  as well as  $\mathcal{F}_\alpha^{\mu\nu}$  the field strength tensor of the gluons. Further,  $\gamma_\mu$  denotes the Dirac matrices,  $\mathcal{D}^\mu$  the covariant derivative and  $\delta_{ij}$  the Kronecker symbol. In this representation of the Lagrangian, natural units ( $\hbar = c = k_B = 1$ ) and the Minkowski metric ( $g^{\mu\nu} = \text{diag}(1, -1, -1, -1)$ ) have been used.

As a last important phenomenon of the strong interaction stands the so-called *chiral symmetry restoration*. The QCD Lagrangian in Eq. (1.1) is only invariant under chiral symmetry transformation in the limit of massless quarks. However, due to the non-zero mass of quarks, chiral symmetry is broken explicitly. Additionally, due to the presence of quark-antiquark pairs in the QCD “vacuum” (also called  $q\bar{q}$  condensate), the ground state of the QCD Lagrangian breaks the chiral symmetry as well. This is referred to as the dynamic breaking [17]. The chiral symmetry can, however, be restored in very hot (or

dense) environments [18], such as the quark–gluon plasma (QGP), which will be described in more details in the next section.

### 1.3 Quark–gluon plasma

The running of the strong coupling constant  $\alpha_s$  is the key phenomenon behind many important properties of strongly interacting matter. In 1978, Edward Shuryak [19] theorised that there might exist an environment, in which the asymptotic freedom of the quarks allows a state of matter consisting of deconfined quarks and gluons. This state of matter was then called the *quark–gluon plasma*. The QGP has already been of huge interest as many people suggested the presence of a deconfined phase of quarks and gluons inside a neutron star [20] due to the high densities inside the core. Besides that, the QGP is expected to be one of the initial stages of matter a few microseconds after the Big Bang, thus playing a key role in the physics and evolution of the Early Universe [21, 22]. Lastly, as it has been shown in Sec. 1.2, in very hot environments, the restoration of chiral symmetry is expected which additionally contributes to the interest of the physics community in the QGP [23].

As depicted in Fig. 1.3, this state of matter exists at very high temperatures and/or high baryonic densities. In fact, a study of the MIT Bag Model [24] showed that the pressure of the  $q\bar{q}$  condensate, which is attributed to the confinement of quarks, can be overcome at a temperature of around 144 MeV [25]. At this point, the model predicts the existence of a gas of deconfined quarks. This is supported by recent lattice QCD calculations, which predict the occurrence of QGP at  $T = (154 \pm 9)$  MeV for low baryonic densities  $\mu \approx 0$  [26]. Most notably, the knowledge about the QGP has changed over the years. In the first years after its proposal, it was suspected that the QGP behaves like a gas, i.e. its constituents interact only weakly with each other. However, with the emergence of the first large scale hadron colliders like the Relativistic Heavy Ion Collider (RHIC) and the Large Hadron Collider (LHC), the experimental study of ultrarelativistic heavy-ion collisions became accessible. In such collisions, temperatures of about 300 MeV (for Pb–Pb at  $\sqrt{s_{NN}}$  of 2.76 TeV in 0–20% centrality) [27] are reached at low baryonic densities. A more detailed description of heavy-ion collision is provided in Sec. 1.4. The obtained experimental results show that the QGP does not behave like a gas, but rather like a strongly coupled fluid. In fact, it was found that the shear-viscosity of entropy density  $\eta/s$  of the QGP is extremely close to the universal lower boundary of  $1/4\pi$  provided in [28]. Thus, the QGP is found to be the most perfect fluid known so far.

Despite the various successes in the research about the QGP over the past years, many open questions remain. For example, the exact place of the phase transition within the phase diagram is yet to be determined, as is the existence of a critical point. Furthermore, the properties of the transition — whether it is a smooth crossover or for example a first order phase transition — are left unanswered as well. Programs like the beam energy scan at RHIC [30, 31], the study of heavy-ion collisions and collisions of lighter nuclei like xenon, or the planned oxygen-oxygen collisions [32] at the LHC try to provide new insights into these questions. In addition to the study of the QGP in new collision systems and at different collision energies, the development of new experimental observables is of greatest importance. The comparison of new experimental data to model predictions of the initial and final state of a heavy-ion collision can provide new important and independent information on the properties of the QGP. Additionally, these new observables can be used as an input to Bayesian analyses to constraint the properties of the QGP.

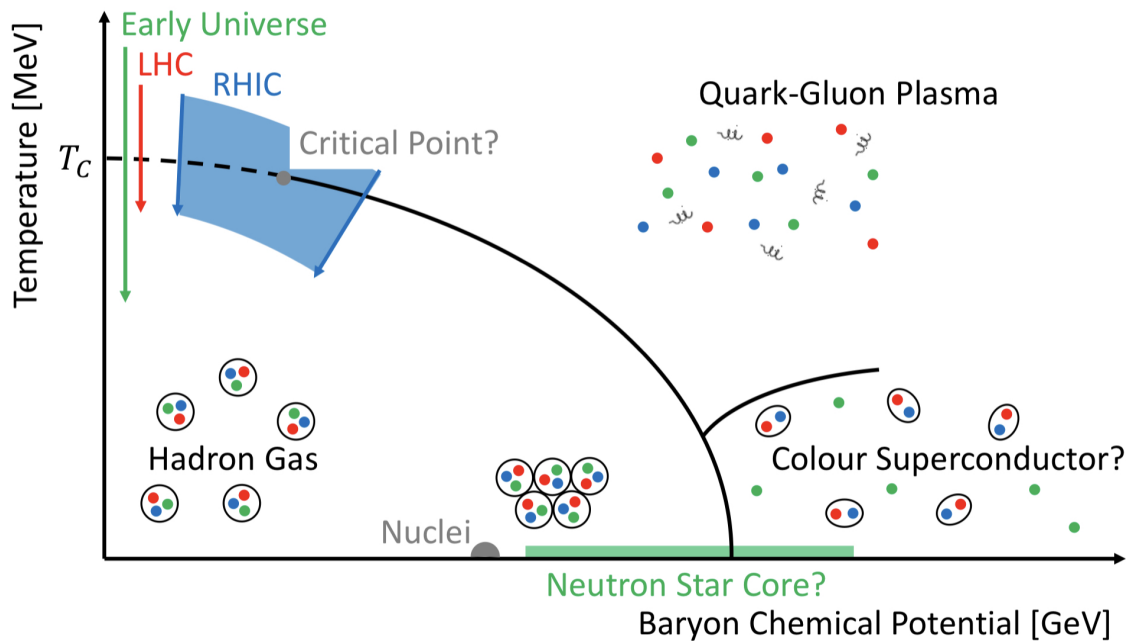


Figure 1.3: Sketch of the QCD phase diagram as a function of the system temperature and the baryon chemical potential, taken from [29].

## 1.4 Heavy-ion collisions

As described in Sec. 1.3 and shown in Fig. 1.3, the QGP is supposed to form at very large temperatures and low baryon densities. Such a condition can be experimentally produced in particle accelerators by the collision of ultrarelativistic heavy ions. These high-energy collisions, such as Pb–Pb at a centre of mass per nucleon pair  $\sqrt{s_{NN}}$  of 2.76 TeV at the LHC, reach effective temperatures of about 300 MeV [27]. In the collision process, the nucleons that collide with each other are destroyed and form the QGP, while the remaining fragments of the nuclei fly away fast from the point of collision. This results in a system with low baryon density.

To describe such a collision of two heavy ions, two main aspects have to be taken into account as both have a crucial influence on the measured signals: The geometry of the initial stage as well as the time evolution of the system. A schematic description of the basic collision geometry and its relevant quantities is provided in Fig. 1.4. There, the *beam axis* along which the two heavy ions travel is referred to as  $z$ . The vector pointing from the centre of one nucleus to the other in the plane transverse to the beam axis is referred to as the *impact parameter vector*  $\vec{b}$  [33]. The magnitude of  $\vec{b}$  is called the *impact parameter*  $b$  and it determines how much the two colliding nuclei overlap. Collisions with  $b = 0$  are called head-on. Events with small impact parameter are in general referred to as central, while collisions with large impact parameter (i.e. the nuclei only have small overlapping region) are called peripheral.

Experimentally, the impact parameter is not accessible. However, it is related to the amount of produced particles in the event, also called the *multiplicity*. In general, the multiplicity of head-on collisions is much greater than it is for peripheral collisions. Experiments thus classify events by the so-called *centrality*  $c$ , where for instance a centrality of 5% stands for the 5% of events with the highest multiplicities (see Fig. 1.5). Using

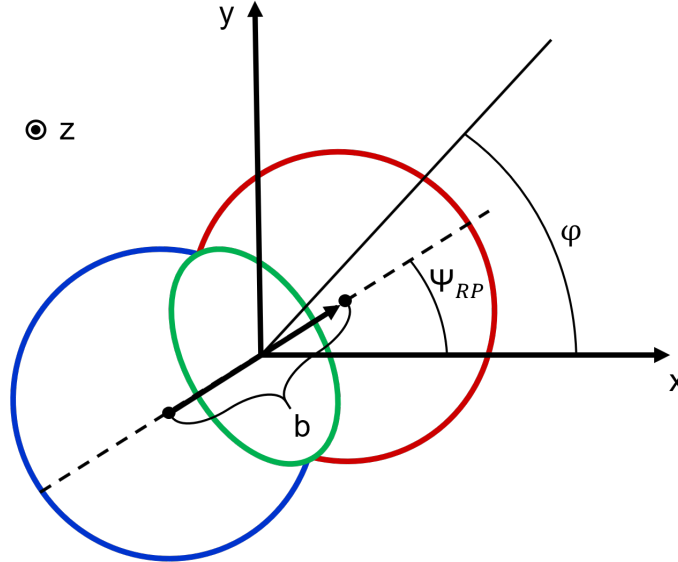


Figure 1.4: Sketch of the basic collision geometry of two heavy ions in the transverse plane perpendicular to the beam axis  $z$ . The impact parameter  $b$  and the reaction plane angle  $\Psi_{RP}$  fully describe the basic geometry.

the total inelastic nucleus-nucleus cross-section  $\sigma_{inel}$ , an approximate relation between the centrality  $c$  and the impact parameter  $b$  is given by [34]

$$c \approx \frac{\pi b^2}{\sigma_{inel}}. \quad (1.2)$$

The impact parameter vector spans together with the beam axis the so-called *reaction plane*, whose orientation in respect to the  $x$ - $z$  plane of the laboratory frame is characterised by the *reaction plane angle*  $\Psi_{RP}$  [33]. The nucleons that collide with each other (i.e. nucleons within the green ellipse in Fig. 1.4) are referred to as *participants*, while nucleons which do not undergo any collision are called *spectators*.

The orientation of the impact parameter vector  $\vec{b}$  and thus  $\Psi_{RP}$  fluctuate randomly in each event. In theoretical studies this is not of any concern, as most models provide a notion of  $\Psi_{RP}$  or fix this angle within the model to a specific value. Experimentally however, the reaction plane angle is (like the impact parameter) not directly accessible and can therefore not be easily accounted for [33]. Therefore, any experimental observables that involve the azimuthal angle  $\varphi$  of emitted particles has to be rotationally invariant under a random shift by  $\Psi_{RP}$ . The importance of this will be explained in more detail in Sec. 2.2.

Besides this basic geometrical description of the collision, one has to take into account that the colliding nuclei are built out of protons and neutrons. As such, the overlapping region of heavy-ion collisions is not perfectly elliptical as it is shown in Fig. 1.4. To describe the initial geometry of the collision more realistically, one (at least) has to take the nucleons within the nuclei and their fluctuating positions into account. Including this leads to a more complex picture in which the initial geometry is not fully described by an elliptic overlapping region. Additional shapes of higher order  $n > 2$ , whose orientation with respect to the  $x - z$  plane are characterised by their *participant plane*  $\Phi_n$ , have to be taken into account (see Fig. 1.6) [33]. A more detailed description of these angles is provided in Sec. 2.1.

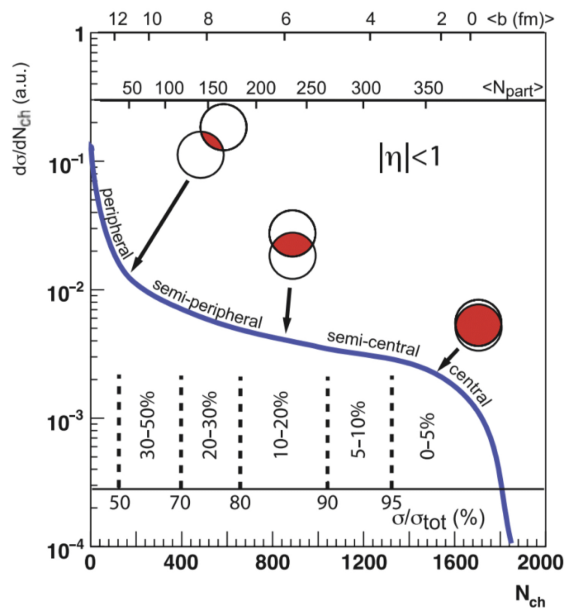


Figure 1.5: Exemplary normalized multiplicity distribution of heavy-ion collisions and the categorisation by centrality, taken from [35].

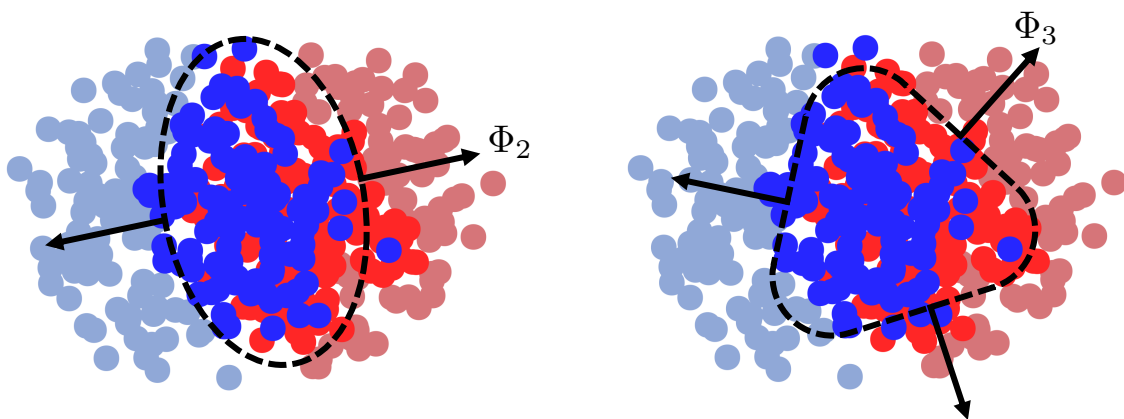


Figure 1.6: Ellipticity and triangularity in the initial stage of a heavy-ion collision. Figure obtained with the output of the MuPa Glauber model (see Sec. 3.1), inspired from [36].

There are various models which take such initial stage fluctuations into account with different levels of complexity. One of the most commonly used initial stage models is the Glauber model [37], which will be explained in greater detail in Sec. 3.1.

As explained before, besides the geometry of the initial collision, the time evolution of the system plays a crucial role in the final state that can be experimentally observed. The typical time evolution of a heavy-ion collision is depicted in Fig. 1.7. After the collision of the two heavy ions, the system is shortly in an out of equilibrium state. Already in this early stage, hard processes (which are characterized by large transferred momenta  $Q > 10$  GeV/ $c$ ) can occur [38]. The particles resulting from these processes (e.g. hadronic jets or direct photons) have energies and transverse momenta of the order of  $Q$ . With the formation of the thermal equilibrium at a proper time  $\tau \approx 1$  fm/ $c$ , the QGP phase is reached and the system continues to expand [39]. This expansion can be described by relativistic hydrodynamics as it was found in various studies [23, 40] by comparison of theoretical predictions to experimental data. During the expansion, the system cools down and at a time of about  $\tau \approx 10$  fm/ $c$  [38] hadronization will start leading to a gas

of hadrons. As the system still has a high temperature, the produced hadrons undergo inelastic collisions. This goes on till the system cools down that much, that the point of chemical freeze-out with a temperature  $T_{chem}$  is reached at  $\tau \approx 20$  fm/c [38]. Then, any inelastic collisions cease and the particle composition does not change further. However, elastic collisions still occur leading to a momentum transfer between the particles. At the point of kinematic (or thermal) freeze-out, which is characterized by the temperature  $T_{kin}$ , the elastic processes stop and the produced particles travel freely to the detector.

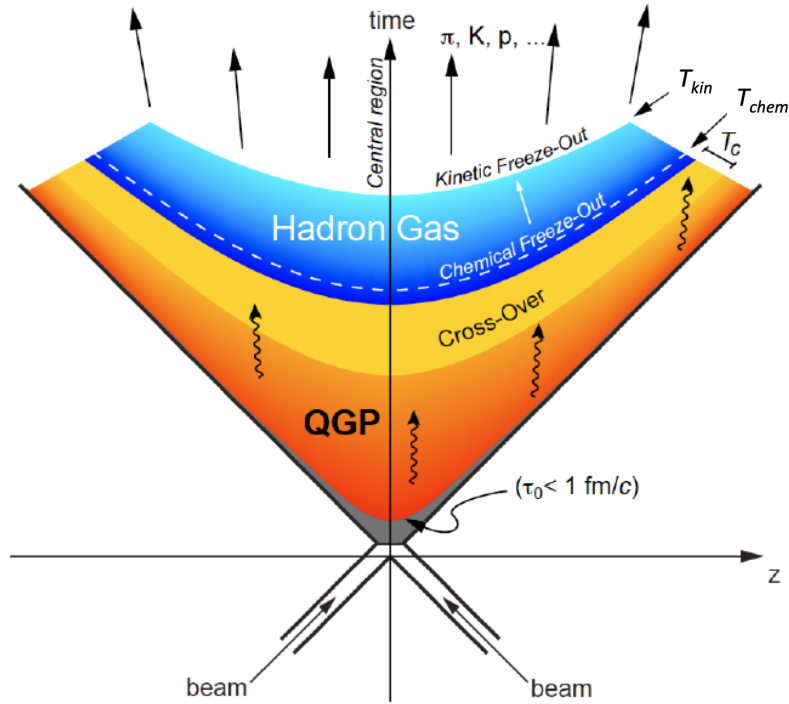


Figure 1.7: Evolution of a heavy-ion collision in space-time diagram. The ions collide at  $\tau = 0$  at a longitudinal position  $z = 0$ . Taken from [39].

# Chapter 2

## Flow

### 2.1 Anisotropic flow

Considering that the QGP is one of the earliest stages of a heavy-ion collision (see Sec. 1.4), the question on how to infer on its properties from the finally measured particles inevitably arises. Indeed, there are many physical phenomena to study the system properties such as jet quenching [41, 42] or strangeness enhancement [43].

However, the focus here lies on the phenomenon of *anisotropic flow*. In non-central heavy-ion collisions, the overlapping region and thus the initial energy distribution in coordinate space is, to leading order, elliptical and as such anisotropic. This initial anisotropy leads to anisotropic pressure gradients inside the medium if — and only if — the medium thermalized, i.e. the QGP was formed. Thus, the coordinate space anisotropy is transferred into an anisotropy in momentum space. Consequently, the particles that stem from the collision will have a non-uniform distribution in azimuthal angles (see Fig. 2.1). Therefore, anisotropic flow can be investigated experimentally by studying those distributions and one can infer on the properties of the QGP as it will be further explained in this section.

#### 2.1.1 Description of the initial state

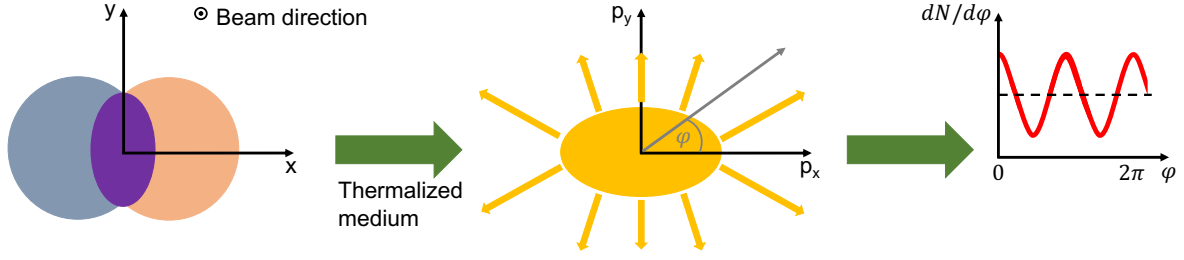
In order to quantify the description of anisotropic flow given above, one traditionally describes the anisotropy in coordinate space by the so-called *eccentricities*  $\mathcal{E}_n$

$$\mathcal{E}_n = \epsilon_n e^{in\Phi_n}, \quad (2.1)$$

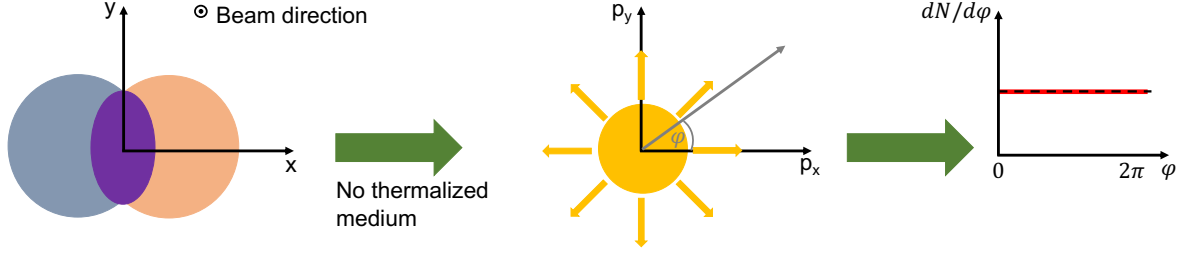
where  $\epsilon_n$  is the magnitude of the  $n^{\text{th}}$  order asymmetry and  $\Phi_n$  the *participant planes*. By definition,  $\epsilon_2$  corresponds to the ellipticity,  $\epsilon_3$  to the triangularity and so forth. The participant planes provide the phase (or orientation) of these higher order asymmetries (see Fig. 1.6). As it was briefly explained in Sec. 1.4, the fact that the colliding nuclei are built of protons and neutrons with fluctuating positions consequently leads to the emergence of eccentricities of higher orders. The most commonly used mathematical definition of the eccentricities is given by [44]

$$\mathcal{E}_n = \epsilon_n e^{in\Phi_n} = \begin{cases} -\frac{\{r^3 e^{in\varphi}\}}{r^3} & \text{for } n = 1 \\ -\frac{\{r^n e^{in\varphi}\}}{r^n} & \text{for } n > 1 \end{cases} \quad (2.2)$$

where  $r$  and  $\varphi$  are the transverse coordinates which are used in the average  $\{\dots\} = \int r dr d\varphi e(r, \varphi)$  over the initial energy density distribution  $e(r, \varphi)$ . An alternative approach



(a) A system where the medium thermalized. The geometrical anisotropy translated into an anisotropy in momentum space, resulting in an anisotropic distribution of azimuthal angles.



(b) A system with no thermalized medium and thus no anisotropic flow. The distribution of azimuthal angles is flat.

Figure 2.1: Examples of a system in which flow did (a) and did not (b) evolve, inspired by [16].

to characterise the initial state was first introduced by Teaney and Yan in [45] and studied further in [46, 47]. This approach deviates from the traditional description of the initial state via its moments, i.e. the eccentricities, but characterises it rather by the cumulants of energy density. Here, these cumulants of energy density will be denoted by the complex number  $C_n$

$$C_n = c_n e^{in\phi_n}, \quad (2.3)$$

where  $c_n$  is its magnitude and  $\phi_n$  its phase, i.e. its participant plane. By slightly adjusting the notation in [48], the first four complex cumulants of energy density can be expressed as

$$\begin{aligned} C_2 &= c_2 e^{i2\phi_2} = \epsilon_2 e^{i2\Phi_2} \\ C_3 &= c_3 e^{i2\phi_3} = \epsilon_3 e^{i3\Phi_3} \\ C_4 &= c_4 e^{i2\phi_4} = \epsilon_4 e^{i4\Phi_4} + 3 \left( \frac{\{r^2\}^2}{\{r^4\}} \right) \epsilon_2^2 e^{i4\Phi_2} \\ C_5 &= c_5 e^{i2\phi_5} = \epsilon_5 e^{i5\Phi_5} + 10 \left( \frac{\{r^2\}\{r^3\}}{\{r^5\}} \right) \epsilon_2 \epsilon_3 e^{i2\Phi_2} e^{i3\Phi_3}. \end{aligned} \quad (2.4)$$

It becomes evident that  $C_2$  and  $C_3$  correspond to the eccentricity  $\mathcal{E}_2$  and  $\mathcal{E}_3$  respectively, while for higher orders additional terms appear. Therefore,  $C_4$  has a non-linear contribution from  $\mathcal{E}_2^2$  and  $C_5$  from  $\mathcal{E}_2 \mathcal{E}_3$ . The advantage of these cumulants of energy density compared to the traditional eccentricities is that higher order eccentricities contain lower order contributions, which are removed in the cumulants of energy density. For example, using a Gaussian shape as the initial state, one would expect to only find ellipticity [45]. However, also a fourth order moment can be found in this case simply due to the residual contribution of the ellipticity. This lower order contribution is removed in the cumulant approach, therefore the fourth order asymmetry is zero.

### 2.1.2 Description of the final state

On the other hand, the distribution of the final state is characterised by the so-called *flow amplitudes*  $v_n$  and *symmetry planes*  $\Psi_n$ , with again  $n$  referring to the order. Most commonly,  $v_1$  is called directed flow,  $v_2$  elliptical flow,  $v_3$  triangular flow, etc. These final state quantities can be combined into the complex flow harmonic  $V_n$ , which is defined as

$$V_n = v_n e^{in\Psi_n}. \quad (2.5)$$

Using the flow amplitudes and symmetry planes, one can describe the distribution of particles in momentum space as [49]

$$E \frac{d^3N}{d^3\mathbf{p}} = \frac{d^3N}{p_T dp_T d\eta d\varphi} = \frac{1}{2\pi} \frac{d^2N}{p_T dp_T d\eta} \left[ 1 + 2 \sum_{n=1}^{\infty} v_n(p_T, \eta) \cos[n(\varphi - \Psi_n)] \right]. \quad (2.6)$$

Equation (2.6) represents the Lorentz-invariant distribution of particles where  $E$  is the energy and  $\mathbf{p}$  the three-momentum of the particles. As seen in Eq. (2.6), this distribution can be rewritten in terms of the transverse momentum  $p_T$ , the pseudorapidity  $\eta$  and the azimuthal angle  $\varphi$ . Most notably, in Eq. (2.6) a Fourier series consisting of the flow amplitudes and symmetry planes is used to describe the anisotropy in the transverse plane, i.e. the anisotropy in the distribution of azimuthal angles  $dN/d\varphi$ . In general,  $v_n$  depend on  $p_T$ ,  $\eta$  and the species of the particles. Therefore,  $v_n(p_T, \eta)$  is called  *$n^{\text{th}}$  order differential flow* [50, 51]. Considering the averaged value of  $v_n$  over  $p_T$ ,  $\eta$  and particle species, one generally speaks of  *$n^{\text{th}}$  order integrated flow* [52], which will be denoted by  $v_n$ . As the integrated flow has no dependence on  $p_T$  and  $\eta$  besides the integration boundaries, the single event particle distribution simplifies into the Fourier series

$$\frac{dN}{d\varphi} = \frac{M}{2\pi} \left[ 1 + 2 \sum_{n=1}^{\infty} v_n \cos[n(\varphi - \Psi_n)] \right], \quad (2.7)$$

which is a distribution purely for the azimuthal angle  $\varphi$  in the transverse plane. In Eq. (2.7),  $M$  denotes the multiplicity of an event. Additionally it has to be stressed, that the symmetry planes are rotationally invariant under the operation

$$\Psi_n \rightarrow \Psi_n + \frac{2\pi}{n}, \quad (2.8)$$

which becomes evident by the definition of the  $\Psi_n$  within the Fourier series Eq. (2.6) itself. Most importantly, the described phenomenon of flow affects all particles, which are emitted from the common source — the QGP — in an independent way. It is therefore a genuine multiparticle collective effect. Assuming that  $M$  final state particles are emitted independently from the source and that there are no other correlations between them, one can thus factorise the common multiparticle probability density function (p.d.f.)  $f(\varphi_1, \varphi_2, \dots, \varphi_M)$  as

$$f(\varphi_1, \varphi_2, \dots, \varphi_M) = f_{\varphi_1}(\varphi_1) f_{\varphi_2}(\varphi_2) \dots f_{\varphi_M}(\varphi_M). \quad (2.9)$$

In the latter equation,  $f_{\varphi_i}(\varphi_i)$  stands for the single-particle p.d.f., which can be obtained by proper normalisation of Eq. (2.7). This factorisation property in the context of anisotropic flow will be exploited in Sec. 2.3 where the technical details of measuring flow are discussed.

### 2.1.3 From initial to final state: linear and non-linear response

Given the description of eccentricities and flow harmonics above, the relation between them is governed by the so-called *linear and non-linear response*. Considering a flow harmonic  $V_n$ , it can be a general function of the eccentricities [44], i.e.

$$V_n = V_n(\mathcal{E}, \alpha), \quad (2.10)$$

where  $\alpha$  contains the dynamic medium properties, for instance the shear viscosity over entropy density  $\eta/s$ . In general, the response of  $V_n$  to the eccentricity of the same order  $\mathcal{E}_n$  is referred to as *linear response*, while the dependence of  $V_n$  to (a combination of) lower order eccentricities is called *non-linear response*. As the exact form of the relation between  $V$  and  $\mathcal{E}$  is not known, an expansion of the form

$$V_n = \kappa(\alpha)\mathcal{E} + \mathcal{O}(\mathcal{E}^2) + \delta_n \quad (2.11)$$

is made [44]. In Eq. (2.11), the complex number  $\delta_n$  is introduced to capture additional fluctuations and is by assumption not directly related to the initial state. The expansion in Eq. (2.11) is justified if the involved  $\mathcal{E}_n$  are small, which is generally satisfied in heavy-ion collisions. Additionally, the different dependences of the eccentricities  $\mathcal{E}_n$  on the medium properties are accounted for by the introduction of the individual expansion coefficients  $\kappa(\alpha)$ . As the flow harmonics  $V_n$  are rotationally invariant under the transformation

$$\Psi_n \rightarrow \Psi_n + \frac{2\pi}{n}, \quad (2.12)$$

the right side of the Eq. (2.11) has to be invariant under these transformations as well. Thus, the allowed combinations of eccentricities  $\mathcal{E}$  in the expansion are determined by this transformation invariance, given that the expansion coefficients  $\kappa(\alpha)$  are real numbers. Therefore, one finds for the first flow harmonics up to the sixth order the following leading order linear and non-linear responses [44]:

$$\begin{aligned} V_2 &= \kappa_2 \mathcal{E}_2 + \kappa'_2 \epsilon_2^2 \mathcal{E}_2 + \delta_2, \\ V_3 &= \kappa_3 \mathcal{E}_3 + \kappa'_{23} \epsilon_2^2 \mathcal{E}_3 + \delta_3, \\ V_4 &= \kappa_4 \mathcal{E}_4 + \kappa_{422} \mathcal{E}_2^2 + \delta_4, \\ V_5 &= \kappa_5 \mathcal{E}_5 + \kappa_{523} \mathcal{E}_2 \mathcal{E}_3 + \delta_5, \\ V_6 &= \kappa_6 \mathcal{E}_6 + \kappa_{633} \mathcal{E}_3^2 + \kappa_{624} \mathcal{E}_2 \mathcal{E}_4 + \kappa_{6222} \mathcal{E}_2^3 + \delta_6. \end{aligned} \quad (2.13)$$

It becomes evident that  $V_2$  and  $V_3$  exhibit only linear response while non-linear terms appear only for harmonics  $n > 3$ .

In particular, it is possible that the initial state does not contain a higher order event plane like  $\Phi_5$ , while the corresponding symmetry plane  $\Psi_5$  may exist due to the non-linear response the  $\Phi_2$  and  $\Phi_3$ .

Similar to the linear and non-linear response of the flow harmonics  $V_n$  to the eccentricities  $\mathcal{E}$ , the expansion can be performed on the cumulants of energy density  $C_n$  as it is shown in [48]. The first four expressions for the leading terms in response are thus

$$\begin{aligned} V_2 &= \omega_2 C_2, \\ V_3 &= \omega_3 C_3, \\ V_4 &= \omega_4 C_4 + \omega_{422} C_2^2, \\ V_5 &= \omega_5 C_5 + \omega_{523} C_2 C_3, \end{aligned} \quad (2.14)$$

where the subleading contributions have been neglected. Again,  $V_2$  and  $V_3$  exhibit only linear response to  $C_2$  and  $C_3$  while  $V_4$  and  $V_5$  have additional non-linear terms.

## 2.2 From azimuthal angles to flow observables

As presented in Sec. 2.1, the central formalism, which is used to describe anisotropic flow is the Fourier series Eq. (2.7). In fact, by proper normalisation this series can be seen as a probability density function (p.d.f.) for the particle emission at a certain azimuthal angle  $\varphi$ . For this section, this p.d.f. will be expressed as

$$f(\varphi) = \frac{1}{2\pi} \left[ 1 + 2 \sum_{n=1}^{\infty} v_n \cos[n(\varphi - \Psi_n)] \right]. \quad (2.15)$$

Additionally,  $\langle \cdot \cdot \cdot \rangle$  will be used to denote the single-event average, i.e. the average over the azimuthal angles of the particles of interest in *one* given event. Furthermore,  $\langle\langle \cdot \cdot \cdot \rangle\rangle$  denotes the average over all events.

Using this notation in addition to Eq. (2.15), one can show the following relation (see App. A.1 for details)

$$v_n = \langle \cos[n(\varphi - \Psi_n)] \rangle. \quad (2.16)$$

This result is, however, of limited importance as  $\Psi_n$  cannot be measured directly in the experiment. One method traditionally used for estimating  $\Psi_n$  is the so-called *event plane method* with

$$\Psi_n(EP) = \frac{1}{n} \arctan \left( \frac{\sum_i w_i \sin(n\varphi_i)}{\sum_i w_i \cos(n\varphi_i)} \right), \quad (2.17)$$

which was first introduced in [49]. In Eq. (2.17), the sum runs over the azimuthal angles  $\varphi$  of all measured particles weighted with  $w_i$  to optimize the experimental resolution. Despite this, the event plane method cannot reliably estimate a single symmetry plane  $\Psi_n$  within one event as the resolution is limited by the finite amount of final state particles. Additionally, the technique is affected by the event-by-event flow fluctuations, and the strong dependence on the resolution limits the reproducibility between different experiments as pointed out in [53].

The problem of estimating  $\Psi_n$  can be circumvented by applying the flow principle, i.e. that all particles are emitted from the common source independently of each other. Using this, one can introduce a 2-particle correlator  $\langle e^{in(\varphi_1 - \varphi_2)} \rangle$ , which evaluates the azimuthal angles  $\varphi_1$  and  $\varphi_2$  of two particles relative to each other. In the single event average, which takes all possible combinations between distinct particle pairs (see Sec. 2.3), one recovers for the real part  $\Re$  of the 2-particle correlator the following relation

$$\begin{aligned} \Re \left( \langle e^{in(\varphi_1 - \varphi_2)} \rangle \right) &= \Re \left( \langle e^{in(\varphi_1 - \Psi_n - \varphi_2 + \Psi_n)} \rangle \right) \\ &= \Re \left( \langle e^{in(\varphi_1 - \Psi_n)} \rangle \langle e^{in(\varphi_2 - \Psi_n)} \rangle \right) \\ &= v_n^2. \end{aligned} \quad (2.18)$$

Note that in the short calculation above, the factorisation from the first to the second line is justified by the flow principle. Further, it was exploited that the imaginary part of  $\langle e^{in(\varphi - \Psi_n)} \rangle$  is zero (see App. A.1). This result was generalized by Bhalerao *et al.* [54] to

$$\langle k \rangle_{n_1, n_2, \dots, n_k} \equiv \langle e^{i(n_1\varphi_1 + n_2\varphi_2 + \dots + n_k\varphi_k)} \rangle = v_{n_1} v_{n_2} \dots v_{n_k} e^{i(n_1\Psi_{n_1} + n_2\Psi_{n_2} + \dots + n_k\Psi_{n_k})}, \quad (2.19)$$

which links a generic multiparticle correlator of  $k$  azimuthal angles to the flow amplitudes  $v_n$  and symmetry planes  $\Psi_n$ . In Eq. (2.19),  $\{n_1, \dots, n_k\}$  are the so-called flow harmonics. Additionally, the notation  $\langle k \rangle_{n_1, \dots, n_k}$  has been introduced for a  $k$ -particle correlator with harmonics  $\{n_1, \dots, n_k\}$ . As such, by utilizing multiparticle azimuthal correlation techniques, the symmetry planes  $\Psi_n$  are not needed any longer as an input for

the measurement of flow amplitudes, but rather become a part of the experimental results themselves. By proper choice of the flow harmonics, the symmetry planes cancel out on the right-hand side of Eq. (2.19) such that it is possible to measure only flow amplitudes. However, it is not possible to find a set of harmonics that result in an expression only for the symmetry planes without any contribution of the flow amplitudes. Thus, one needs to employ estimators for the measurement of symmetry planes as it is shown in Sec. 5.1.

At this point, one has to stress that for particle detectors, which cover the full transverse plane (i.e.  $\varphi \in [0, 2\pi)$ ), the flow harmonics  $\{n_1, \dots, n_k\}$  cannot be chosen arbitrarily. They have to obey the *isotropy condition* [54]

$$n_1 + \dots + n_k = 0. \quad (2.20)$$

If this condition is violated, the multiparticle correlator of Eq. (2.19) will trivially lead to zero when averaged over all events due to the randomness of the reaction plane. As an example, consider the schematic representation of a few heavy-ion collisions in Fig. 2.2. In this sketch, every heavy-ion collision is assumed to be perfectly identical with the only

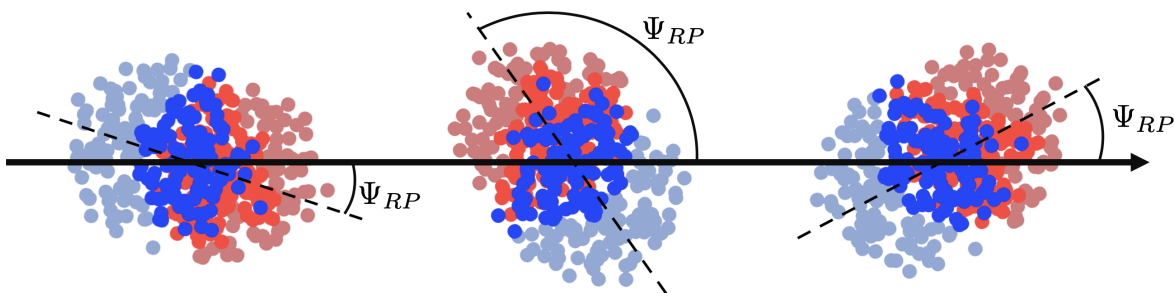


Figure 2.2: Schematic representation of the event-by-event fluctuation of the reaction plane  $\Psi_{RP}$ .

difference being the random orientation of the reaction plane  $\Psi_{RP}$ . As such, every distribution of emitted particle relative to the corresponding reaction plane will be identical for each of these collisions. However, as the laboratory frame does not shift correspondingly to the fluctuation of the reaction planes, the truly measured distributions will be shifted by the random phase  $\Psi_{RP}$  for each collision. As the physics of the collisions do not change, any experimental observable has to be invariant under these random shifts of the reaction plane. In case of the observables that are accessible by the multiparticle correlators (Eq. (2.19)), this means that the left-hand side (and consequently the right-hand side) has to be isotropic for the azimuthal angles  $\varphi$  and the symmetry planes  $\Psi_n$  such that any shift

$$\varphi \rightarrow \varphi + \Psi_{RP}, \quad (2.21)$$

$$\Psi_n \rightarrow \Psi_n + \Psi_{RP}, \quad (2.22)$$

does not affect the observable. It thus becomes evident, that the isotropy condition must not be violated, otherwise the all-event average will trivially lead to zero (see App. A.2 for exemplary calculation).

## 2.3 Multiparticle correlation techniques

After introducing the connection between multiparticle correlators and the flow observables in the previous section, this part will focus on the evaluation of the correlators themselves.

### 2.3.1 Single-event averages

At first, consider the introductory example of the 2-particle correlator

$$\langle 2 \rangle_{n,-n} = \langle e^{in(\varphi_1 - \varphi_2)} \rangle. \quad (2.23)$$

To evaluate the single-event average, one has to take all possible combinations of pairs of particles, i.e.

$$\begin{aligned} \langle 2 \rangle_{n,-n} &= \langle e^{i(n(\varphi_1 - \varphi_2))} \rangle \\ &\equiv \frac{1}{M(M-1)} \sum_{\substack{l_1, l_2=1 \\ l_1 \neq l_2}}^M e^{i(n(\varphi_{l_1} - \varphi_{l_2}))}. \end{aligned} \quad (2.24)$$

In Eq. (2.24) it is assumed that the event consists of  $M$  particles. In addition, Eq. (2.24) contains the important condition  $l_1 \neq l_2$ . This prevents the presence of the so-called *autocorrelations* where a particle is correlated to itself, i.e.  $\varphi_1 = \varphi_2 = \varphi_i$ . If not removed properly, the autocorrelations will artificially add a 1 to the real part of the correlator for each particle that is correlated to itself as  $e^{i(\varphi_i - \varphi_i)} = 1$ . This results in a large bias of the final result as flow amplitudes per definition are smaller than 1 (see App. A.3). Generalised in [55], a  $k$ -particle correlator with a set of harmonics  $\{n_1, \dots, n_k\}$  can be written as

$$\begin{aligned} \langle k \rangle_{n_1, n_2, \dots, n_k} &\equiv \left\langle e^{i(n_1 \varphi_{l_1} + n_2 \varphi_{l_2} + \dots + n_k \varphi_{l_k})} \right\rangle \\ &\equiv \frac{\sum_{\substack{l_1, l_2, \dots, l_k=1 \\ l_1 \neq l_2 \neq \dots \neq l_k}}^M w_{l_1} w_{l_2} \dots w_{l_k} e^{i(n_1 \varphi_{l_1} + n_2 \varphi_{l_2} + \dots + n_k \varphi_{l_k})}}{\sum_{\substack{l_1, l_2, \dots, l_k=1 \\ l_1 \neq l_2 \neq \dots \neq l_k}}^M w_{l_1} w_{l_2} \dots w_{l_k}} \\ &\equiv \frac{N \langle k \rangle_{n_1, n_2, \dots, n_k}}{D \langle k \rangle_{n_1, n_2, \dots, n_k}}, \end{aligned} \quad (2.25)$$

where the numerator of the  $k$ -particle correlator is denoted by  $N \langle k \rangle_{n_1, n_2, \dots, n_k}$  and the denominator by  $D \langle k \rangle_{n_1, n_2, \dots, n_k}$ . Both are trivially related as the denominator can be calculated by setting all harmonics to zero in the numerator expression, i.e.

$$D \langle k \rangle_{n_1, n_2, \dots, n_k} = N \langle k \rangle_{0, 0, \dots, 0}. \quad (2.26)$$

Most importantly, Eq. (2.25) properly removes autocorrelations with the condition  $l_1 \neq l_2 \neq \dots \neq l_k$ . Additionally, particle weights  $w_i$  have been introduced. These weights can be used to correct for various detector inefficiencies (see Sec. 6.3). Thus, they can be set up as the most general functions, e.g. with dependencies on  $p_T$ ,  $\eta$  or the particle species.

Finally, the question on how a  $k$ -particle correlator can be evaluated has to be answered. An easy and straightforward approach would be the implementation of nested

loops. This approach, however, is computationally very expensive as a  $k$ -particle correlator needs  $k$  nested loops, which all run over the full event multiplicity  $M$  with proper *if*-statements to avoid autocorrelations. A much more efficient way to compute the correlator presented in Eq. (2.25) was first introduced in [55] and is called the *Generic Framework*. The basis of this framework are the so-called *Q-vectors*

$$Q_n = \sum_{j=1}^M e^{in\varphi_j}, \quad (2.27)$$

which were introduced in [56, 57]. The  $Q$ -vector in Eq. (2.27) can be computed by one single loop over the set of azimuthal angles in a single event. Using this, one can rewrite Eq.(2.24) as

$$\begin{aligned} \langle 2 \rangle_{n,-n} &\equiv \langle e^{i(n(\varphi_1 - \varphi_2))} \rangle \\ &= \frac{1}{M(M-1)} \sum_{\substack{l_1, l_2=1 \\ l_1 \neq l_2}}^M e^{i(n(\varphi_{l_1} - \varphi_{l_2}))} \\ &\equiv \frac{1}{M(M-1)} (|Q_n|^2 - M). \end{aligned} \quad (2.28)$$

The advantage of using  $Q$ -vectors is evident directly from the 2-particle case provided in Eq. (2.28). Instead of two loops over all particles, only one loop is needed for the computation of the  $Q$ -vectors. The Generic Framework generalises this usage of  $Q$ -vectors for any  $k$ -particle correlators. Firstly, particle weights are used for the  $Q$ -vectors, i.e.

$$Q_{n,p} = \sum_{j=1}^M w_j^p e^{in\varphi_j}. \quad (2.29)$$

Additionally, an efficient algorithm is provided exploiting the recursive calculation of higher order correlators from lower order ones. This is needed as the amount of terms per  $k$ -particle correlators grows with the Bell sequence and as such, a direct implementation of higher order correlators becomes difficult. In particular, only up to the sixth order the hardcoded expressions for the multiparticle correlators evaluate faster than the recursive algorithm [55].

### 2.3.2 All-event averages

Finally, after description of the single-event averages, the transition to the averages over all events will be explained. In general, such an average over  $N_{ev}$  events can be defined as

$$\langle \langle k \rangle \rangle = \frac{\sum^{N_{ev}} W_i \cdot \langle k \rangle_i}{\sum^{N_{ev}} W_i} \quad (2.30)$$

where  $\langle k \rangle_i$  are the results from the multiparticle correlator in one event and  $W_i$  the event weights.

In the averaging over many events, one has to keep in mind that the multiplicity is a fluctuating quantity. As such, a multiparticle correlator from one event is often calculated with a different amount of particles than the one in another event. These event-by-event multiplicity fluctuations have to be taken into account. In general, the statistical stability of a multiparticle correlator increases with the event multiplicity [52]. As it was shown

in [16], a unit weight in the all-event average can bias flow measurements with multiparticle correlators and can lead to a larger statistical error if the multiplicity fluctuations are not taken into account. This problem can be circumvented by averaging only events with the same multiplicity with a unit weight and later rebin the obtained results [58]. An alternative approach to this is based on the *number of combinations* [59] of creating  $k$  tuples of particles in an event of multiplicity  $M$ . In particular, this method was shown to reduce the statistical spread of the final observable after the all-event averaging [16]. In the case where no particle weights have been used, the event weights of this method are given for a 2-, 3- and 4-particle correlator by

$$\begin{aligned} W_{\langle 2 \rangle} &= M(M-1), \\ W_{\langle 3 \rangle} &= M(M-1)(M-2), \\ W_{\langle 4 \rangle} &= M(M-1)(M-2)(M-3). \end{aligned} \quad (2.31)$$

This can be generalised to the event weight of a  $k$ -particle correlator as

$$W_{\langle k \rangle} = \binom{M}{k} k!. \quad (2.32)$$

Should particle weights have been used, the corresponding event weights can be obtained by the evaluation of the denominator in Eq. (2.25). In fact, the weights in Eqs. (2.31) are easily obtained from the denominator of Eq. (2.25) in the case of unit particle weights.

## 2.4 Flow vs non-flow

In contrast to the previously defined phenomenon of flow, one categorises any kind of few particle correlations which are not directly linked to the common source of emission, i.e. the QGP, as *non-flow*. Typical non-flow phenomena involve jet fragmentation, interactions between final state particles or resonance decay. These effects violate the independent emission of particles, and thus break the factorisation in Eq. (2.9). It is therefore important to understand the contribution of non-flow phenomena in experimental analyses. It is common to use a probabilistic approach to estimate the non-flow contribution  $\delta_k$  to a  $k$ -particle correlator as [58, 60]

$$\delta_k \approx \frac{1}{M^{k-1}}. \quad (2.33)$$

Consider the example in Fig. 2.3 which is composed of particles only genuinely correlated by the source (i.e. flow) and a non-flow contribution stemming from a particle decaying into four daughters. The probability to have purely the daughters in e.g. a 3-particle correlator is thus given by

$$\delta_3 \propto \frac{4}{M} \frac{3}{M-1} \frac{2}{M-2} \approx \frac{1}{M^3} \quad (2.34)$$

where the prefactor of 4 accounts for the 4 possible combinatorial groups of having three daughters together. The approximation on the right-hand side in Eq. (2.34) is justified if the event multiplicity  $M$  is large, which is the case for heavy-ion collisions. It thus becomes evident, that higher order correlators are less affected by non-flow even though it has to be noted that they are statistically more demanding. Non-flow effects can at least partially be reduced in the experiment by e.g. excluding high- $p_T$  particles as jets in general originate from high- $p_T$  partons and hard processes. As such, excluding high- $p_T$  particles in flow analyses can effectively reduce the contributions from jets.

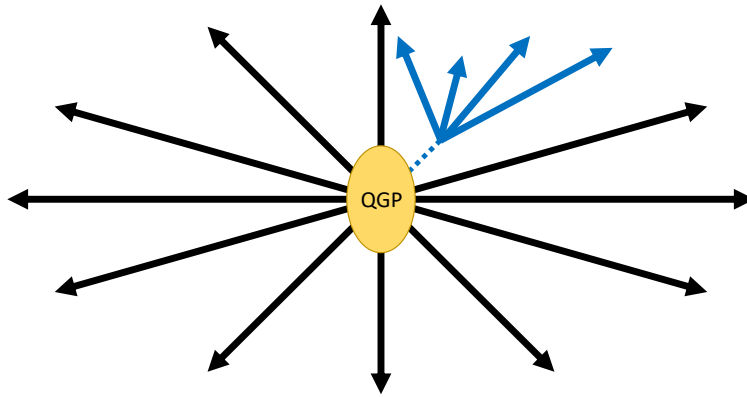


Figure 2.3: Schematic representation of non-flow. The black arrows represents particles, which are only correlated to the common source (the QGP), while the daughters of a particle decay (blue arrows) introduce non-flow correlations to the measured azimuthal correlations.

## 2.5 Summary of important experimental results in flow

In this section, a short overview over key measurements of flow observables obtained in the past years is given. While the study of anisotropic flow has a long history, especially with many flow measurements performed at RHIC, this section will focus mostly on results obtained in the LHC area.

The first measurements of anisotropic flow at the LHC have been provided by the ALICE Collaboration [51] with the measurement of the flow amplitudes  $v_2$  for Pb–Pb collisions at  $\sqrt{s_{NN}} = 2.76$  TeV. The results have been obtained as a function of centrality (see Fig. 2.4) and also as a function of transverse momentum  $p_T$ . In particular, this study

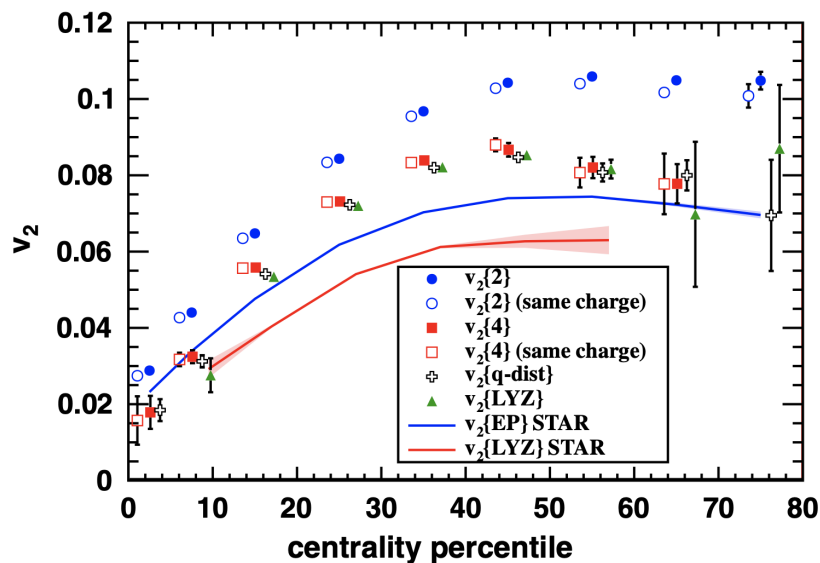


Figure 2.4:  $v_2$  as a function of centrality measured by ALICE in Pb–Pb collisions at  $\sqrt{s_{NN}} = 2.76$  TeV [51].

has utilized a cumulant-based approach for the measurement of the flow amplitudes [52,

59, 60], which has been shown to suppress non-flow contributions. The first two orders of this method are

$$v_2\{2\} = \sqrt{\langle v_n^2 \rangle} \quad (2.35)$$

$$v_2\{4\} = \sqrt[4]{-\langle v_n^4 \rangle + 2\langle v_n^2 \rangle^2} \quad (2.36)$$

$$(2.37)$$

where  $\langle v_n^2 \rangle$  and  $\langle v_n^4 \rangle$  are estimated via 2- and 4-particle correlators, respectively. The obtained results show the general behaviour for anisotropic flow as a function of centrality:  $v_2$  is small for the most central collisions as anisotropic flow cannot develop in this region due to the lack of initial anisotropy. With increasing centrality the magnitude of  $v_2$  rises, reaching a maximum for mid-central collisions around 40–50%. Afterwards, the signal starts to go down again, which indicates less strong anisotropic flow. Latter observation is expected for peripheral collisions at the system size is small and the evolution time very short, such that the initial anisotropy cannot be transferred into the momentum space.

A significant progress in the measurement of flow amplitudes has been obtained with the introduction of the so-called symmetric cumulants (SC) [55], which are defined as

$$SC(n, m) = \langle v_n^2 v_m^2 \rangle - \langle v_n^2 \rangle \langle v_m^2 \rangle. \quad (2.38)$$

These observables measure the genuine correlations between the two flow amplitudes  $v_n^2$  and  $v_m^2$ . The first experimental study of the SC have been conducted by the ALICE Collaboration [61] and has found non-zero signals for the SC(2,4) and SC(2,3), demonstrating the correlations between the involved flow amplitudes (see Fig. 2.5). The SC proved to

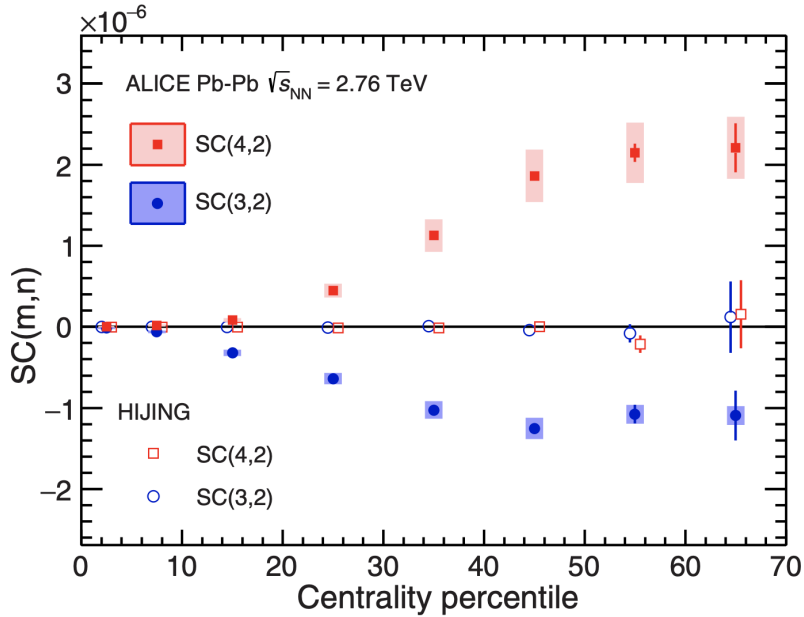


Figure 2.5: SC(2,4) and SC(2,3) as a function of centrality measured by ALICE in Pb–Pb collisions at  $\sqrt{s_{\text{NN}}} = 2.76$  TeV [61].

be particularly useful, as they provided a sensitivity to the temperature dependence of the shear viscosity over entropy density ratio  $\eta/s$ , which was not present in previous measurements. A recent study generalized the SC to higher orders [58], with the first results of correlations between three flow amplitudes provided by the ALICE Collaboration [62].

The first measurements of symmetry plane correlations were conducted by the E877 experiment [63], with many more studies performed by the PHENIX experiment at

RHIC [64, 65]. The first results of SPC during the LHC era have been obtained by the ALICE Collaboration [66]. In this study, no quantitative values of the SPC have been extracted, but the measurement provided the first information that such a correlation exists. The most detailed study of SPC at the LHC to this day were carried out by the ATLAS Collaboration [67, 68, 69], measuring a wide range of correlations between two and three symmetry planes (see Fig. 2.6 for an example) in Pb–Pb collisions at  $\sqrt{s_{NN}} = 2.76$  TeV. This study utilized two methods in the analysis, the event plane

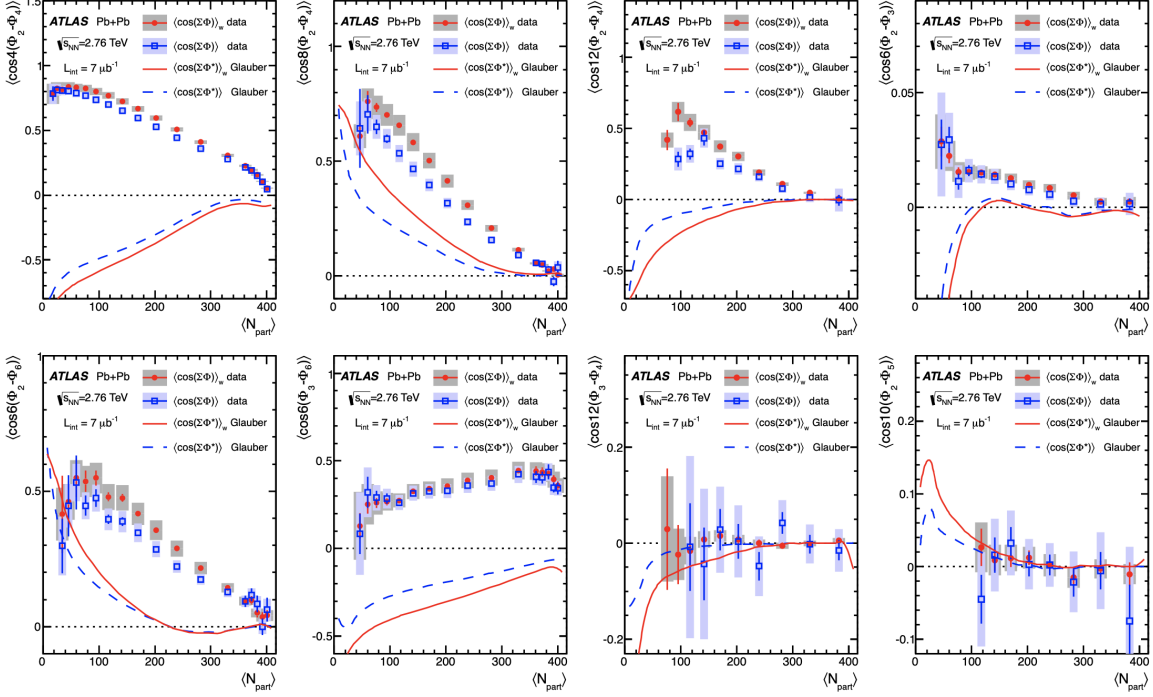


Figure 2.6: SPC between two planes as a function of number of participants  $N_{part}$  measured by ATLAS in Pb–Pb collisions at  $\sqrt{s_{NN}} = 2.76$  TeV [67]. The solid symbols are the data obtained via the SP method, while the open symbols correspond to the EP method.

method (see Sec. 2.2) and the so-called Scalar Product (SP) method [70, 71], where the latter method resulted in slightly larger values for some of the measured SPC observables (see Fig. 2.6). In the latter approach, the SPC is measured as

$$\langle \cos(a_1 n_1 \Psi_{n_1} + \dots + a_k n_k \Psi_{n_k}) \rangle_{SP} = \frac{\langle v_{n_1}^{a_1} \dots v_{n_k}^{a_k} \cos(a_1 n_1 \Psi_{n_1} + \dots + a_k n_k \Psi_{n_k}) \rangle}{\sqrt{\langle v_{n_1}^{2a_1} \rangle \dots \langle v_{n_k}^{2a_k} \rangle}}, \quad (2.39)$$

where a quantity consisting of flow amplitudes and symmetry planes is measured for the numerator. The contribution of the flow amplitudes is divided out by a factorised mean of the respective flow amplitudes in the denominator. This last step in particular introduces a bias into the measurement as a joined mean of flow amplitudes (numerator) is divided by a factorised mean in the denominator. However, this factorisation is not valid as the flow amplitudes themselves are correlated as it was shown by the measurement of the SC. The presence of this bias will be demonstrated in Sec. 5.1.3 where a new approach for measuring SPC will be demonstrated based on [72]. A similar approach to the SP method has been used in a study by the ALICE Collaboration [73], which partially solved the issue of factorised means but did not overcome it fully.

# Chapter 3

## Theoretical models

In this chapter, the theoretical models that are used throughout the thesis are described. In Sec. 3.1 and Sec. 3.2 the Glauber and T<sub>R</sub>ENTo initial state models are discussed, while Sec. 3.3 and Sec. 3.4 focus on the iEBE-VISHNU and HIJING model, respectively.

### 3.1 Glauber model

The Glauber model can be used for calculating the initial geometry of high-energy nuclear collisions. There exist two approaches for the model, the optical Glauber model and a Monte Carlo based Glauber [37]. Focussing on the latter version, the colliding nuclei are sampled from scratch on an event basis according to the Woods-Saxon distribution

$$\rho(r) = \rho_0 \frac{1 + w \left(\frac{r}{R}\right)^2}{1 + \exp\left(\frac{r-R}{a}\right)}. \quad (3.1)$$

In the above equation,  $\rho$  is the nucleon density,  $w$  a parameter describing the deviation from a perfect sphere,  $R$  the nuclear radius and  $a$  the skin depth of the nucleus. As such, the radial position can be sampled from a distribution proportional to  $\rho(r) r^2$ , while the azimuthal and polar angle can be obtained from uniform distributions in the interval  $[0, 2\pi)$  and  $[0, \pi)$ , respectively. During this sampling process, it is possible to require a minimal distance between the nucleons of the same nucleus.

After the sampling, the two nuclei, which are displaced relative to each other in the transverse plane by the impact parameter  $b$ , are then collided. For this collision process, the Glauber model makes the assumption that any nucleon that undergoes an inelastic interaction continues to travel on a straight path after the collision. In particular, the nucleons can participate in many of such collisions. Whether a nucleon undergoes an inelastic process can be determined in several ways. The simplest is the *black disk approach*, which assigns a collision between two nucleons of the two different nuclei if their distance in the transverse plane is smaller than a distance  $R_c$ . This distance is determined via the inelastic proton-proton cross-section  $\sigma_{NN}^{inel}$  as [37]

$$R_c = \sqrt{\frac{\sigma_{NN}^{inel}}{\pi}}. \quad (3.2)$$

Using this approach of independent nucleon-nucleon collisions, one obtains the number of colliding nucleons  $N_{part}$  (also called wounded nucleons), as well as the total amount of binary collisions  $N_{coll}$  per event. In addition, using the positions of the participants

in the transverse plane, one can calculate the eccentricities and participant planes of the collision as [74]

$$\epsilon_n = \frac{\sqrt{\langle r^n \cdot \cos(n \cdot \varphi) \rangle^2 + \langle r^n \cdot \sin(n \cdot \varphi) \rangle^2}}{\langle r^n \rangle}, \quad (3.3)$$

$$\Phi_n = \frac{1}{n} \cdot [\text{atan2}(\langle r^n \cdot \sin(n \cdot \varphi) \rangle, \langle r^n \cdot \cos(n \cdot \varphi) \rangle) + \pi]. \quad (3.4)$$

Therefore, the MC Glauber can be used to model the anisotropies in the initial state.

### 3.1.1 MuPa Glauber model

A local version of the Monte Carlo Glauber model, dubbed *MuPa Glauber* has been presented in its first version in [75]. Since then, the model has been improved to accommodate a random impact parameter drawn from a distribution proportional to  $b$  in the interval  $b \in [0, 20]$  fm. Additionally, the minimal distance required between nucleons within the same nucleus is set from 0.8 fm to a new value of 0.4 fm in accordance to [76].

To validate the MuPa Glauber model, Pb–Pb collisions at  $\sqrt{s_{NN}} = 2.76$  TeV are simulated. For sampling the lead ions, a nuclear radius of  $R = 6.67$  fm, a sphere parameter of  $\omega = 0$  and a nuclear skin depth of  $a = 0.44$  fm are used. These parameters were chosen in accordance to [77]. The minimal distance of 0.4 fm between the nucleons in the same nucleus is required in the sampling. The inelastic nucleon-nucleon cross-section is chosen as  $\sigma_{NN}^{inel} = 61.8$  mb [76]. In addition to that, the wounded nucleons are smeared around their position in the radial direction with a Gaussian distribution of width  $0.25$  fm<sup>2</sup>.

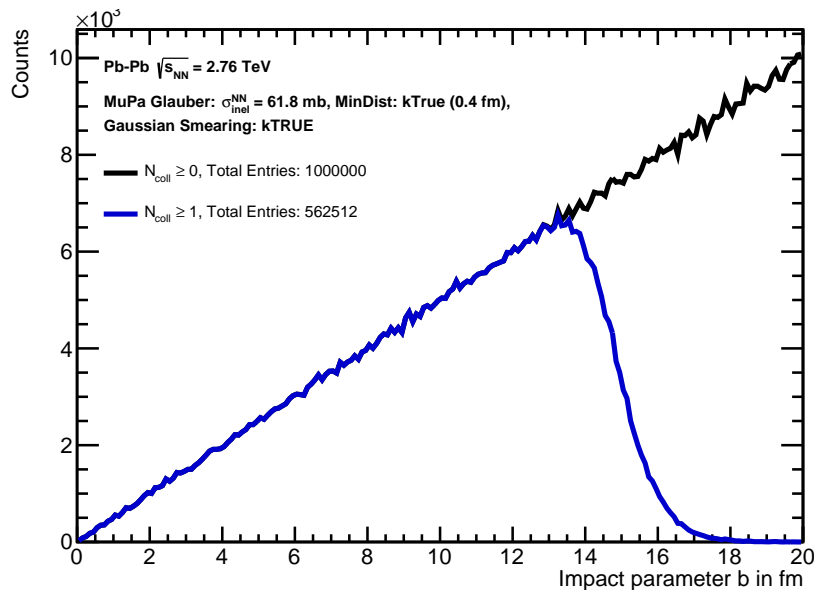


Figure 3.1: Impact parameter distribution of all events (black) and of events with at least one inelastic nucleon-nucleon interaction (blue).

In total,  $10^6$  collisions have been simulated amongst which about 56 % have undergone inelastic collisions (see Fig. 3.1). For the centrality determination of the collisions, Eq. (1.2) is used with an inelastic Pb–Pb cross-section of  $\sigma_{Pb,Pb} = 7.55$  b in accordance to [76].

The results of this setup of the MuPa Glauber are compared to the results obtained of the SuperMC Glauber model implemented for the iEBE-VISHNU model [77]. As a cross-check,  $\epsilon_2^2$  and  $\epsilon_3^2$  (Fig. 3.2a) as well as the symmetric cumulants SC(2,3) and SC(2,4)

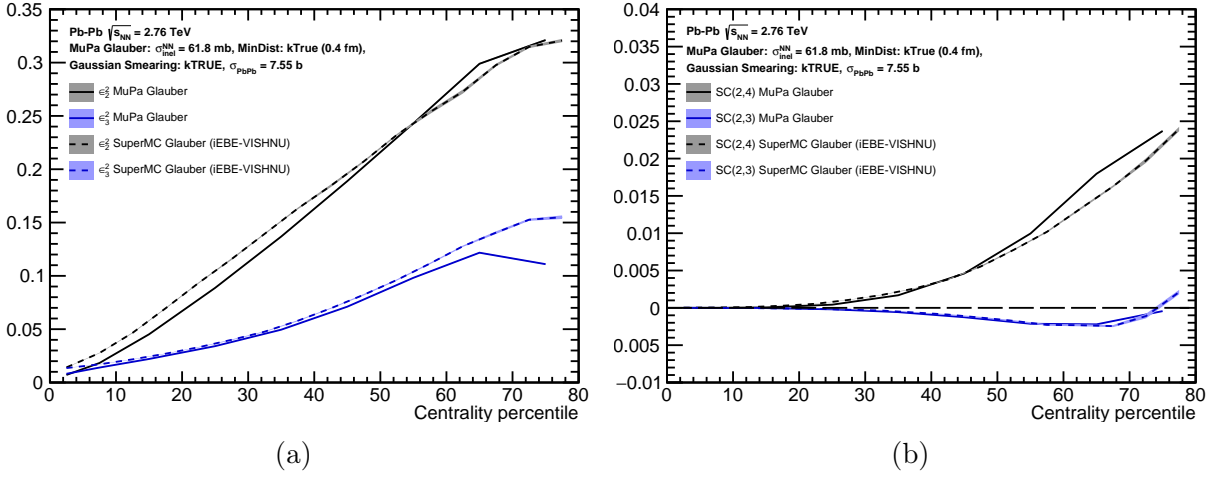


Figure 3.2: Comparison between the MuPa Glauber and the SuperMC Glauber from iEBE-VISHNU for  $\epsilon_2^2$  and  $\epsilon_3^2$  (a) and SC(2, 3) and SC(2, 4) (b).

(Fig. 3.2b) are compared. As it can be seen, the two models agree well with each other, given the fact that no sophisticated centrality determination is employed in the MuPa Glauber model. In particular, Eq. (1.2) is only valid for central to mid-central collision, which explains the great agreement between the MuPa Glauber and the SuperMC in this region.

### 3.1.2 Centrality determination

In addition to its usage as an initial state model, the MC Glauber model can be used to parametrise the experimental multiplicity distribution. For this, it is assumed that the amount of produced particles per nucleon-nucleon collision is parametrized by a negative binomial distribution (NBD) [76] of the form

$$P_{\mu,k}(n) = \frac{\Gamma(n+k)}{\Gamma(n)\Gamma(k)} \cdot \frac{(\mu/k)^n}{(\mu/k+1)^{n+k}}. \quad (3.5)$$

The above equation gives the probability of producing  $n$  particles per ancestor with an expected multiplicity of  $\mu$  and width  $k$ .  $\Gamma$  is the gamma function, i.e.  $\Gamma(m) = (m-1)!$  for positive integer  $m$ . The number of ancestors  $N_{ancestor}$  is parametrised as  $N_{ancestor} = f \cdot N_{part} + (1-f) \cdot N_{coll}$  [76].  $N_{ancestor}$  represents a two-component approach that separates the collision into soft and hard processes, where the soft interactions produce particles with a multiplicity proportional to  $N_{part}$  and the hard processes proportional to  $N_{coll}$ . The NBD above is then utilized  $N_{ancestor}$  times per MC Glauber event to obtain the final multiplicity distribution. Using  $\mu$ ,  $k$  and  $f$  as parameters, one can fit the Glauber multiplicity to the measured experimental distribution as shown in Fig. 3.3.

This allows to relate the experimentally measured centrality classes to the averages of number of participants, number of binary collisions and impact parameter in the initial state.

## 3.2 T<sub>R</sub>ENTo

The *Reduced Thickness Event-by-event Nuclear Topology*, in short T<sub>R</sub>ENTo [78], is an initial state model for the study of high-energy nuclear collisions. The model uses the so-called *participant thickness*  $T_{A,B}(x, y)$  of the two nuclei A and B, which collide along

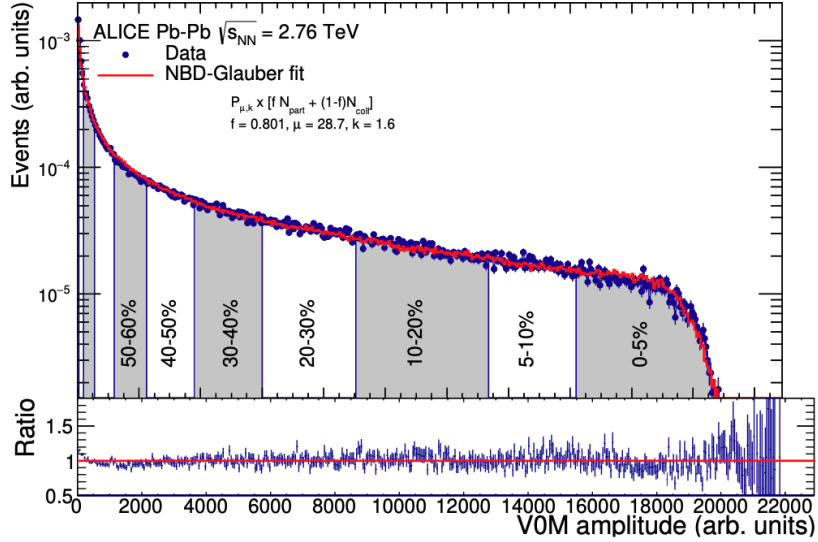


Figure 3.3: Experimentally measured multiplicity distribution of Pb-Pb at  $\sqrt{s_{NN}} = 2.76$  TeV with ALICE and the corresponding MC Glauber multiplicity fit. Taken from [76].

the beam axis  $z$  for the calculation of the initial entropy density profile. The thicknesses are obtained via the density  $\rho_{A,B}^{part}$  of nuclear matter participating in the collision as

$$T_{A,B}(x, y) = \int \rho_{A,B}^{part}(x, y, z) dz. \quad (3.6)$$

For obtaining the entropy density profile, T<sub>RENT</sub>o assumes that there is a scalar field  $f(T_A, T_B)$  proportional to the entropy deposition, which is related to the participant thicknesses. In particular, the model uses the *reduced thickness*  $T_r$  as the scalar field in the form of

$$f = T_R(p; T_A, T_B) = \left( \frac{T_A^p + T_B^p}{2} \right)^{1/p}. \quad (3.7)$$

In Eq. (3.7),  $p$  is a dimensionless, continuous parameter. Using this approach, T<sub>RENT</sub>o is an effective model that does not make any assumption of the underlying physics of the mechanisms leading to the initial entropy density. However, the parameter  $p$  allows the interpolation between different physical mechanisms related to the entropy production. For example, by using  $p = 1$ , one obtains the wounded nucleon approach, which can be similarly obtained from the Glauber model.

### 3.3 iEBE-VISHNU

Given an initial energy density profile, e.g. from the Glauber model or T<sub>RENT</sub>o, the iEBE-VISHNU model [77] is used for modelling the subsequent hydrodynamic evolution of the system. It uses 2+1 causal hydrodynamics (this part is called VISH2+1), and an equation of state obtained via lattice QCD and the hadronic resonance gas model [79]. After the hydrodynamic evolution, the Cooper-Frye formalism [80] is used for obtaining the distribution of hadrons from the evolved fluid. After this hadronization, the UrQMD model [81, 82] is utilised to simulate the subsequent evolution in the hadronic stage.

Throughout this thesis, the iEBE-VISHNU model will be used in two distinct setups. The first setup uses the SuperMC Glauber implemented within iEBE-VISHNU as the initial state, where the hydrodynamic evolution is initiated at  $\tau = 0.6$  fm/c. The shear

viscosity over entropy density  $\eta/s$  is fixed to 0.08. After the freezeout, no evolution in the hadronic stage is considered, such that an exact event-by-event determination of  $v_n$  and  $\Psi_n$  is feasible without using any estimators (see [72] for more details). For each centrality bin, 14k Pb–Pb collisions at  $\sqrt{s_{\text{NN}}} = 2.76$  TeV are generated with this setup.

The second setup has T<sub>R</sub>ENTo as the initial state with  $p = 0.007$ . After the hydrodynamic evolution, UrQMD is used for the evolution in the hadronic stage. The parameters of the initial conditions, the transport properties, like the shear viscosity over entropy density  $\eta/s$  and bulk viscosity over entropy density  $\zeta/s$ , as well as other free parameters of the combined model have been obtained from a global Bayesian analysis [83]. The used values in this model are chosen from the best-fit parameters from the maximum *a posteriori* for Pb–Pb collisions at  $\sqrt{s_{\text{NN}}} = 2.76$  TeV. In this setup, the model does not provide direct access to the  $v_n$  and  $\Psi_n$  and thus one needs to use multiparticle correlation techniques.

### 3.4 HIJING

The last model used is the *Heavy-Ion Jet INteraction Generator* (HIJING) model [84, 85], which is a Monte Carlo based event generator introduced for the study of jet and particle production in high-energy collisions between pp, p-A and A-A. The model contains various physical mechanisms such as jets, minijet production or jet quenching. These effects are obtained via the inclusion of other models within HIJING, e.g. pQCD and PYTHIA for the modelling of interactions between hadrons. However, HIJING does not contain any notion of anisotropic flow and it can thus be used to study non-flow effects on the flow observables of interest. The model can also be used in the study of inefficiencies and non-uniform acceptances of the ALICE detector (see Sec. 4.2). For this, simulations based on HIJING propagated through the ALICE detector are analysed. Specifically for this study, simulated data anchored the LHC10h Pb–Pb data at  $\sqrt{s_{\text{NN}}} = 2.76$  TeV is used, where the same detector conditions are used in the model as they were during the LHC10h data taking. More details on this is provided in Sec. 6.3.



# Chapter 4

## Experimental setup

### 4.1 LHC

<sup>1</sup>Located at the European Organisation for Nuclear Research (fr. former “Conseil Européen pour la Recherche Nucléaire”) – short CERN – the Large Hadron Collider (LHC) is the largest and most powerful particle accelerator in existence. Built as a synchrotron-type accelerator, the LHC is placed within the tunnel of its predecessor, the Large Electron Positron (LEP), which was dedicated to the precision study of the  $Z^0$  and later  $W^\pm$  bosons [87]. The LHC has a total circumference of 26.7 km and is placed at an average depth of 100 m underground.

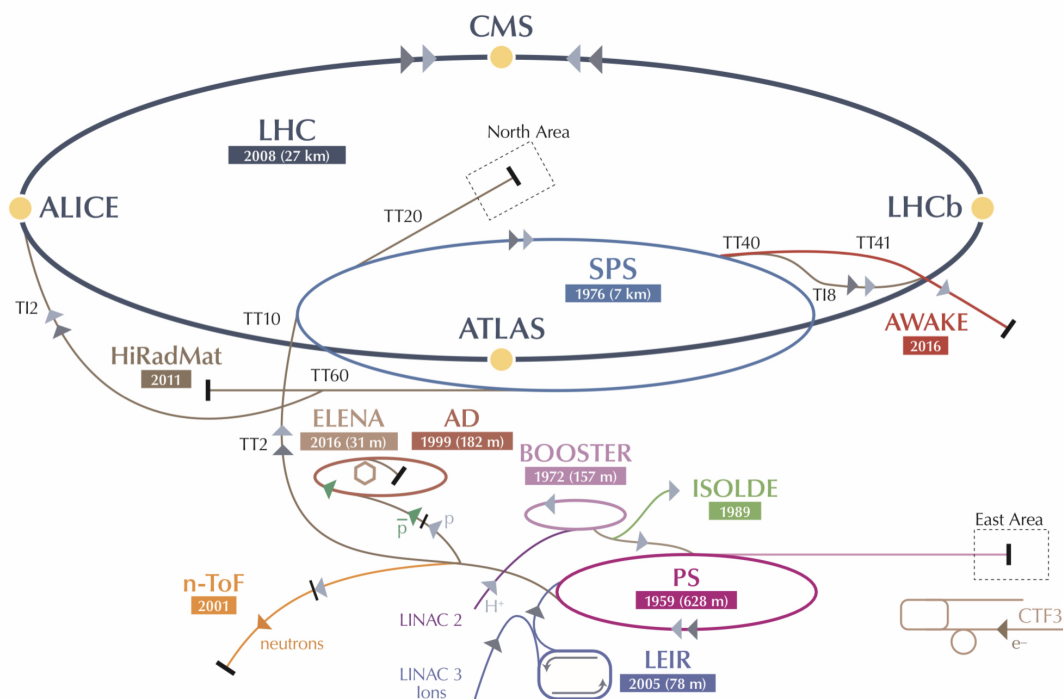


Figure 4.1: Overview of CERN and LHC, taken from [86].

The particles collided in the LHC are not injected directly into the machine but undergo a whole chain of pre-accelerators (see Fig. 4.1). For proton beams, hydrogen atoms

<sup>1</sup>Section based on [86].

are stripped of their electrons leaving the bare protons, which are then accelerated to an energy of 50 MeV in the LINAC2. After this, the protons are injected into the PS Booster (PSB), which further accelerates them to an energy of 1.4 GeV after which they are guided into the Proton Synchrotron (PS). After the PS, the protons have an energy of 25 GeV and are further injected into the Super Proton Synchrotron (SPS), where they are accelerated to an energy of 450 GeV. Only then, the protons are injected into the LHC. Concerning heavy ions, a lead sample is heated up to 800 °C and the resulting gas is ionized up to  $\text{Pb}^{29+}$ . After an acceleration to 4.2 MeV per nucleon, the particles are further ionised with a carbon stripping foil. These further ionized lead particles (mostly comprised of  $\text{Pb}^{54+}$ ), are transferred to the Low Energy Ion Ring (LEIR) where they are accelerated further and passed to the PS and then in the SPS. Before the injection into the SPS, the ions are fully ionized by passing them through a second stripping foil. After the acceleration in the SPS to 177 GeV per nucleon, the lead beam is injected into the LHC.

There, a total of eight radio-frequency cavities accelerate the particles to their final energies and compensate for synchrotron radiation losses. In total, 9600 superconducting magnets comprised of mainly dipole and quadrupole magnets define the particles trajectories. The main dipoles (in total 1232) have a magnetic field of up to 8.33 T and are cooled to 1.9 K. These dipole magnets are used to keep the particles on their circular orbit, while quadrupole magnets are used for beam focusing. With this setup, the LHC was able to accelerate and collide protons at a centre of mass of  $\sqrt{s} = 7$  TeV and Pb–Pb at centre of mass per nucleon pair of  $\sqrt{s_{\text{NN}}} = 2.76$  TeV during Run 1.

Distributed along its beam line are the four major LHC experiments. *A Toroidal LHC ApparatuS* (ATLAS) and the *Compact Muon Solenoid* (CMS) are multipurpose experiments covering a broad range of physics. These experiments were in particular involved in the experimental discovery of the Higgs Boson mentioned in the introduction and are further involved in other physics programs like the search for Supersymmetry. In addition to this, there are two more dedicated experiments. The *Large Hadron Collider beauty* (LHCb) experiment is used for investigating the differences between matter and antimatter, while *A Large Ion Collider Experiment* (ALICE) is the only dedicated heavy-ion experiment at the LHC (see Sec. 4.2).

Besides these four major experiments, there are three smaller detectors located at the LHC, the *Large Hadron Collider forward* (LHCf), the *TOTAL Elastic and diffractive cross section Measurement* (TOTEM) and the *Monopole and Exotics Detector at the LHC* (MoEDAL).

## 4.2 ALICE

Mostly devoted to the study of the strongly interacting QCD matter at extreme temperatures, ALICE [88, 89] is the dedicated heavy-ion experiment at the LHC. To fulfil the requirements of such research goals, ALICE is able to track and identify particles with extremely low momenta of 100 MeV/ $c$  up to large momenta of 100 GeV/ $c$  while offering outstanding particle identification (PID) capabilities. In addition, ALICE is able to cope with the large amount of particles produced in central heavy-ion collisions.

ALICE, which measures  $16 \times 16 \times 26$  m<sup>3</sup> and weighs about 10000 t, can be divided into two main parts (see Fig. 4.2). The first region is placed within the solenoid magnet with a nominal magnetic field of 0.5 T and is called the *central barrel*. Within this central part, the most important detectors of ALICE are placed for the detection of hadrons, electrons and photons within a pseudorapidity range of  $|\eta| < 0.9$ .

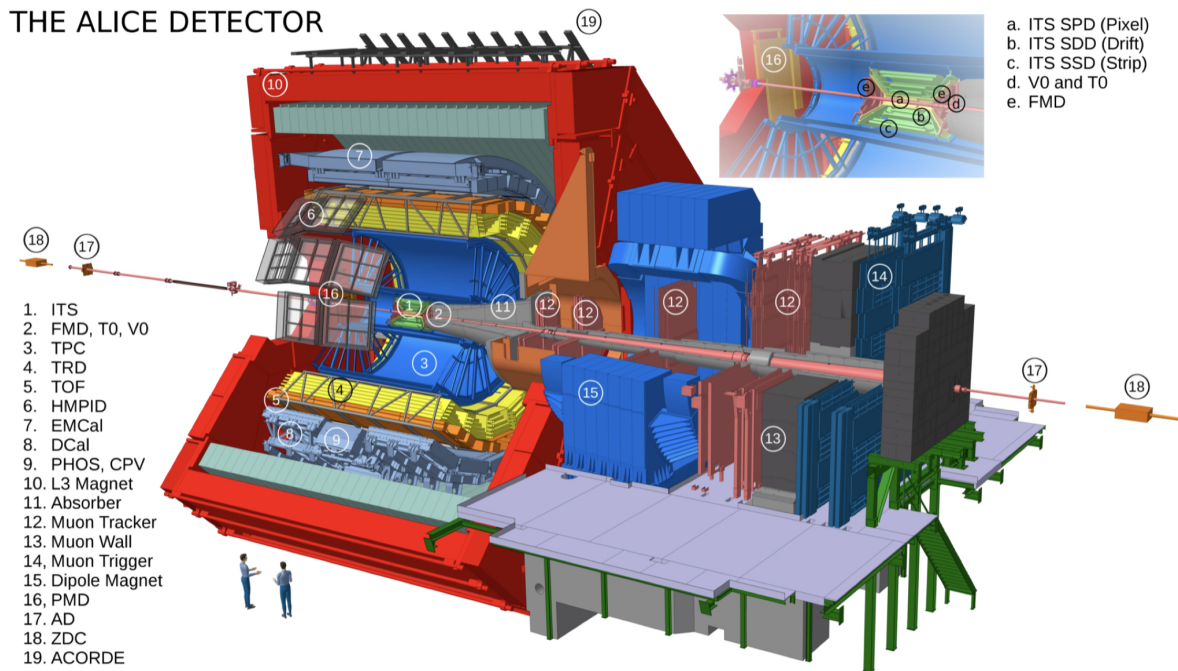


Figure 4.2: Overview of ALICE, taken from [90].

Closest to the beam line is the *Inner Tracking System* (ITS) whose main purpose is the determination of the primary collision vertex as well as the reconstruction of secondary vertices of fast decaying particles such as heavy flavours or strange particles. In particular, the ITS allows the tracking of low momentum particles that do not reach the more outer detectors. After the ITS, a gas detector, the so-called *Time Projection Chamber* (TPC), is placed. Its main purpose is the tracking and high resolution PID of the produced charged particles. The momentum resolution and PID of high momentum particles can be further improved by employing the subsequent detectors, the *Transition Radiation Detector* (TRD) and the *Time Of Flight* (TOF), which are placed still within the central barrel.

Placed between the structural support of the above mentioned detectors, the *Electromagnetic Calorimeter* (EMCal) is used for the energy measurement of charged particles as well as a trigger of high momentum particles. During the long shutdown between Run 1 and Run 2, the *Dijet Calorimeter* (DCal) has been added following the EMCal. Complementing these main detectors of ALICE, two smaller detectors are placed within the central barrel. Those are the *High Momentum Particle Identification* (HMPID) and the *Photon Spectrometer* (PHOS). It has to be stressed that the EMCal, DCal, HMPID and PHOS do not provide a full azimuthal coverage. Placed at large rapidities on one side of ALICE is additionally the muon spectrometer with its own dipole magnet.

In addition to these detectors, ALICE has several detectors in the forward and backward region located close to the beam pipe. The Zero Degree Calorimeter (ZDC) provides information for the estimation of the impact parameter, while the Photon Multiplicity Detector (PMD) is dedicated for measurement of the amount of produced photons. The Forward Multiplicity Detector (FMD), the T0 and V0 are employed as fast triggers. Above the L3 magnet is an additional detector specialized for the measurement of cosmic rays which is called the *ALICE Cosmic Ray Detector* (ACORDE).

### 4.2.1 ITS

ALICE most inner tracking system – the ITS [88] – is composed of six layers of semiconductor detectors based on three different types of technologies (see Fig. 4.3). The two innermost layers are the *Silicon Pixel Detectors* (SPD), followed by two layers called the *Silicon Drift Detectors* (SDD). The two outermost layers of the ITS are the *Silicon Strip Detectors* (SSD).

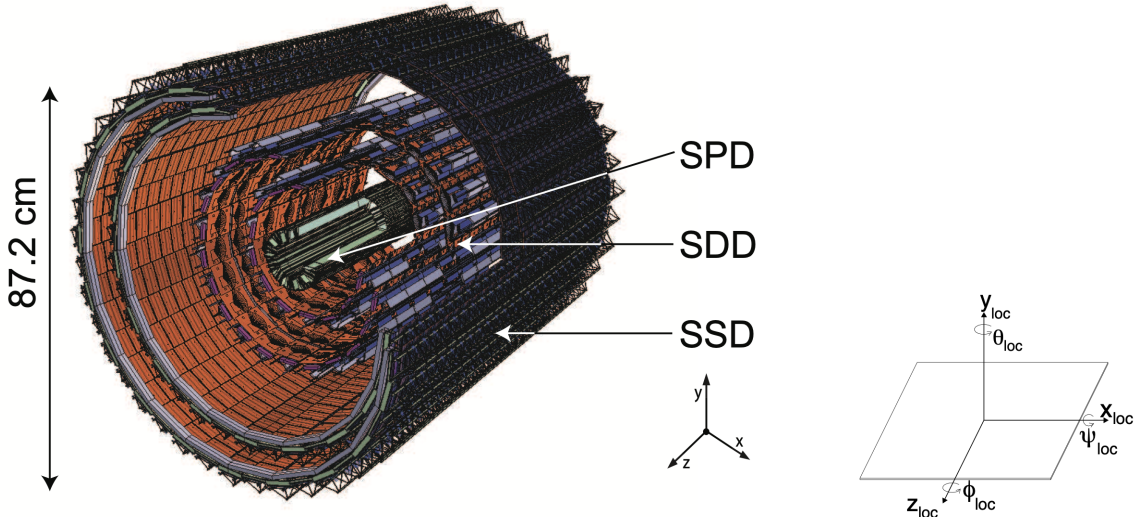


Figure 4.3: Model of the ITS detector, taken from [91].

Placed at radii of 3.9 cm and 7.6 cm, the two SPD layers are crucial in the determination of the primary vertex as well as measurement of the distance of closest approach of secondary particles, stemming from weak decays of heavy flavour particles. In total,  $9.8 \times 10^6$  cells give the SPD the fine granulation needed to be operated in environments with track densities up to 80 tracks/cm<sup>2</sup>. The SDD, which are placed at distances of 15 cm and 23.9 cm have to cope with lower track densities of about 7 tracks/cm<sup>2</sup>. They have good multitrack capabilities and provide two of the four  $dE/dx$  samples needed for the particle identification of the ITS. The last two layers of the ITS, the SSD, are located at radii of 38 cm and 43 cm. They are employed for the track fitting between ITS and TPC.

Combining all the ITS layers, the primary vertex of a collision can be located with high resolution within 100  $\mu\text{m}$  while providing a pseudorapidity coverage of  $|\eta| < 0.9$  for the full azimuth. In addition to this, the SPD clusters can be employed for centrality determination.

### 4.2.2 TPC

Utilized as the main tracking and PID detector in ALICE, the TPC [88] provides information about the tracks, momenta as well as PID of the charged particles. It is a cylindrical gas detector with an inner radius of 85 cm, an outer radius of 250 cm and a length of 500 cm. During the LHC Run 1, the 88 m<sup>3</sup> of detector volume contained a mixture of 90 % Ne and 10 % CO<sub>2</sub>.

Along its length, the TPC is divided into two sections by a central high-voltage electrode with 100 kV, which generates a highly uniform electrostatic drift field of about 400 V/cm. When a charged particle traverses the detector gas, it interacts with it, leading to

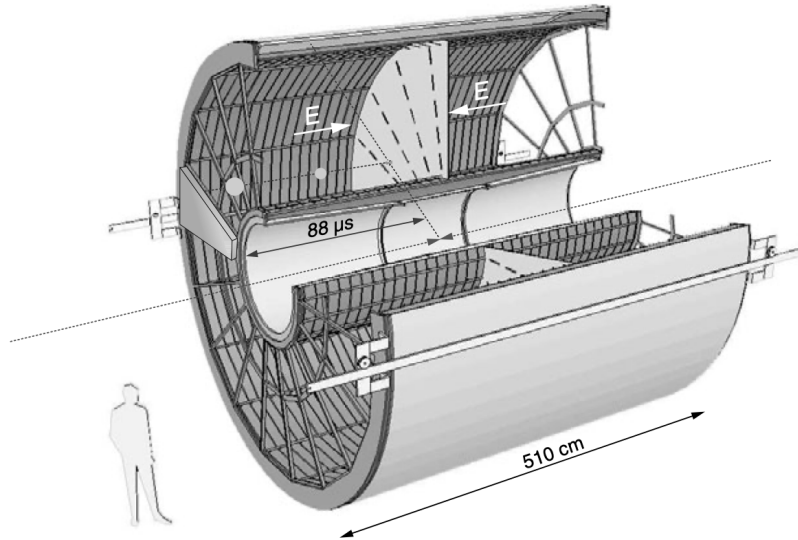


Figure 4.4: Model of the TPC detector, taken from [88].

the creation of ionized particles. With the applied electrostatic field, these ions drift with a maximum time of about  $90 \mu\text{s}$  from the centre of the TPC before reaching one of the endplates. These endplates contain the readout chambers made of Multi-Wire Proportional Chambers (MWPC) and amplify the incoming signal of primary electrons. For the reconstruction of the radial  $r$  and azimuthal coordinates  $\varphi$  of the track, the localisation of the produced ions registered by the readout chambers is used. The third coordinate  $z$  in the longitudinal direction is obtained by the time of flight measurement. As such, the TPC allows a whole three-dimensional reconstruction of the tracks in the momentum range of  $0.1 < p_{\text{T}} < 100 \text{ GeV}/c$  while covering a pseudorapidity range of  $|\eta| < 0.9$  with uniform azimuthal coverage.

As a final remark, it has to be noted that during the LHC Run 1 and Run 2, the TPC had a gating system. The gate would be opened  $6.5 \mu\text{s}$  after a collision has been triggered and is kept open for the maximum drift time of  $90 \mu\text{s}$ . After this time, the gate is closed such that no further electrons can reach the readout chambers. This prevents space charge distortions from secondary ionisations in the gas as well as ions drifting back to the active volume where they perturbate the homogeneous electrostatic drift field. As such, the TPC can cope with collisions at a rate of about  $10 \text{ kHz}$ . For the upcoming LHC Run3, a new readout system is installed for the TPC which employs so-called Gas Electron Multipliers (GEMs) [92, 93]. This technology allows for a continuous readout of the incoming signals and thus a higher detection rate.

### 4.2.3 V0

The V0 is a detector consisting of two parts called the V0A and V0C. The V0A is located  $329 \text{ cm}$  from the nominal interaction point along the beam line while V0C has a distance of  $90 \text{ cm}$  and is located at the opposite side of the interaction point compared to the V0A. Together, the V0A and V0C cover a pseudorapidity range of  $2.8 < \eta < 5.1$  and  $-3.7 < \eta < -1.7$ . These detectors are utilized to provide various triggers for the ALICE amongst which is the minimum bias trigger used for Pb–Pb collisions. An event has been triggered as minimum bias in 2010 if two of the following conditions are given: hits in at least two pixels of the outer SPD are detected, a signal in the V0A is detected or a signal in the V0C is detected.



# Chapter 5

## New technical developments for symmetry plane correlations

### 5.1 New estimator for SPC

This section presents the key idea behind the new conceptual approach on how to measure SPC as well as how this measurement would be performed ideally. After a brief explanation of the limits of this idealistic approach, a new estimator for SPC is presented and discussed. If not indicated otherwise, the results of this section are based on [72].

#### 5.1.1 Ideal measurement of SPC

As presented in Sec. 2.5, the current methods of measuring SPC are often plagued by built-in biases due to neglected correlations between flow amplitudes. To avoid this, an ideal measurement would recover the SPC on an event basis and average this result over many events. This type of approach, which will be referred to as the *event-by-event* (EbE) approach, is at least in theory possible. As an introductory example, one can consider the ratio of two 6-particle correlators within the *same* event

$$\frac{\langle \cos(2\varphi_1 + 2\varphi_2 - \varphi_3 - \varphi_4 - \varphi_5 - \varphi_6) \rangle}{\langle \cos(2\varphi_1 - 2\varphi_2 + \varphi_3 - \varphi_4 + \varphi_5 - \varphi_6) \rangle} = \frac{v_2^2 v_1^4 \cos 4(\Psi_2 - \Psi_1)}{v_2^2 v_1^4} = \cos 4(\Psi_2 - \Psi_1), \quad (5.1)$$

where Eq. (2.19) has been used to translate the multiparticle azimuthal correlators into the flow observables. Numerator and denominator have been constructed carefully, such that the numerator contains flow amplitudes and symmetry planes. The denominator is built out of the same flow amplitudes as the numerator but without any contribution of symmetry planes. As this ratio is by construction taken within the same event, the flow amplitudes cancel out exactly, resulting in a pure contribution from the symmetry planes.

This concept of event-by-event ratios of two carefully chosen correlators can be generalized for any number of  $k$  symmetry planes

$$\langle \cos(a_1 n_1 \Psi_{n_1} + \dots + a_k n_k \Psi_{n_k}) \rangle_{\text{EbE}} = \left\langle \frac{v_{n_1}^{a_1} \dots v_{n_k}^{a_k} \cos(a_1 n_1 \Psi_{n_1} + \dots + a_k n_k \Psi_{n_k}) + \delta}{v_{n_1}^{a_1} \dots v_{n_k}^{a_k} + \delta'} \right\rangle, \quad (5.2)$$

where the numbers  $a_1, \dots, a_k$  have to fulfil a certain set of constraints for the EbE approach (see [75]). Considering that numerator and denominator use different multiparticle correlators, their statistical errors will be different and are denoted in Eq. (5.2) by  $\delta$  and  $\delta'$ , respectively. This difference in per-event statistical properties limits the EbE approach. Especially, the estimation of multiparticle azimuthal correlators with Q-vectors (presented

in Sec. 2.3) has large statistical uncertainties on the single event basis due to the finite multiplicity in experimental heavy-ion collisions. This limits the applicability of Eq. (5.2) further, resulting in an unstable approach for the measurement of SPC with the currently available technologies. This instability of the EbE approach was first reported in [75].

The previously presented scalar product method [70, 71] is not affected by this statistical limitation, as the ratio is built after averaging the involved observables over many events. However, the observable used in [67],

$$\langle \cos(a_1 n_1 \Psi_{n_1} + \dots + a_k n_k \Psi_{n_k}) \rangle_{\text{SP}} = \frac{\langle v_{n_1}^{a_1} \dots v_{n_k}^{a_k} \cos(a_1 n_1 \Psi_{n_1} + \dots + a_k n_k \Psi_{n_k}) \rangle}{\sqrt{\langle v_{n_1}^{2a_1} \rangle \dots \langle v_{n_k}^{2a_k} \rangle}}, \quad (5.3)$$

has a built-in bias. Its origin is due to neglected correlations between flow amplitudes, as a joined mean of flow amplitudes is divided by the product of factorised means of the same amplitudes.

The limits of both the idealistic EbE approach as well as the scalar product method lead to the development of a new estimator for SPC. The derivation of this new approach, which is called the *Gaussian Estimator* (GE), is presented in the following subsection.

### 5.1.2 Gaussian Estimator

The GE has been developed to take into account the genuine correlations between the flow amplitudes which bias the present SPC estimators, while being statistically stable. It was shown in [94, 95] that single flow harmonics and their fluctuations can be approximated well in central to mid-central collisions with a Gaussian distribution. As such, the key idea for the derivation of the new estimator is the approximation of multi-harmonic flow fluctuations with a two-dimensional Gaussian distribution. To begin with, one defines the following quantities

$$\mathcal{R} = v_{n_1}^{a_1} \dots v_{n_k}^{a_k}, \quad \Theta = a_1 n_1 \Psi_{n_1} + \dots + a_k n_k \Psi_{n_k}, \quad (5.4)$$

where  $\mathcal{R}$  consists purely of flow amplitudes while  $\Theta$  is built only from symmetry planes. The expressions of  $\mathcal{R}$  and  $\Theta$ , which describe a polar coordinate system, can be translated into a Cartesian coordinate system using the variables  $R_x$  and  $R_y$  with

$$\mathcal{R}_x = \mathcal{R} \cos \Theta, \quad \mathcal{R}_y = \mathcal{R} \sin \Theta. \quad (5.5)$$

In general, the quantities  $\mathcal{R}_x$  and  $\mathcal{R}_y$  undergo event-by-event fluctuations due to underlying flow fluctuations per event. These fluctuations can be described via the p.d.f.  $P(\mathcal{R}_x, \mathcal{R}_y)$  or alternatively in polar coordinates  $P(\mathcal{R}, \Theta)$ . Using this p.d.f., one can study any moment of the form  $\langle \mathcal{R}_x^p \mathcal{R}_y^q \rangle = \langle \mathcal{R}^{p+q} \cos^p \Theta \sin^q \Theta \rangle$ , where only positive integers  $p$  and  $q$  are of interest. For odd  $q$ , these moments will trivially lead to zero due to sine terms with odd power. To further illustrate this latter statement made in [72], one can consider as an example the sketch provided in Fig. 5.1 where on the left-hand side,  $\Psi_3 > \Psi_2$ . However, it is equally possible to find the system in the mirrored configuration shown in the right-hand side in Fig. 5.1 where  $\Psi_3 < \Psi_2$ . As the sine is an odd function, the mirrored configuration will lead to the same value of SPC, only with the inverted sign as the absolute value in difference between the two planes is equal, only differing in the sign. As both configurations are equally probable, the average of the sine term will thus trivially lead to zero.

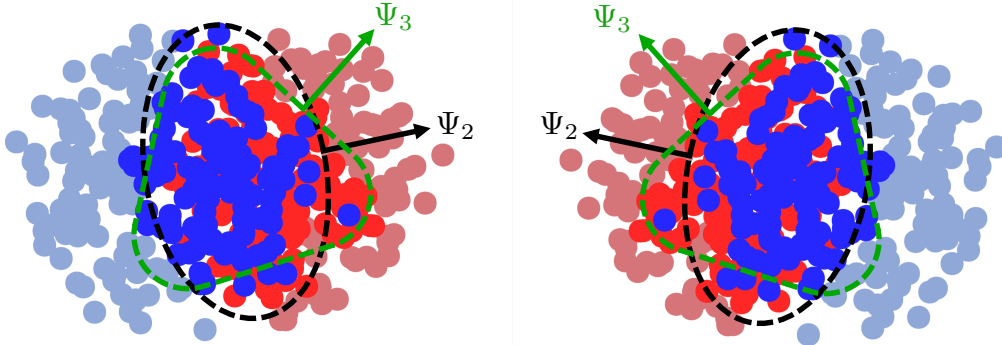


Figure 5.1: The SPC configuration on the left-hand side is as equally probable to the mirrored configuration on the right-hand side with an inverse sign in the difference of symmetry planes.

As the underlying p.d.f.  $P(\mathcal{R}, \Theta)$  is not known, it is approximated by a two-dimensional Gaussian distribution

$$\mathcal{N}(\mathcal{R}_x, \mathcal{R}_y) = \frac{1}{2\pi\sigma_x\sigma_y} \exp \left[ -\frac{(\mathcal{R}_x - \mu_x)^2}{2\sigma_x^2} - \frac{\mathcal{R}_y^2}{2\sigma_y^2} \right], \quad (5.6)$$

which is justified due to the Central Limit Theorem. In Eq. (5.6) the variables  $\mu_x = \langle \mathcal{R}_x \rangle$ ,  $\sigma_x^2 = \langle \mathcal{R}_x^2 \rangle - \langle \mathcal{R}_x \rangle^2$ , and  $\sigma_y^2 = \langle \mathcal{R}_y^2 \rangle$ , which are the mean and variance of the multi-harmonic variables respectively, have been introduced. In the next step, the radial part of this two-dimensional distribution is integrated out as only the symmetry planes are of interest. This leads to the spatial angular distribution

$$\mathcal{N}_\theta(\Theta) \equiv \int \mathcal{R} d\mathcal{R} \mathcal{N}(\mathcal{R}, \Theta) = \frac{\sigma_x^3 \sigma_y e^{-\mu_x^2/2\sigma_x^2}}{\pi \sigma_\theta^2} \left[ 1 + \frac{\sqrt{\pi} \mu_x \sigma_y e^{\mu_\theta^2}}{\sigma_\theta} [1 + \text{erf}(\mu_\theta)] \right], \quad (5.7)$$

where

$$\sigma_\theta(\Theta) = \sigma_x \sqrt{2\sigma_y^2 \cos^2 \Theta + 2\sigma_x^2 \sin^2 \Theta}, \quad \mu_\theta(\Theta) = \frac{\mu_x \sigma_y \cos \Theta}{\sigma_\theta}. \quad (5.8)$$

In Eq. (5.7), erf represents the Gauss error function. To obtain the new estimator for SPC, the distribution in Eq. (5.7) is used to calculate the average  $\langle \cos \Theta \rangle$ . The latter expression is of interest, as it represents the angular, real part of the experimentally usable multiparticle correlation techniques (see Sec. 2.2). Thus, the Gaussian Estimator for SPC is defined as

$$\langle \cos \Theta \rangle_{\text{GE}} = \int d\Theta \mathcal{N}_\theta(\Theta) \cos \Theta. \quad (5.9)$$

To find an analytic result for this estimator, additional approximations have to be made. Assuming that the fluctuations in  $x$  and  $y$  are of the same order  $\sigma_x \sim \sigma_y \sim \sigma_r/\sqrt{2}$  where  $\sigma_r = \sqrt{\sigma_x^2 + \sigma_y^2}$ , the  $\Theta$  dependence of  $\sigma_\theta$  in Eq. (5.8) cancels out. As such, one can expand Eq. (5.9) in terms of  $\mu_x/\sigma_r$  which gives the following, leading order expression for the GE estimator

$$\langle \cos \Theta \rangle_{\text{GE}} \simeq \sqrt{\frac{\pi}{4}} \left( \frac{\mu_x}{\sigma_r} \right). \quad (5.10)$$

Finally, this expression has to be translated into the original flow amplitudes and symmetry planes. Using the expressions from Eq. (5.4) and Eq. (5.5), one obtains the new estimator in terms of flow amplitudes and symmetry planes as

$$\langle \cos(a_1 n_1 \Psi_{n_1} + \dots + a_k n_k \Psi_{n_k}) \rangle_{\text{GE}} \simeq \sqrt{\frac{\pi}{4}} \frac{\langle v_{n_1}^{a_1} \dots v_{n_k}^{a_k} \cos(a_1 n_1 \Psi_{n_1} + \dots + a_k n_k \Psi_{n_k}) \rangle}{\sqrt{\langle v_{n_1}^{2a_1} \dots v_{n_k}^{2a_k} \rangle}}. \quad (5.11)$$

For the denominator in Eq. (5.11),  $\sigma_r = \sqrt{\langle \mathcal{R}_x^2 \rangle - \mu_x^2 + \langle \mathcal{R}_y^2 \rangle} \simeq \sqrt{\langle \mathcal{R}_x^2 \rangle + \langle \mathcal{R}_y^2 \rangle}$  has been made as an approximation, which has an error of  $(\mu_x/\sigma_r)^2$ . Besides the numerical factor of  $\sqrt{\pi/4}$ , the most notable difference between the Gaussian Estimator in Eq. (5.11) and the scalar product method from Eq. (5.3) is the joined mean of flow amplitudes in the denominator. Regarding the integers  $a_i$ , their choice is not arbitrary and has to follow a certain set of constraints, which are explained in detail in App. B.1.

### 5.1.3 Validation of the Gaussian Estimator

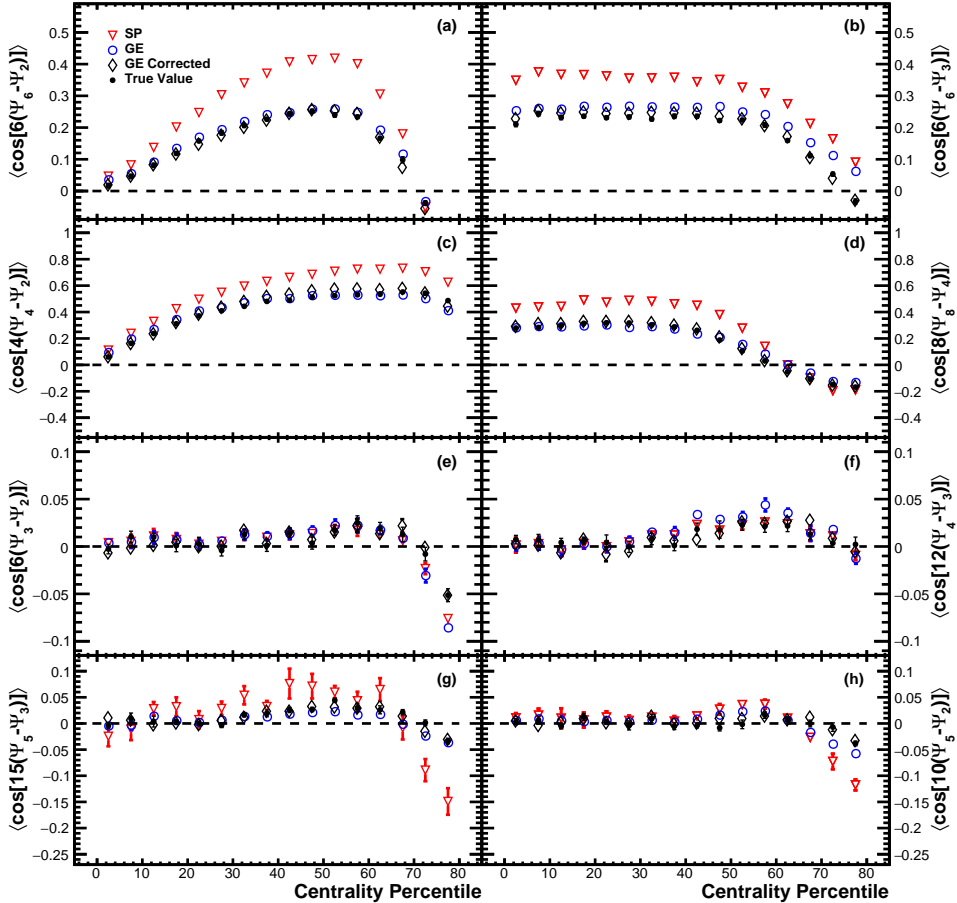


Figure 5.2: GE and SP method compared to the true value of correlation between two symmetry planes in iEBE-VISHNU.

To verify that the GE provides a better estimate of SPC in heavy-ion collisions, this new method is tested with the state-of-the-art realistic Monte Carlo generator iEBE-VISHNU with Monte Carlo Glauber as the initial state (see Sec. 3 for a detailed description of the models). As the used setup does not consider the system evolution in the hadronic

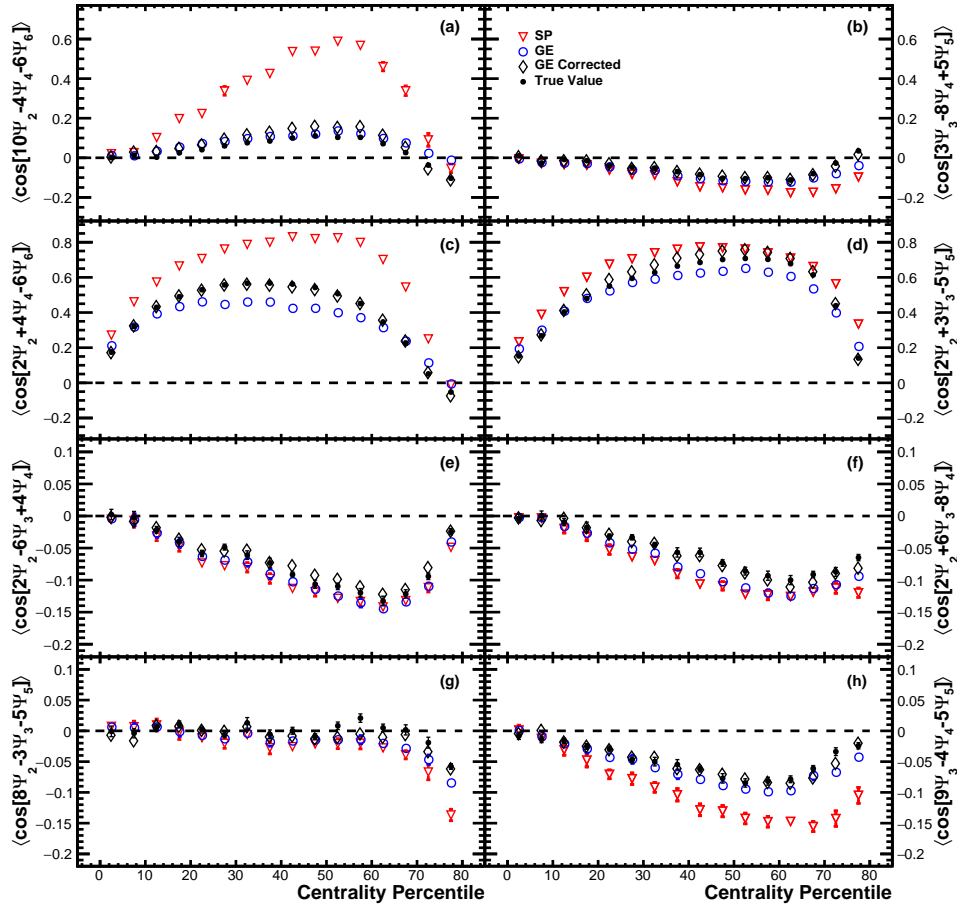


Figure 5.3: GE and SP method compared to the true value of correlation between three symmetry planes in iEBE-VISHNU.

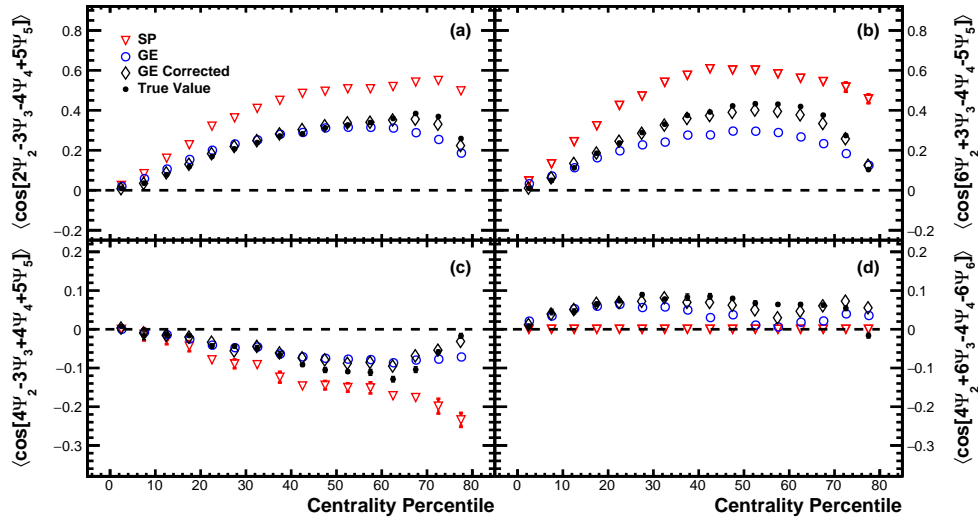


Figure 5.4: GE and SP method compared to the true value of correlation between four symmetry planes in iEBE-VISHNU.

stage, a precise event-by-event notion of symmetry planes and flow amplitudes is available within the model. As such, the SPC can directly be calculated on an event-by-event basis without the use of any estimator. These unbiased and directly obtained SPC values have been calculated per centrality bin and averaged over the available events. The result of this procedure is called the “true value”. In comparison to that, estimates of SPC using the

SP method (Eq. (5.3)) and the GE (Eq. (5.11)) are provided as a function of centrality. The results of this study for correlations between two, three and four symmetry planes are presented in Fig. 5.2, Fig. 5.3 and Fig. 5.4, respectively.

Focusing on the results for the SPC between two planes, it becomes obvious that the GE shows a great improvement when compared to the SP method. In the presented cases, the GE estimators reproduce the true value very well. This is especially true for SPC where the final state symmetry planes have a strong correlation due to the geometric relation from the initial state (e.g.  $\Psi_2$  and  $\Psi_4$ ). In cases where no such initial geometric correlation exists, the GE and SP method are comparable to each other. Considering further the study of correlations between three and four symmetry planes, the improvement of the GE estimator becomes even more evident. Overall, these studies demonstrate the huge bias introduced to the measurements by neglecting the correlations between flow amplitudes. However, in a few cases it is evident that the GE still deviates from the true value of SPC, as it can be seen for instance for  $\Theta = 2\Psi_2 + 3\Psi_3 - 5\Psi_5$  in Fig. 5.3 (d). In these cases, the initial assumption of the GE, namely the modelling of multi-harmonic flow fluctuations with a two-dimensional normal distribution, is violated. In [72], a conceptual event-shape-engineering approach for correcting these deviations from a Gaussian distribution is presented (called ‘‘GE Corrected’’ in the figures). The experimental feasibility of this approach is yet to be determined in a follow up study.

Besides the argumentation in [72], the difference between the GE and the true value, in particular for peripheral collisions, can be understood as follows: In the same way that the SP method has a bias from neglecting the correlations between the flow amplitudes, a small bias from neglecting the correlations between the amplitudes and symmetry planes in the numerator is left in the GE. It has to be noted that this bias is also present in the SP method. To demonstrate that the prefactor of amplitudes in the numerator and the difference of planes are correlated already in the initial state, the MuPa Glauber model is employed in the same setup as in its validation in Sec. 3.1.1. Figure 5.5 shows the correlations between  $\epsilon_2^2\epsilon_4$  and  $\Phi_4 - \Phi_2$  for the centrality ranges 0–5%, 20–30% and 50–60%. This kind of correlations have already been reported in [75] as a function of the impact parameter and dubbed ‘‘Wolverine Plots’’. As one can see, the distribution is uniform for very central collisions indicating uncorrelated amplitudes and phases, while correlations between them arise and become more and more pronounced with increasing centrality. The bias from factorising the numerator of the GE and SP method into the amplitude and phase part is thus expected to increase with the centrality as well. This explains the small deviation between the GE and the true value that is left in particular for large centralities.

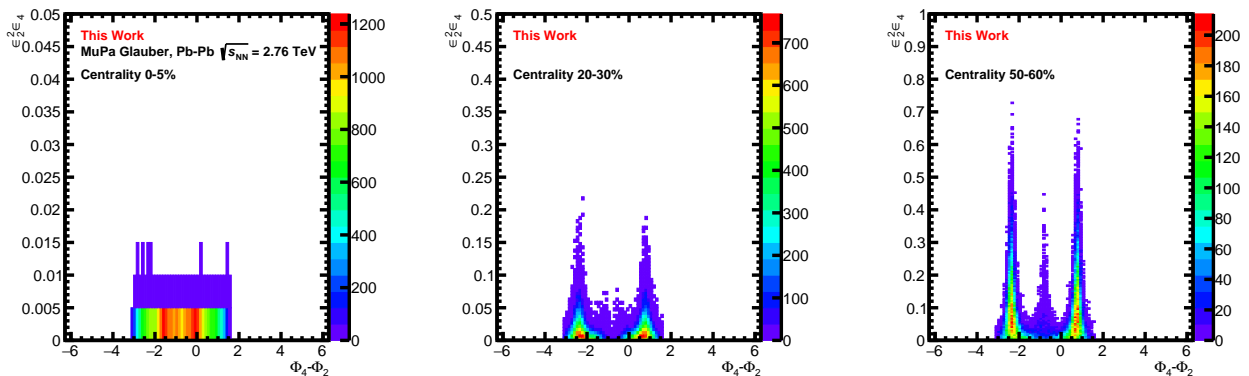


Figure 5.5: Correlation plots between  $\epsilon_2^2\epsilon_4$  and  $\Phi_4 - \Phi_2$  for the centrality ranges 0–5%, 20–30% and 50–60% obtained with the MuPa Glauber model.

## 5.2 Cumulants of SPC

This section will present a short overview of the cumulant formalism by Kubo [96], which is then applied to the concept of symmetry plane correlations. This leads to the definition of a new observable whose properties are tested with Toy Monte Carlo studies. All of the presented results of this section are based on [97] if not indicated otherwise.

### 5.2.1 Conceptual introduction to cumulants

<sup>1</sup>For the conceptual approach to cumulants, consider a general p.d.f.  $f(X_1, X_2)$  of two random variables  $X_1$  and  $X_2$ . This p.d.f. can be split into two contributions: first, the product of univariate p.d.f.  $f(X_1)f(X_2)$  where  $X_1$  and  $X_2$  are uncorrelated, and second a contribution that cannot be factorised due to the genuine correlation between the two variables (see Fig. 5.6).



Figure 5.6: Decomposition of a two particle distribution into the uncorrelated, single particle distributions and the distribution with the genuine correlation (indicated by the blue ellipse). Taken from [29].

The latter contribution is denoted by  $f_c(X_1, X_2)$ . This leads to the mathematical expression

$$f(X_1, X_2) = f(X_1)f(X_2) + f_c(X_1, X_2), \quad (5.12)$$

where it has been used that for a univariate p.d.f. the correlated term is always equal to the p.d.f. itself, i.e.  $f(X_i) = f_c(X_i)$ . The term  $f_c(X_1, X_2)$  is the so-called cumulant which can be measured by reordering Eq. (5.12) into

$$f_c(X_1, X_2) = f(X_1, X_2) - f(X_1)f(X_2). \quad (5.13)$$

The cumulant is thus obtained by subtracting all lower order contributions (in this case the univariate p.d.f.  $f(X_1)$  and  $f(X_2)$ ) from the two-variate p.d.f.  $f(X_1, X_2)$ . As such, the cumulant  $f_c(X_1, X_2)$  represents the *genuine correlation* between the two variables  $X_1$  and  $X_2$ .

### 5.2.2 Cumulant formalism according to Kubo

After the conceptual introduction of cumulants, this subsection describes the mathematical formalism of cumulants based on the work of Kubo [96]. The notation used in this subsection is based on [97].

Consider a general multivariate p.d.f.  $f(X_1, \dots, X_N)$  for  $N$  random variables  $X_1, \dots, X_N$ . This p.d.f. can in general be fully described by its moments

$$\mu_{\nu_1, \dots, \nu_N} = \int X_1^{\nu_1} \cdots X_N^{\nu_N} f(X_1, \dots, X_N) dX_1 \cdots dX_N. \quad (5.14)$$

The notations

$$\mu_{\nu_1, \dots, \nu_N} \equiv \langle X_1^{\nu_1} \cdots X_N^{\nu_N} \rangle \quad (5.15)$$

<sup>1</sup>This subsection is based on [29].

will be equally used throughout this section. As an alternative to Eq. (5.14), the moments  $\mu_{\nu_1, \dots, \nu_N}$  can be obtained via the *moment generating function*  $M(\xi_1, \dots, \xi_N)$ , which is defined as

$$M(\xi_1, \dots, \xi_N) = \langle e^{\sum_{j=1}^N \xi_j X_j} \rangle. \quad (5.16)$$

To calculate the moments,  $M(\xi_1, \dots, \xi_N)$  has to be differentiated and evaluated in the following way

$$\mu_{\nu_1, \dots, \nu_N} = \frac{\partial^{\nu_1}}{\partial \xi_1^{\nu_1}} \cdots \frac{\partial^{\nu_N}}{\partial \xi_N^{\nu_N}} M(\xi_1, \dots, \xi_N) \Big|_{\xi_1 = \dots = \xi_N = 0}. \quad (5.17)$$

Alternatively, the p.d.f.  $f(X_1, \dots, X_N)$  can be studied via its cumulants, which will be denoted by the two following expressions equivalently

$$\kappa_{\nu_1, \dots, \nu_N} \equiv \langle X_1^{\nu_1} \cdots X_N^{\nu_N} \rangle. \quad (5.18)$$

Two of the advantages of cumulants are that their higher orders are not influenced by lower order contributions as it is the case for the moments, and cumulants have in general a smaller sample variance [98]. They are obtained via the *cumulant generating function*  $K(\nu_1, \dots, \nu_N)$  introduced as

$$K(\nu_1, \dots, \nu_N) = \ln M(\xi_1, \dots, \xi_N). \quad (5.19)$$

Using Eq. (5.19), the cumulants  $\kappa_{\nu_1, \dots, \nu_N}$  are then derived as

$$\kappa_{\nu_1, \dots, \nu_N} = \frac{\partial^{\nu_1}}{\partial \xi_1^{\nu_1}} \cdots \frac{\partial^{\nu_N}}{\partial \xi_N^{\nu_N}} K(\xi_1, \dots, \xi_N) \Big|_{\xi_1 = \dots = \xi_N = 0}. \quad (5.20)$$

In the univariate case, one obtains for the first two orders of cumulants

$$\kappa_1 = \mu_1, \quad (5.21)$$

$$\kappa_2 = \mu_2 - \mu_1^2, \quad (5.22)$$

where it becomes obvious that  $\kappa_1$  is just the mean while  $\kappa_2$  is the variance of the random variable. In the two-variate case, the first three cumulants are

$$\kappa_{1,1} = \mu_{1,1} - \mu_{0,1}\mu_{1,0}, \quad (5.23)$$

$$\kappa_{1,2} = \mu_{1,2} - \mu_{0,2}\mu_{1,0} - 2\mu_{1,1}\mu_{0,1} + 2\mu_{1,0}\mu_{0,1}^2, \quad (5.24)$$

$$\kappa_{2,1} = \mu_{2,1} - \mu_{2,0}\mu_{0,1} - 2\mu_{1,0}\mu_{1,1} + 2\mu_{1,0}^2\mu_{0,1}. \quad (5.25)$$

While these expressions are directly derived from the cumulant generating function, other expressions might be considered to be cumulants. However, these expressions have to be tested, as cumulants fulfil by definition the following properties:

1. *Statistical independence.* If the statistical variables  $X_1, \dots, X_N$  can be divided into at least two statistically independent subgroups, the cumulant  $\kappa_{\nu_1, \dots, \nu_N}$  will be zero. Thus, a cumulant can only lead to a non-zero result if all involved variables are genuinely correlated to each other.
2. *Reduction.* In case that some of the random observables  $X_1, \dots, X_N$  in the cumulant expression are identical, the cumulant will be of lower order, i.e.

$$\kappa_{\nu_1, \dots, \nu_N} = \langle X_1^{\nu_1} \cdots X_N^{\nu_N} \rangle_c = \langle X_1^{\tilde{\nu}_1} \cdots X_M^{\tilde{\nu}_M} \rangle_c = \kappa_{\tilde{\nu}_1, \dots, \tilde{\nu}_M}. \quad (5.26)$$

In the last equation,  $M < N$ , and  $\tilde{\nu}_i$  represents the sum over all exponents of distinct  $X_i$  in the initial cumulant. As an example, consider that all variables  $X_1, \dots, X_N$  are the same and equal to  $X$ . The initial multivariate cumulant can thus be expressed as a lower univariate cumulant of  $X$  of order  $\nu_1 + \dots + \nu_N$ :

$$\kappa_{\nu_1, \dots, \nu_N} = \langle X_1^{\nu_1} \cdots X_N^{\nu_N} \rangle_c = \langle X^{\nu_1 + \dots + \nu_N} \rangle_c = \kappa_{\nu_1 + \dots + \nu_N}. \quad (5.27)$$

3. *Semi-invariance.* If a multivariate cumulant  $\kappa_{\nu_1, \dots, \nu_N}$  has at least one index  $\nu_i \geq 2$  or minimum two indices equal to 1 (i.e. if  $\sum_i \nu_i \geq 2$ ), the following expressions holds true

$$\kappa((X_1 + c_1)^{\nu_1}, \dots, (X_N + c_N)^{\nu_N}) = \kappa(X_1^{\nu_1}, \dots, X_N^{\nu_N}), \quad \sum_i \nu_i \geq 2. \quad (5.28)$$

In Eq. (5.28)  $c_1, \dots, c_N$  are constants. In particular, it follows that all univariate cumulants of order  $\nu \geq 2$  are shift-invariant for any constant  $c$ :

$$\kappa((X + c)^\nu) = \kappa(X^\nu), \quad \forall \nu \geq 2. \quad (5.29)$$

This semi-invariance is only broken for first order cumulants where the relation  $\kappa(X + c) = c + \kappa(X)$  is satisfied instead.

4. *Homogeneity.* For a general set of constants  $c_1, \dots, c_N$ , the cumulant satisfies

$$\kappa((c_1 X_1)^{\nu_1}, \dots, (c_N X_N)^{\nu_N}) = c_1^{\nu_1} \dots c_N^{\nu_N} \kappa(X_1^{\nu_1}, \dots, X_N^{\nu_N}). \quad (5.30)$$

5. *Multilinearity.* Consider a random variable  $Z_1$  that is a linear combination of variables  $X_i$ , i.e.

$$Z_1 = \sum_i X_i. \quad (5.31)$$

Then, the multivariate cumulant for  $Z_1, \dots, Z_N$  can be rewritten as

$$\kappa(\sum_i X_i, Z_2^{\nu_2}, \dots, Z_N^{\nu_N}) = \sum_i \kappa(X_i, Z_2^{\nu_2}, \dots, Z_N^{\nu_N}). \quad (5.32)$$

This can be generalised in the case where multiple variables are linear.

6. *Additivity.* If a set of random variables  $X_i$  are statistically independent observables, the  $N$ th-order cumulant of their sum is equal to the sum of their  $N$ th-order cumulants, i.e.

$$\kappa((\sum_i X_i)^N) = \sum_i \kappa(X_i^N). \quad (5.33)$$

The proofs for all of these properties can be found in [97]. If a expression violates one of the presented properties characteristic to cumulants, the expression is not a valid cumulant.

### 5.2.3 New formalism for cumulants of SPC

For flow analysis, the cumulant provided in [52, 59, 60] is based on the expansion on azimuthal angles and has been found to suppress the non-flow contribution in flow analysis. While the used formalism has been criticised for violating some of the cumulant properties [97], the expression was well studied and understood, providing important new insights into flow. Another important cumulants utilised in flow analysis are the symmetric cumulants [55], which are able to measure the genuine correlation between two flow amplitudes by using  $v_n^2$  and  $v_m^2$  as the basic observables in  $\kappa_{1,1}$ . The measurement of these symmetric cumulants provided important information on the temperature dependence of the shear viscosity of entropy density ratio  $\eta/s$ . The formalism of symmetric cumulants has been generalised to higher orders [58] with the first measurements of the genuine correlation between three flow amplitudes provided in [62].

The described cumulants either used azimuthal angles  $\varphi$  or the flow amplitudes as stochastic variables in the cumulant expansion. However, here the cumulant expansion based on symmetry planes is explained as it was introduced in [97]. This formalism provides the first proper cumulant expansion using only symmetry planes, which are the second degree of freedom used in the characterisation of the anisotropic flow p.d.f. Eq. (2.15). Thus, the cumulants of symmetry planes have the potential of providing further information compared to SPC.

Unlike the flow amplitudes  $v_n$ , the symmetry planes  $\Psi_n$  are affected by the random event-by-event fluctuations of the reaction plane. As such, when one expands the cumulant on observables that are not invariant under these random shifts, the single means will trivially lead to zero making the cumulant expression useless. Due to this requirement of rotational invariance and further to the accessibility by multiparticle correlation techniques, the only proper choice of stochastic observables are those who contain isotropic sums of symmetry planes. The following two observables  $X_1$  and  $X_2$  contain each two symmetry planes and, are thus the simplest possible observable satisfying the described requirements

$$X_1 = e^{ib(\Psi_c - \Psi_d)}, \quad (5.34)$$

$$X_2 = e^{ik(\Psi_l - \Psi_m)}. \quad (5.35)$$

In the definition of  $X_1$  and  $X_2$  above, it was assumed that  $b$  and  $k$  are non-zero, positive integers and that no symmetry plane cancels out if the product  $X_1 \cdot X_2$  is taken. To write the differences of symmetry planes in a more compact form, the following abbreviations are introduced

$$\delta_{c,d} \equiv \Psi_c - \Psi_d, \quad (5.36)$$

$$\delta_{l,m} \equiv \Psi_l - \Psi_m. \quad (5.37)$$

As such,  $X_1$  and  $X_2$  can be written as

$$X_1 = e^{ib\delta_{c,d}}, \quad (5.38)$$

$$X_2 = e^{ik\delta_{l,m}}. \quad (5.39)$$

Inserting these two stochastic observables into the expression of the two-variate cumulant  $\kappa_{1,1}$  in Eq. (5.23) leads to

$$\text{CSC}(b\delta_{c,d}, k\delta_{l,m}) = \left\langle e^{i(b\delta_{c,d} + k\delta_{l,m})} \right\rangle - \langle e^{ib\delta_{c,d}} \rangle \langle e^{ik\delta_{l,m}} \rangle, \quad (5.40)$$

which is the simplest possible *Cumulant of Symmetry Plane Correlations* (CSC). This cumulant is rotationally invariant and fulfils all needed cumulant properties as it is demonstrated in App. B.2. The interpretation of Eq. (5.40) can be rather complex, thus the focus here lies on the case where all involved symmetry planes are different from each other (i.e.  $\Psi_c \neq \Psi_d \neq \Psi_l \neq \Psi_m$ ). In this case, the cumulant in Eq. (5.40) consists by definition of two distinct isotropic terms in the joined mean. To further understand the properties of this specific cumulant, the following cases have to be considered:

1. All involved symmetry planes are completely uncorrelated, i.e. the symmetry plane correlations  $\delta_{c,d}$  and  $\delta_{l,m}$  fluctuate randomly and independently from each other. The cumulant leads to zero.
2. The symmetry plane correlations  $\delta_{c,d}$  and  $\delta_{l,m}$  are constant and independent of each other. Equation (5.40) yields zero.

3. The symmetry plane  $\Psi_c$  is correlated to  $\Psi_d$ , as well as  $\Psi_l$  to  $\Psi_m$ . However, the correlations  $\delta_{c,d}$  and  $\delta_{l,m}$  fluctuate independently from each other. Equation (5.40) yields zero.
4. The SPC  $\delta_{c,d}$  and  $\delta_{l,m}$  are genuinely correlated to each other. The cumulant defined in Eq. (5.40) yields a non-zero value.

Based on these exemplary scenarios, the cumulant Eq. (5.40) cannot be understood as a cumulant of symmetry planes but only as a cumulant of symmetry plane *correlations*. This is not surprising as the fundamental stochastic observable in the cumulant expansion is the isotropic sum of symmetry planes. While SPC can be seen as a static observable, which tells whether symmetry planes are correlated (and if so to which extent), the CSC captures more of their dynamics telling how SPC behave and evolve relative to each other.

To test if the cumulant expression Eq. (5.40) has the expected behaviour, a Toy Monte Carlo (TMC) study is used. In such a study, a p.d.f. similar to Eq. (2.15) is used to generate azimuthal angles per event with a given multiplicity  $M$ . The involved flow amplitudes and symmetry planes that characterise the p.d.f. Eq. (2.15) can fluctuate on an event basis in a predefined way. As such, one knows the exact input values and input correlations of the p.d.f. used to generate the azimuthal angles  $\varphi$ . After the generation of the azimuthal angles, the multiparticle correlation techniques are used to calculate the desired quantities which then can be averaged over many events.

In this TMC, a p.d.f. of the form

$$f(\varphi) = \frac{1}{2\pi} [1 + 2(v_1 \cos[(\varphi - \Psi_1)] + v_2 \cos[2(\varphi - \Psi_2)] + v_3 \cos[3(\varphi - \Psi_3)] + v_4 \cos[4(\varphi - \Psi_4)] + v_5 \cos[5(\varphi - \Psi_5)] + v_6 \cos[6(\varphi - \Psi_6)])] \quad (5.41)$$

is used for the study of the four different scenarios presented above using the exemplary CSC

$$\begin{aligned} \text{CSC}(4\delta_{4,2}, 6\delta_{6,3}) &= \langle e^{i(4\delta_{4,2} + 6\delta_{6,3})} \rangle - \langle e^{i4\delta_{4,2}} \rangle \langle e^{i6\delta_{6,3}} \rangle \\ &= \langle e^{i(4(\Psi_4 - \Psi_2) + 6(\Psi_6 - \Psi_3))} \rangle - \langle e^{i4(\Psi_4 - \Psi_2)} \rangle \langle e^{i6(\Psi_6 - \Psi_3)} \rangle. \end{aligned} \quad (5.42)$$

In particular, the following choices are made for the event-by-event fluctuations of the symmetry planes which correspond to the presented cases before:

1. All involved symmetry planes  $\Psi_2$ ,  $\Psi_3$ ,  $\Psi_4$  and  $\Psi_6$  fluctuate independently from each other within  $[0, 2\pi)$ . Thus,  $\delta_{4,2}$  and  $\delta_{6,3}$  fluctuate randomly and uncorrelated in the interval  $[0, 2\pi)$ .
2.  $\Psi_2$  fluctuates randomly in the interval with  $[0, 2\pi)$  and  $\Psi_4 = \Psi_2 + \frac{\pi}{12}$  leading to a constant correlation between those planes  $\delta_{4,2} = \frac{\pi}{12} = \text{const}$ . The symmetry plane  $\Psi_3$  fluctuates with  $\Psi_3 \in [0, 2\pi)$  and  $\Psi_6 = \Psi_3 + \frac{\pi}{18}$  such that  $\delta_{6,3} = \frac{\pi}{18} = \text{const}$ . represents a constant correlation as well. However, the two SPC are independent from each other.
3.  $\Psi_2$  fluctuates according to  $\Psi_2 \in [0, 2\pi)$  and  $\Psi_4 = \Psi_2 + a$  with  $a$  a random number  $a \in [0, \frac{\pi}{12}]$ . Similarly,  $\Psi_3$  fluctuates randomly in the interval with  $[0, 2\pi)$  and  $\Psi_6 = \Psi_3 + b$  with  $b \in [0, \frac{\pi}{18}]$ . Again, the two SPC are uncorrelated to each other.
4.  $\Psi_2$  is chosen according to the uniform distribution  $\Psi_2 \in [0, 2\pi)$  and  $\Psi_4 = \Psi_2 + a$  with fluctuating  $a \in [0, \frac{\pi}{12}]$ .  $\Psi_3$  is fluctuating with  $\Psi_3 \in [0, 2\pi)$  and  $\Psi_6 = \Psi_3 + a + \frac{\pi}{6\sqrt{2}}$  with  $a$  having the same value per event as for  $\delta_{4,2}$ . As such, the two SPC are correlated to each other as  $\delta_{4,2}$  also determines the value of  $\delta_{6,3}$ .

If, during the sampling, a symmetry plane  $\Psi_j = \Psi_i + h$  ( $h$  is a constant and  $\Psi_i \in [0, 2\pi)$ ) turns out to be greater than  $2\pi$ , it is brought back to the interval between 0 and  $2\pi$ . Overall, the study is conducted in bins of fixed multiplicities of  $M = 50, 100, 250, 500, 750, 1000$  with in total  $N_{ev} = 10^8$  events for each multiplicity.

As there is no exact way for measuring SPC using multiparticle correlation techniques, a trick is used to obtain the behaviour of the CSC without the influence of the flow amplitudes. In Eq. (5.41), all flow amplitudes are set to a constant value, which does not change between the events, in particular  $v_1 = v_5 = 0$  and  $v_2 = v_3 = v_4 = v_6 = 0.1$ . As such one can measure the quantities

$$\langle v_2^2 v_3^2 v_4 v_6 e^{i(4\delta_{4,2} + 6\delta_{6,3})} \rangle, \quad (5.43)$$

$$\langle v_2^2 v_4 e^{i4\delta_{4,2}} \rangle, \quad (5.44)$$

$$\langle v_3^2 v_6 e^{i6\delta_{6,3}} \rangle, \quad (5.45)$$

as they are accessible by multiparticle correlation techniques. Afterwards, the constant prefactor of flow amplitudes is divided out leaving the pure contribution of symmetry planes.

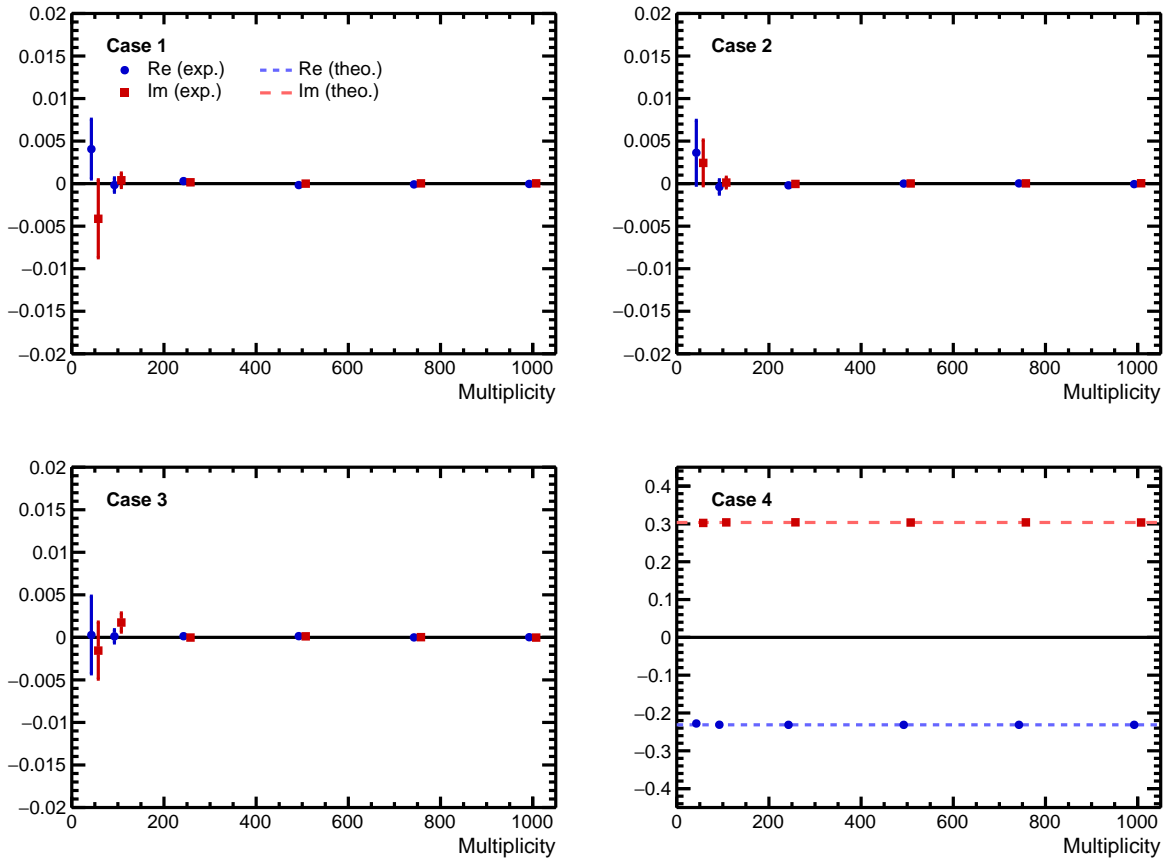


Figure 5.7: Outcome of the TMC for the 4 scenarios of CSC, taken from [97].

The results of the TMC in Fig. 5.7 demonstrate that the CSC indeed has the expected cumulant properties. The CSC is zero in all the cases where no genuine correlation between the SPC is present, while it exhibits a non-zero value in case of a genuine correlation. As such, the CSC is a valid cumulant of symmetry plane correlations.

In addition to the presented TMC studies, a realistic model consisting of Monte Carlo Glauber for the initial state and iEBE-VISHNU for the hydrodynamic evolution (see

Sec. 3.3 for details) has been employed in [97] to study the CSC. In particular, the real part of the two combinations

$$\text{CSC}(4\delta_{4,2}, 6\delta_{6,3}) = \langle e^{i4(\Psi_4 - \Psi_2) + i6(\Psi_6 - \Psi_3)} \rangle - \langle e^{i4(\Psi_4 - \Psi_2)} \rangle \langle e^{i6(\Psi_6 - \Psi_3)} \rangle, \quad (5.46)$$

$$\text{CSC}(6\delta_{6,2}, 8\delta_{8,4}) = \langle e^{i6(\Psi_6 - \Psi_2) + i8(\Psi_8 - \Psi_4)} \rangle - \langle e^{i6(\Psi_6 - \Psi_2)} \rangle \langle e^{i8(\Psi_8 - \Psi_4)} \rangle, \quad (5.47)$$

has been investigated for the initial state given by the participant planes and the final state given by the symmetry planes. As one can see in Fig. 5.8, a non-trivial relation between the initial and final state emerges. For the cumulant  $\text{CSC}(4\delta_{4,2}, 6\delta_{6,3})$ , the SPC  $\delta_{4,2}$  and  $\delta_{6,3}$  seem to be anticorrelated for peripheral collisions in the initial state, while this signal changes its sign for the final state. For  $\text{CSC}(6\delta_{6,2}, 8\delta_{8,4})$ , the initial state shows only weak correlations between the evolved planes, while a strongly correlated signal can be observed for the final state for mid-central collisions. These non-trivial signals promise access to new information on the hydrodynamic evolution of the system and will be investigated further in future studies.

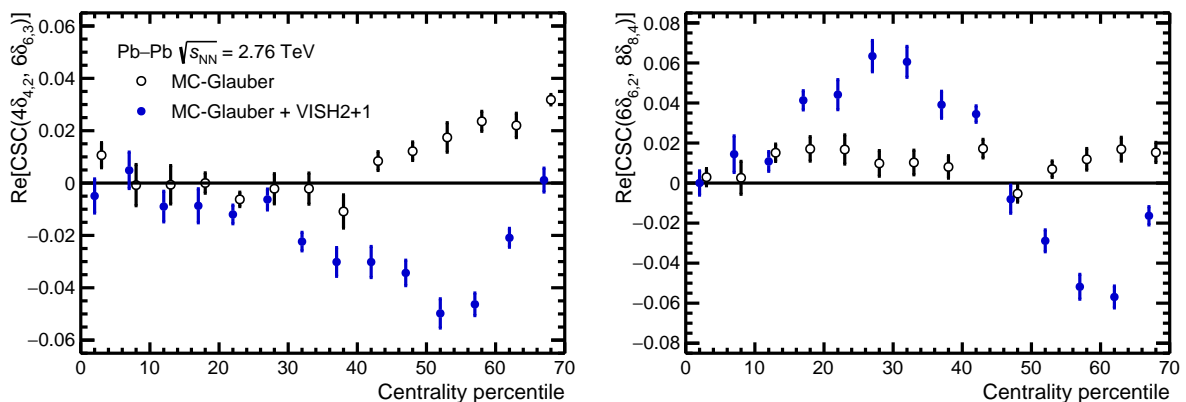


Figure 5.8: Study of  $\text{CSC}(4\delta_{4,2}, 6\delta_{6,3})$  and  $\text{CSC}(6\delta_{6,2}, 8\delta_{8,4})$  given by MC-Glauber and iEBE-VISHNU, taken from [97].



# Chapter 6

## Experimental data analysis

For this analysis, Pb–Pb data at a centre of mass energy of  $\sqrt{s_{\text{NN}}} = 2.76$  TeV recorded by the ALICE detector in 2010 is used. This data set is particularly suitable for the study of anisotropic flow due to the uniform azimuthal acceptance in the transverse plane, especially when using tracks reconstructed only by the TPC. Additionally, the data is not affected by pileup or charge distortions in the TPC, as it was at larger Run 2 energies. Overall, 84 runs have been included in this analysis with a total of  $7.36 \times 10^6$  events after selection in the centrality range of 0–50 %.

### 6.1 Event selection

Considering a collision, one can classify the event by two global properties: the *primary vertex*  $PV$ , which is the location of the initial collision within the ALICE detector and the centrality. Additionally, one has to take into consideration how the event has been triggered for recording, as well as potential reconstruction inefficiencies in the event classification. All of these quantities and their selection criteria are explained in the following subsections with a summary of the default selection values provided in Tab. 6.1.

Table 6.1: Summary of the default event selection criteria.

Property	Selection Criterion
Trigger	Minimum Bias (kMB)
Centrality Estimator	SPD Clusters ( $CL1$ )
Primary vertex in $z$ direction	$ PV_z  < 10$ cm
High multiplicity outliers	$M_{TPC} < 1.54M_{gl} - 65.00$ $M_{TPC} > 2.30M_{gl} + 90.00$
Event multiplicity of passed tracks	$M \geq 14$

#### 6.1.1 Primary vertex selection

The  $PV$  represents the main interaction location at which the two heavy ions collide. By definition, the nominal zero point of the primary vertex along the beam axis  $PV_z$  is located at the middle of the ALICE detector in longitudinal direction. As the colliding lead bunches are not localised at one common position along the beam axis, collisions do not only occur at  $PV_z = 0$  cm, but might be shifted along the  $z$  axis towards one side of ALICE. Thus, collisions might happen close to the edge of the detector in which case

not all produced charged particles can be detected, which leads to a biased multiplicity, and thus a biased centrality of the event. Therefore, a cut along the primary vertex in  $z$  direction has to be used. Restricting the collisions to  $|PV_z| < 10$  cm (i.e. to the region  $\pm 10$  cm around  $PV_z = 0$  cm) allows for a full acceptance of the ITS and a coverage of the TPC of  $|\eta| < 0.9$ . This is of importance as the ITS is used for centrality determination and as such the misidentification of events due to only a partial reconstruction is avoided by this criterion.

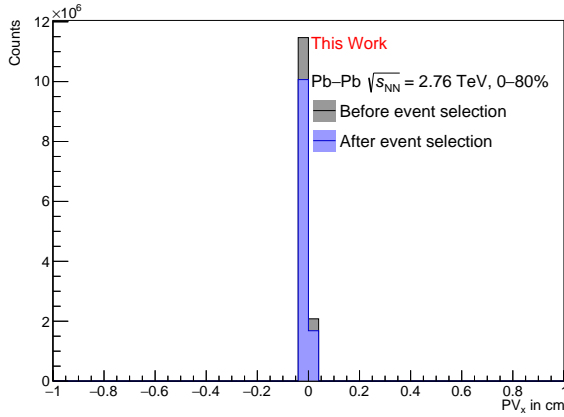


Figure 6.1: Distribution of  $PV_x$  before and after the event selection.

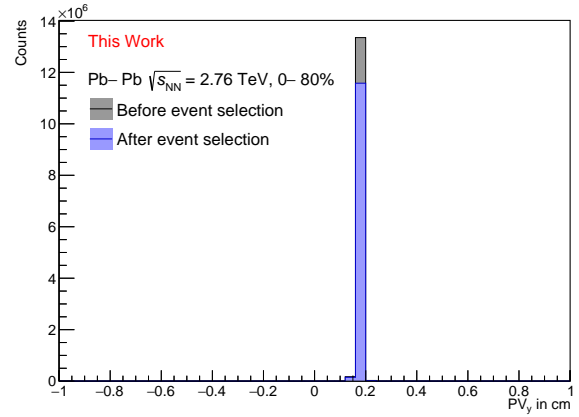


Figure 6.2: Distribution of  $PV_y$  before and after the event selection.

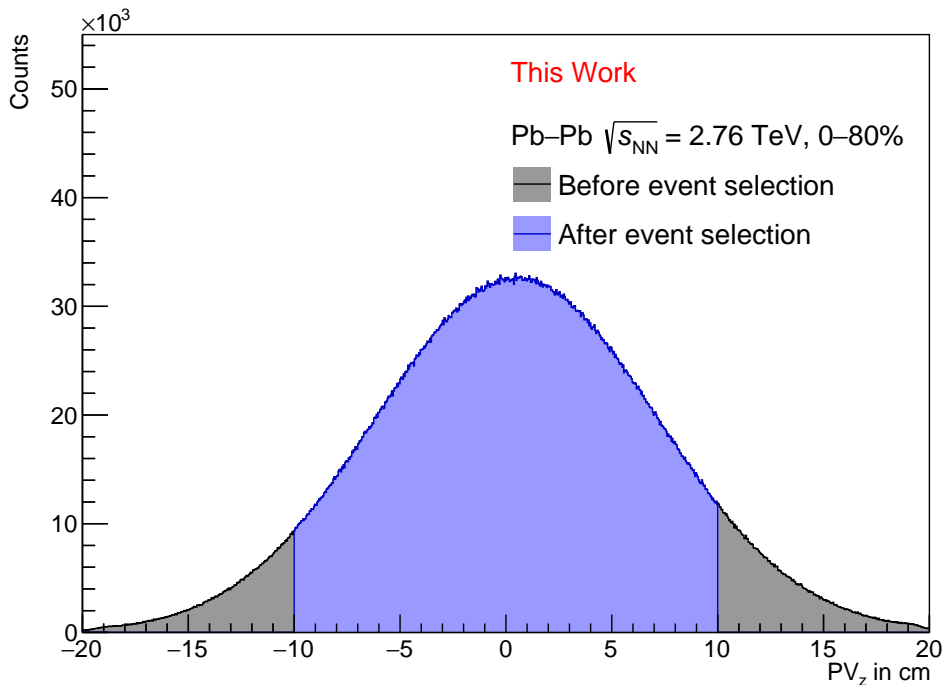


Figure 6.3: Distribution of  $PV_z$  before and after the event selection.

Analogous to the primary vertex in  $z$  direction,  $PV_x$  and  $PV_y$  represent the primary vertex in  $x$  and  $y$  direction respectively. As the beams are focussed very precisely in the transverse plane, the distribution of  $PV_x$  and  $PV_y$  are well defined and have a sharp peak. As such, no further selection criteria are applied for  $PV_x$  and  $PV_y$ . The distribution of

events in respect to the primary vertex in  $x$ ,  $y$  and  $z$  before and after the application of the PV selection can be seen in Fig. 6.1, Fig. 6.2 and Fig. 6.3 respectively.

### 6.1.2 Triggering, centrality and multiplicity selection

The events have been triggered to the condition of being *minimum bias* events (abbreviated by “kMB”). This trigger selects the events based on a simultaneous detection by two out of the following three detectors: the V0A, the V0C and the SPD. This guaranties that trigger efficiency for hadronic interactions is maximised.

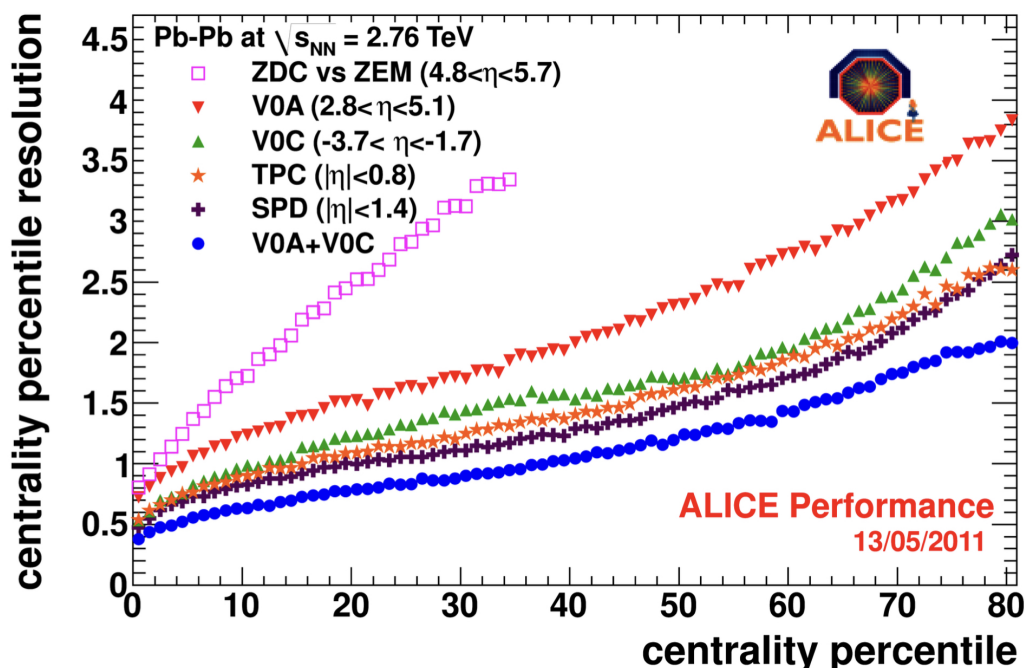


Figure 6.4: Performance of various ALICE centrality estimators, taken from [99].

After the triggering of the event, one of the most important event classifications is the centrality determination. Most commonly in ALICE, the V0M is used for this task as it has the best centrality resolution compared to the other estimators (see Fig. 6.4). However, as it was reported in [29], the V0M has additional problems with the so-called *high multiplicity outliers* (HMOs), which will be explained further in Sec. 6.1.3. Thus, the centrality determination by SPD clusters ( $CL1$ ) is used in this analysis. This method has a slightly worse centrality resolution of 0.5 – 2.5% compared to 0.5 – 2% of the V0M. This is however negligible, especially compared to the effects of not removing the high multiplicity outliers.

Lastly, one has to take into consideration the multiplicity of final state particles after application of the track selection. Considering a  $k$ -particle correlators one has to detect at least  $k$  final particles in the event. Given the fact the analysis of SPC requires up to 12-particle correlators, and later possibly 14-particle correlators, a minimum of 14 final-state particles is needed. As such, events that have a multiplicity  $M$  less than 14 tracks passing the track selection described in Sec. 6.2 are disregarded. This cut however impacts only very peripheral collisions.

### 6.1.3 Removal of the high multiplicity outliers

As discussed above, the classification of the event centrality is related to the amount of produced particles. Therefore, one expects to have a high multiplicity for the most central collisions, while mid-central and peripheral collisions have in general lower multiplicities. However, the reconstruction of the centrality and its connection to the multiplicity is not perfect. Thus, there exist events in mid-central and peripheral collisions with an abnormally large multiplicity compared to what is expected in their centrality range. These events are the so-called high multiplicity outliers, which were studied in detail in [29]. The amount of these HMOs is on the per-mill level and their effect is for most analyses negligible. This, however, is not true for flow analyses due to the multiplicity weights used in the all-event averages. In this case, the HMO events will overweight the healthy events of lower multiplicity.

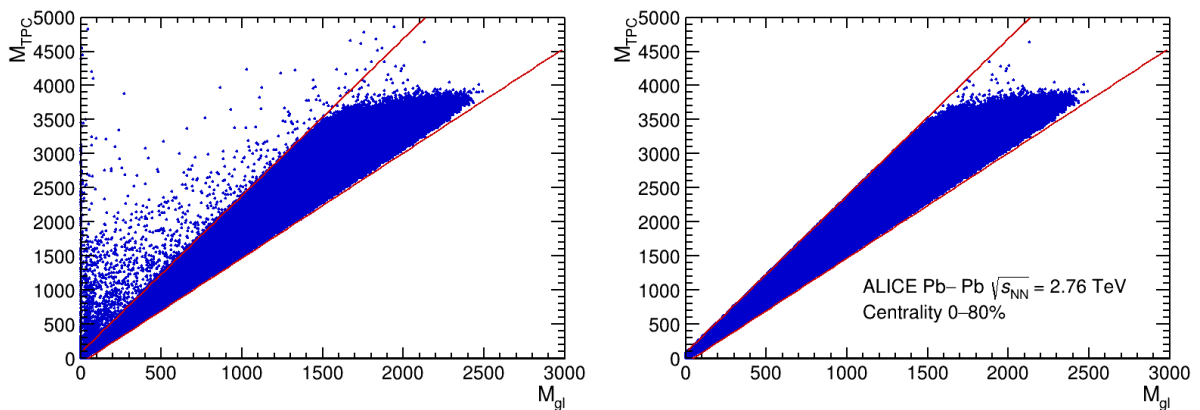


Figure 6.5: Multiplicity of global hybrid versus TPC-only tracks before (left) and after (right) application of the HMO cuts. Taken from [29].

To remove these HMOs, the approach used in [29] is employed. Here, the multiplicity of the global hybrid filterbit and the TPC-only filterbit are compared to each other. Using this histogram, two criteria are introduced as

$$M_{TPC} < 1.54M_{gl} - 65.00, \quad (6.1)$$

$$M_{TPC} > 2.30M_{gl} + 90.00. \quad (6.2)$$

Only events fulfilling these criteria are further used for the analysis (see Fig. 6.5). The effect on the multiplicity distributions can be seen in Fig. 6.6 and Fig. 6.7, which show the multiplicity distribution for the event centrality 40–50 % without and with the application of the HMO cut. As one can see in Fig. 6.6, a few events with abnormally large multiplicity are present when no HMO cut is applied, while these events are removed by the application of the cut (Fig. 6.7).

## 6.2 Track selection

Regarding the track selection, one has to consider the basic kinematic properties of a track, namely its transverse momentum  $p_T$ , its pseudorapidity  $\eta$  as well as its distance of closest approach to the primary vertex. Additionally, depending on the subdetectors used for the track reconstruction, different cuts have to be applied to assure a high quality of track reconstruction. A summary of the applied track selection criteria is provided in Tab. 6.2.

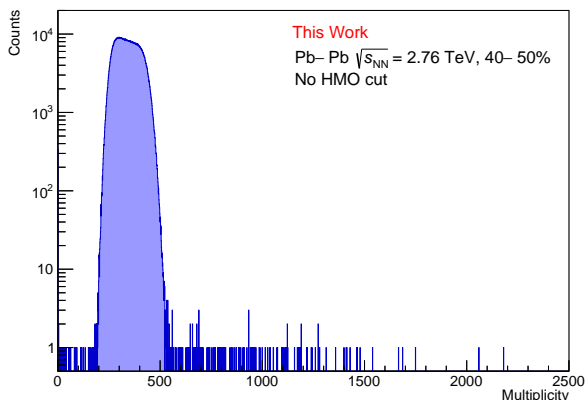


Figure 6.6: Multiplicity distribution after the track selection without the application of the HMO cut.

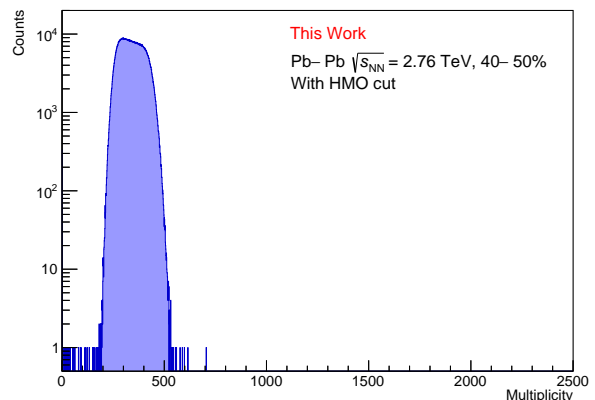


Figure 6.7: Multiplicity distribution after the track selection with the application of the HMO cut.

Table 6.2: Summary of the default track selection criteria.

Quantity	Selection Criterion
Filterbit	128 (TPC-only)
Transverse Momentum	$p_T \in [0.2, 5.0]$ GeV/ $c$
Pseudorapidity	$ \eta  < 0.8$
Distance of closest approach in $z$ direction	$ DCA_z  < 3.2$ cm
Distance of closest approach in $xy$ direction	$ DCA_{xy}  < 2.4$ cm
Number of TPC clusters	$N_{TPC} > 70$
$\chi^2$ per TPC cluster	$\chi^2/N_{TPC} \in [0.3, 4.0]$

## 6.2.1 Reconstruction selection

For this analysis, the TPC has been used as the main detector for track reconstruction. This is ensured by applying the so-called *filterbit* 128 to use only tracks reconstructed with the information provided by the TPC. Using these TPC-only tracks has the advantage of a great uniform acceptance, as shown in Fig. 6.8. There, the distribution of azimuthal angles  $\varphi$  becomes perfectly flat after the track selection and application of the filterbit.

Concerning the track reconstruction itself, two main quantities have to be considered. First is the number of TPC clusters  $N_{TPC}$ , which represents the amount of clusters that have been used in the track reconstruction. In the TPC, up to 159 clusters can be used for this task. Naturally, the quality of the reconstructed track becomes higher if more clusters are used for its reconstruction. For this analysis, a minimum of 70 TPC clusters are required to ensure a good track quality in this regard (see Fig. 6.9). This minimum can, however, not be chosen too large as this biases the sample towards tracks with high transverse momenta  $p_T$ .

The second quantity important for the reconstruction is the  $\chi^2$  per TPC cluster. It relates the goodness of the track fitting to the measured points used in its reconstruction. As a default,  $\chi^2/N_{TPC} \in [0.3, 4.0]$  is used (Fig. 6.10).

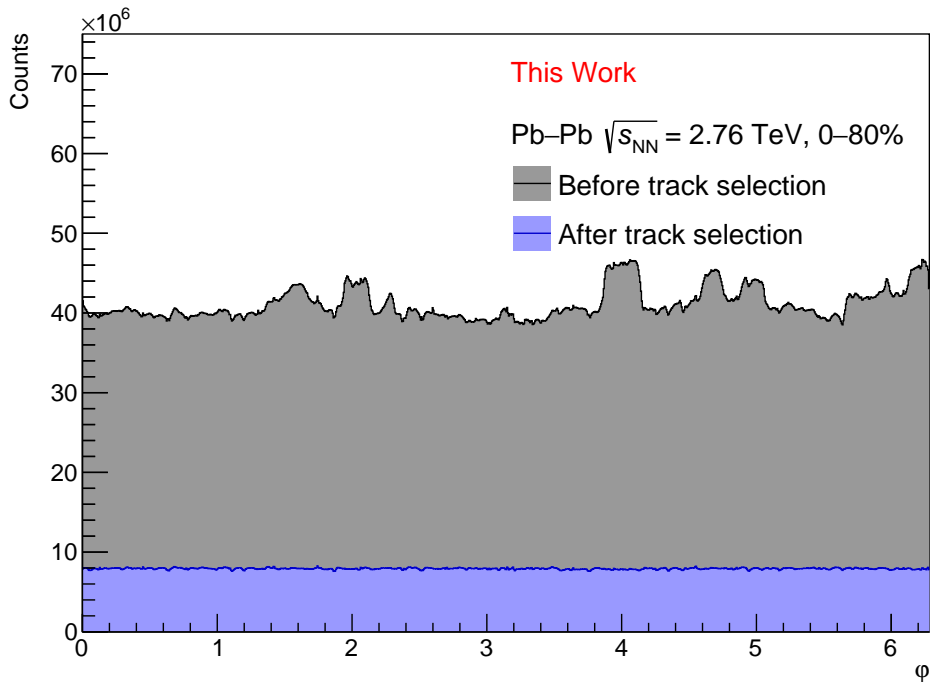


Figure 6.8: Distribution of  $\varphi$  before and after the track selection.

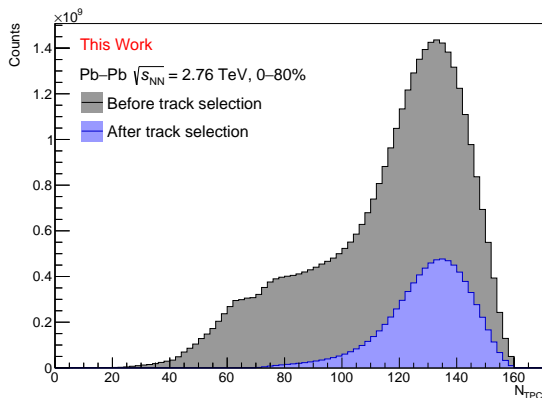


Figure 6.9: Distribution of  $N_{TPC}$  before and after the track selection.

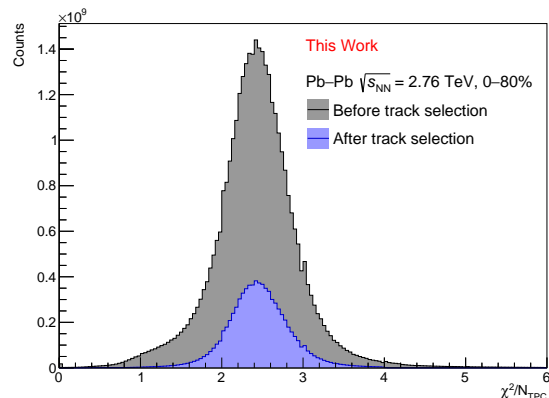


Figure 6.10: Distribution of  $\chi^2/N_{TPC}$  before and after the track selection.

## 6.2.2 Kinematic cuts

Regarding the  $p_T$  selection of tracks, the following criterion is applied  $p_T \in [0.2, 5.0]$  GeV/ $c$  (see Fig. 6.11). The lower boundary assures that the tracks can reach the TPC, as the TPC is not one of the innermost detectors within ALICE. As such, this minimum removes artefacts in the TPC reconstruction, which would lead to a bias in the analysis. The motivation for the upper boundary of 5.0 GeV/ $c$  lies in the removal of jets, which in general contain high  $p_T$  particles from the hard processes that generated the jet [38]. As jets represent a few-particle non-flow contribution, their influence has to be suppressed to not bias the flow analysis. These jets have to be removed not only due to non-flow, but also as they lead to event-by-event anisotropies which bias the measurement as well.

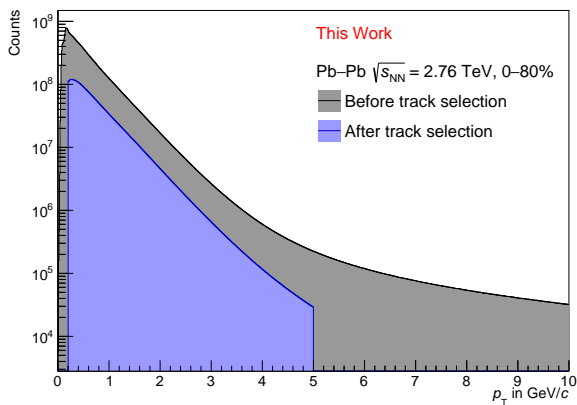


Figure 6.11: Distribution of  $p_T$  before and after the track selection.

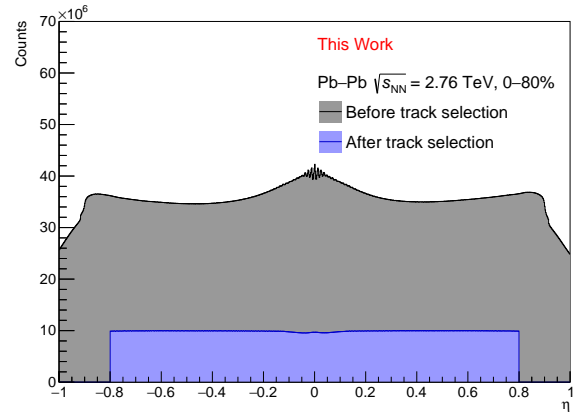


Figure 6.12: Distribution of  $\eta$  before and after the track selection.

Further, a cut along the pseudorapidity  $\eta$  is used as  $|\eta| < 0.8$  (see Fig. 6.12). This guarantees the usage of almost the full coverage of the TPC ( $|\eta| < 0.9$ ), while removing edge effects and guaranty a uniform acceptance in pseudorapidity.

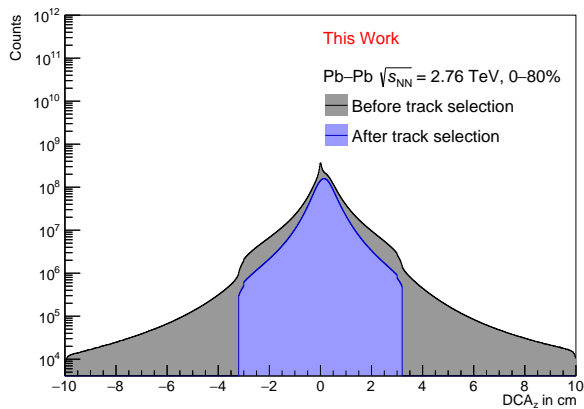


Figure 6.13: Distribution of  $DCA_z$  before and after the track selection.

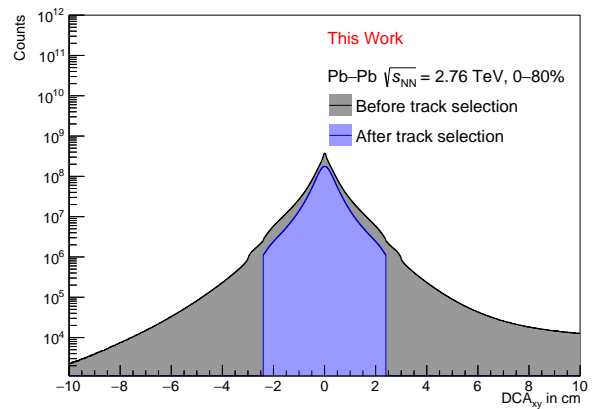


Figure 6.14: Distribution of  $DCA_{xy}$  before and after the track selection.

Lastly, cuts on the so-called distance to closest approach  $DCA$  are used along the beam axis  $z$  and in the transverse plane  $xy$ . The distance of closest approach represents the minimal distance a track has to the reconstructed primary vertex of the collision. Minimising the allowed  $DCA$  of tracks leads to the selection of mainly primary particles, as particles stemming from decays (the so-called secondaries) have in general a larger  $DCA$ . The removal of secondaries is of interest, as they are correlated to the other products of their decay and thus they represent non-flow. However, as the TPC is located rather far from the inner part of the detector, the cut on  $DCA$  cannot be chosen too narrow. As a default for this analysis, the selection criteria  $DCA_z < 3.2$  cm (Fig. 6.13) and  $DCA_{xy} < 2.4$  cm (Fig. 6.14) are chosen.

### 6.3 Weights

In addition to event and track selections, particle weights<sup>1</sup> have to be introduced to correct for non-uniform efficiency (NUE) and non-uniform acceptances of the detector.

For obtaining the NUE for each centrality bin, HIJING simulations anchored to the real LHC10h Pb–Pb data are used. This Monte Carlo generator has been tuned to produce events for Pb–Pb collisions at  $\sqrt{s_{NN}} = 2.76$  TeV. The information collected at this stage, the so-called “kinematics” level, represents the particle distributions that should be obtained for an ideal case (or with an ideal/perfect detector). These data is then be propagated through a simulation of the ALICE detector (using softwares like GEANT3 or Geant4). The distribution after this propagation through the detector is called the “reconstruction” level and it uses the same event and track selection criteria as the real analysis. By comparing the  $p_T$  distribution of particles at the kinematics and reconstruction level, one can obtain the efficiency of the detector for measuring particles with a certain transverse momentum  $p_T$ . In particular, the efficiency  $\epsilon$  is defined as the  $p_T$  distribution at reconstructed level divided by the kinematics level. An example for the centrality 10–20% is shown in Fig. 6.15. As one can see, the efficiency of reconstructed particles has a maximum for low momenta and then drops to a constant value for higher  $p_T$ , meaning that the detector is less good at reconstructing those tracks. The corresponding NUE weights are then obtained as  $1/\epsilon$  for each centrality range.

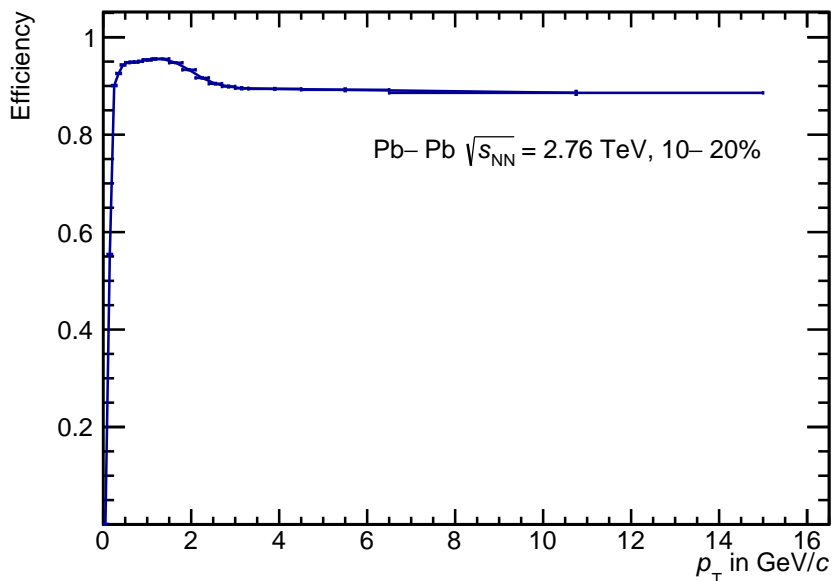


Figure 6.15: Reconstruction efficiency as a function of  $p_T$  for centrality 10-20%.

In addition to the NUE, weights for the NUA have been investigated via a data driven method for each run and centrality bin separately. In this procedure, three-dimensional histograms between the azimuthal angle  $\varphi$ , the pseudorapidity  $\eta$  and the  $PV_z$  are obtained and called the *correction maps*. Inverting this three-dimensional correction maps results in the weights. An example for the projection of the correction map of run 137161 in centrality 10–20% onto the three axis is shown in Fig. 6.16, Fig. 6.17 and Fig. 6.18. In particular, one can see that the corrections for the pseudorapidity and azimuthal angle are

<sup>1</sup>The implementation of obtaining the weights is the work of Dong Jo Kim.

flat, as it is expected for the TPC-only tracks in LHC10h. Due to this uniform acceptance of the TPC in the LHC10h data, it has been decided to not use NUA corrections for the default analysis. A systematic check with their application will be performed at a later point.

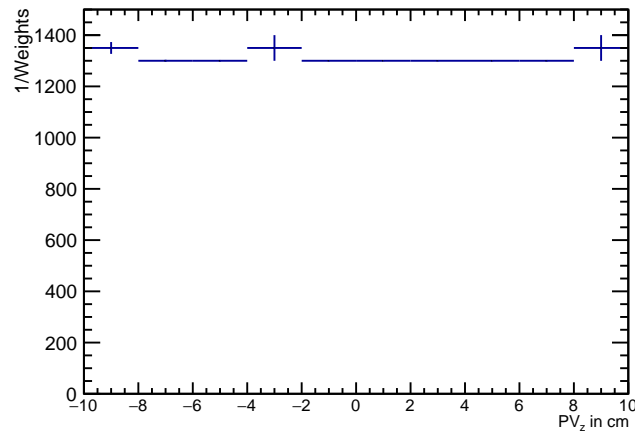


Figure 6.16: Projection of the correction map of run 137161 in centrality 10-20% onto the  $PV_z$  axis.

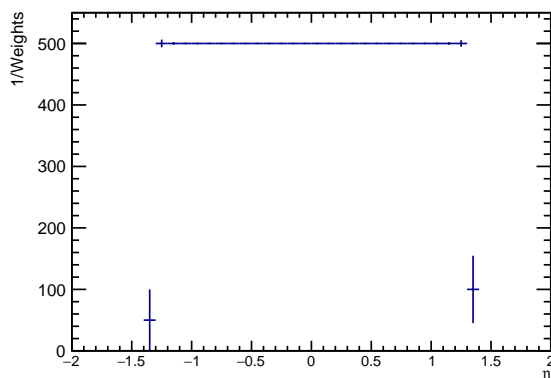


Figure 6.17: Projection of the correction map of run 137161 in centrality 10-20% onto the  $\eta$  axis.

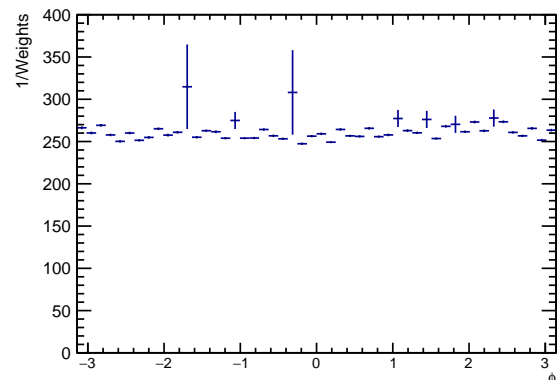


Figure 6.18: Projection of the correction map of run 137161 in centrality 10-20% onto the  $\varphi$  axis.

## 6.4 Final quality assurance

As final quality assurance, the results of the multiparticle correlators from the numerator and denominator in Eq. (5.11) are plotted for each run and centrality bin, as well as the corresponding average multiplicity of the run and its total amount of events (see Figs. E.1-E.2 in App. E.1 as an example). With this run by run trending, four runs with an extremely low number of events were found with outliers in the numerator and denominator for some of the measured SPC. Removing these low statistics runs improved the stability of the statistical errors while only losing 0.2% of the data. The details on how the statistical errors are computed can be found in Sec. 6.6.

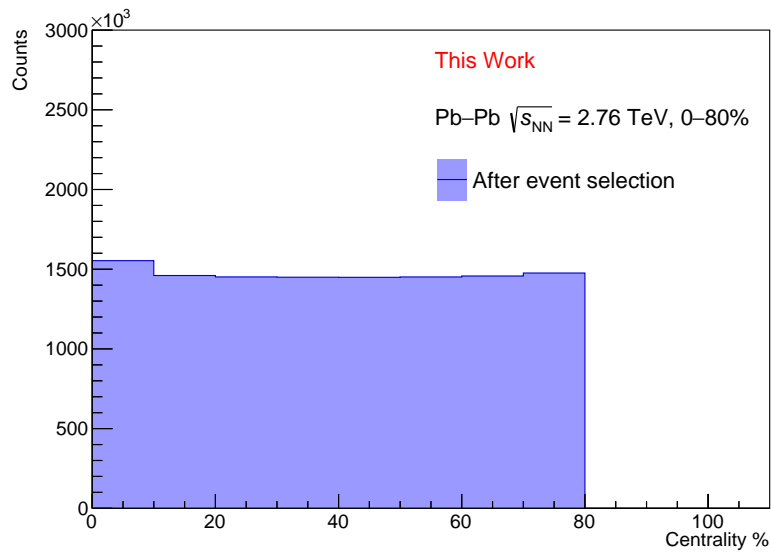


Figure 6.19: Distribution of centrality after the event selection.

Additionally, the centrality distribution of all 84 used runs has been obtained (see Fig. 6.19). As it can be seen, there is a slight excess of events in the 0-10% centrality bin. The effects of this will be studied in a future systematic check, but no huge impact is expected.

As a final quality assurance, the framework employed for this analysis is used with the above described event and track selection criteria to measure already published flow observables, in particular  $v_2\{2\}$  and  $v_2\{4\}$  and the symmetric cumulants  $SC(2,3)$  and  $SC(2,4)$ . The results for  $v_2$  in Fig. 6.20 show a good agreement with the published data [51], in particular as the analysis in [51] did not use the same centrality selection framework, and had a smaller data set as the one in the presented analysis. Similarly, the results of the symmetric cumulants provided in Fig. 6.21 are in great agreement with the published data [61] as well. Here, one has to emphasise that the analysis in [61] did not use TPC-only tracks but a combination of ITS and TPC tracks (also called *hybrid tracks*).

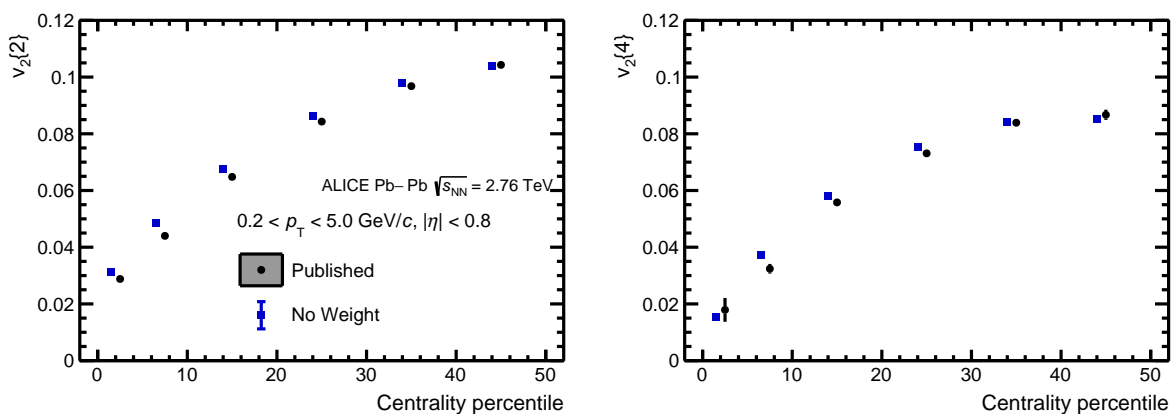


Figure 6.20: Comparison of  $v_2\{2\}$  and  $v_2\{4\}$  obtained with the code from this analysis to the published data [51].

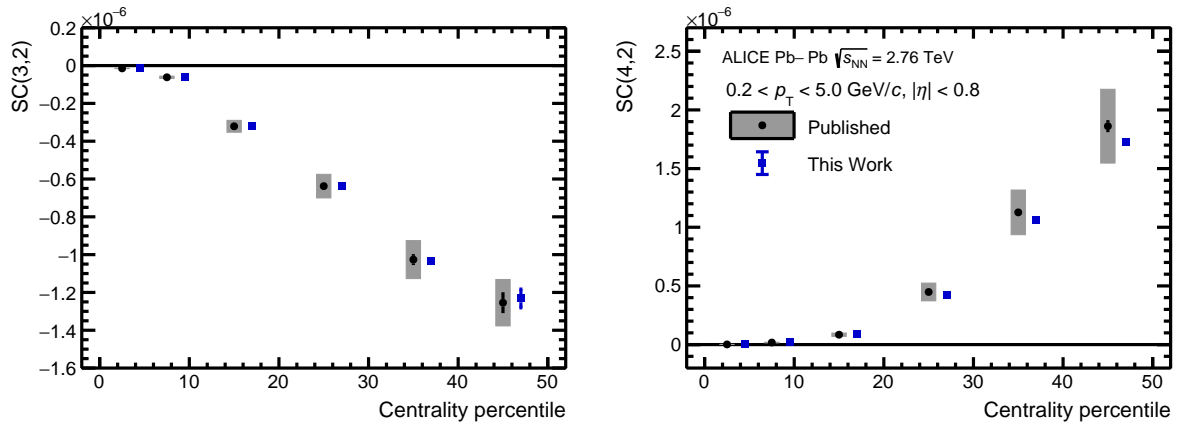


Figure 6.21: Comparison of SC(2, 3) and SC(2, 4) obtained with the code from this analysis to the published data [61].

## 6.5 Non-flow estimation

One of the most important studies in flow analyses is the impact of non-flow on the final observables. To investigate its effects in this analysis, the multiparticle correlators in the numerator and denominator of the GE are obtained using simulated data from HIJING (see Sec. 3.4) on a data set, which mimics the real data of Pb-Pb collisions at  $\sqrt{s_{NN}} = 2.76$  TeV recorded by ALICE. The obtained results are then plotted in comparison to the real experimental data. An example of this procedure for the SPC  $\langle \cos [4(\Psi_4 - \Psi_2)] \rangle$  is shown in Fig. 6.22. As it can be seen, the results of the multiparticle correlators from HIJING are compatible with zero when compared to the real data, which has a clear, non-zero signal. Thus one can conclude, that non-flow does not affect the multiparticle correlators in the numerator and denominator in the presented centrality region. This is true for the other measured SPC as well. The respective plots are provided in App. C. It has to be noted, that the GE estimator itself cannot be measured using the HIJING data, as one will face a 0/0 situation between the numerator and denominator. However, the provided study shows that the numerator and denominator themselves are not affected by non-flow in the relevant scale.

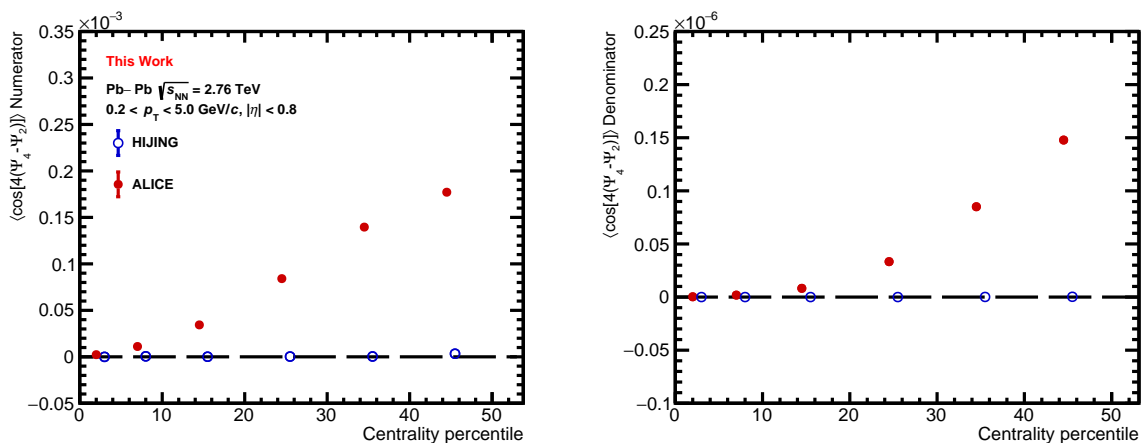


Figure 6.22: Comparison of the multiparticle correlators from the numerator and denominator in the GE of  $\langle \cos [4(\Psi_4 - \Psi_2)] \rangle$  obtained with HIJING and the real experimental data.

## 6.6 Statistical errors

The often used bootstrap method divides the measured data into  $N$  subsamples. For each subsample, the desired quantity is calculated individually. Finally, the mean of the subsamples is calculated and its standard deviation used as the error. However, this procedure is not feasible for SPC given the fact that the GE uses higher order correlators (at least a 6 particle correlator for the denominator). Such higher order correlators are statistically very demanding and as such, dividing the data into subsamples can lead to a negative denominator purely due to fluctuations and lack of statistics. This renders the bootstrap method not feasible for the measurement of SPC using the Run 1 data. As such, the alternative technique of first order error propagation has been employed [16, 100]. For this, the GE is written in the form

$$SPC = \sqrt{\frac{\pi}{4}} \frac{\langle N \rangle}{\sqrt{\langle D \rangle}}. \quad (6.3)$$

In Eq. (6.3),  $\langle N \rangle$  and  $\langle D \rangle$  are the weighted averages for the numerator and denominator obtained with the multiparticle correlators. Using first order error propagation on these quantities results into the leading order estimate of the error  $\sigma_{SPC}$  as

$$\sigma_{SPC}^2 = \left( \frac{SPC}{\langle N \rangle} \cdot s_{\langle N \rangle} \right)^2 + \left( \frac{1}{2} \frac{SPC}{\langle D \rangle} \cdot s_{\langle D \rangle} \right)^2 - \frac{1}{2} \frac{SPC^2}{\langle N \rangle \langle D \rangle} Cov(\langle N \rangle \langle D \rangle), \quad (6.4)$$

where  $s_{\langle N \rangle}$  and  $s_{\langle D \rangle}$  are the unbiased estimates for the square-root of the sample variance on the numerator and denominator, respectively. The term  $Cov(\langle N \rangle \langle D \rangle)$  describes the estimate for the sample covariance between numerator and denominator. See App. D for the definition of the unbiased estimate of an error.

Regarding the estimate of the covariance, the classical approach is

$$Cov(\langle N \rangle \langle D \rangle) \propto \frac{\frac{\sum_{i=1}^{N_{ev}} (\omega_N)_i (\omega_D)_i N_i D_i}{\sum_{i=1}^{N_{ev}} (\omega_N)_i (\omega_D)_i} - \frac{\sum_{i=1}^{N_{ev}} (\omega_N)_i N_i}{\sum_{i=1}^{N_{ev}} (\omega_N)_i} \frac{\sum_{j=1}^N (\omega_D)_j D_j}{\sum_{j=1}^{N_{ev}} (\omega_D)_j}}{1 - \frac{\sum_{i=1}^{N_{ev}} (\omega_N)_i (\omega_D)_i}{\sum_{i=1}^{N_{ev}} (\omega_N)_i \sum_{j=1}^{N_{ev}} (\omega_D)_j}} \quad (6.5)$$

where  $N_i$  and  $D_i$  are the measured values of numerator and denominator per event with their corresponding event weights  $(\omega_N)_i$  and  $(\omega_D)_i$ . In this regard, an alternative approach for estimating the covariance term has been studied, which estimates the joined mean of numerator and denominator not as their respective product, but as a *single* multiparticle correlator  $J$ , i.e.

$$Cov(\langle N \rangle \langle D \rangle) \propto \frac{\frac{\sum_{i=1}^{N_{ev}} (\omega_J)_i J_i}{\sum_{i=1}^{N_{ev}} (\omega_J)_i} - \frac{\sum_{i=1}^{N_{ev}} (\omega_N)_i N_i}{\sum_{i=1}^{N_{ev}} (\omega_N)_i} \frac{\sum_{j=1}^N (\omega_D)_j D_j}{\sum_{j=1}^{N_{ev}} (\omega_D)_j}}{1 - \frac{\sum_{i=1}^{N_{ev}} (\omega_N)_i (\omega_D)_i}{\sum_{i=1}^{N_{ev}} (\omega_N)_i \sum_{j=1}^{N_{ev}} (\omega_D)_j}} \quad (6.6)$$

This multiparticle correlator  $J$  has the same output in terms of flow amplitudes and symmetry planes as the product of numerator and denominator. This is motivated by fact that the same event product of two multiparticle correlators is not the same after averaging as if one uses a joined multiparticle correlator, even if the output in terms of flow amplitudes and symmetry planes is the same. This differences originates from the fact that the product of two lower order multiparticle correlators does not remove all autocorrelations as the joined one does (see [29] for more details). To study the impact

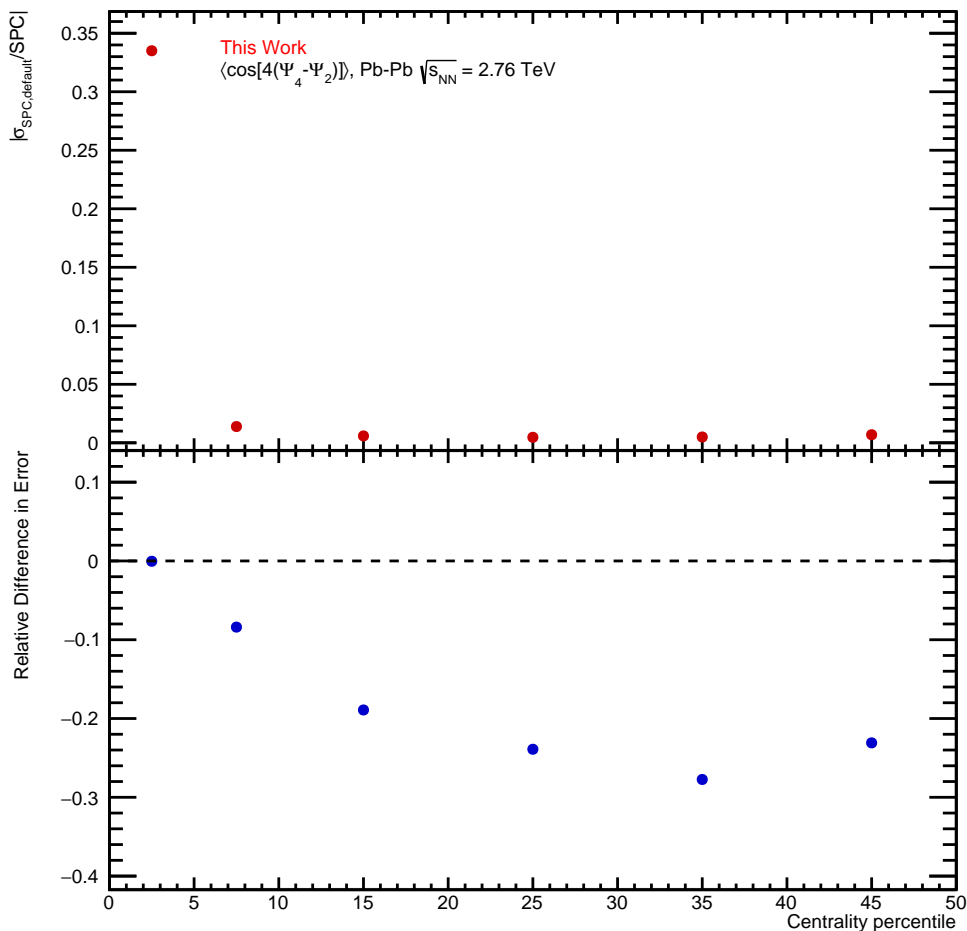


Figure 6.23: Error of the classical approach relative to the signal as an absolute value (upper panel) and relative difference in error between the classical and alternative approaches (bottom panel).

of this alternative approach, the relative difference between the two errors are calculated as

$$\text{Relative Difference in Error} = \frac{\sigma_{\text{classical}} - \sigma_{\text{alternative}}}{\sigma_{\text{classical}}}, \quad (6.7)$$

where  $\sigma_{\text{classical}}$  and  $\sigma_{\text{alternative}}$  are the errors of the classical and alternative approaches, respectively. The difference between the two approaches is found to be around 5–10% for most SPC combinations (see App. E.2). The biggest difference is found for the SPC between  $\Psi_2$  and  $\Psi_4$  with a value about 30 % (see Fig. 6.23). However, this huge difference is in a region where the statistical error is two orders of magnitude smaller compared to the actual SPC signal.

In addition, the alternative approach limits the amount of feasible SPC drastically. If the numerator is a multiparticle correlator of order  $k$ , the denominator subsequently is of order  $2k$  and thus the correlator  $J$  will be of order  $3k$ . This implies, that only combinations of SPC using at most a 4-particle correlator in the numerator can be used in this approach. From this limitation and the extremely small size of the statistical errors of both approaches, it has been decided to continue the usage of the classical approach.

## 6.7 Systematic checks

To evaluate the systematic errors of this analysis the so-called Barlow test is employed [101, 102]. In this procedure, one of the default values in the event or track selection is changed and the analysis is performed with this variation. As such, the results related to this single change of a parameter are referred to as the *trial* (denoted by  $SPC_{trial}$ ). To study whether the divergence between the trial and the default results  $SPC_{def}$  is of significance, their difference is calculated as a first step. It is defined as

$$Diff = SPC_{trial} - SPC_{def}. \quad (6.8)$$

To determine its statistical significance, the error of the trial  $\sigma_{trial}$  in comparison to the one of the default analysis  $\sigma_{def}$  has to be accounted for. The importance of this lies in the statistical influence of the used trials. In general, when a selection cut is tightened, less data is used for the analysis leading to an increased statistical error for the trial, while a looser cut leads to the opposite effect in general. To account for this, the so-called *error on the difference* is used

$$Err = \sqrt{|\sigma_{trial}^2 - \sigma_{def}^2|}. \quad (6.9)$$

In the last equation, the minus sign has to be used because the data sets used for the trial and default are correlated to each other as they only differ in one selection criterion while being part of the larger, default data set. Would the two data sets be uncorrelated to each other, a plus sign would have to be used in Eq. (6.9). Given the difference and the error in difference, the so-called  $\sigma_{Barlow}$  can be computed as

$$\sigma_{Barlow} = \frac{Diff}{Err}. \quad (6.10)$$

The  $\sigma_{Barlow}$  quantifies the statistical significance of the performed trial. If it is found to be greater than a certain value, the trial is classified as a statistically relevant deviation. For this analysis of symmetry plane correlations, a critical value of  $\sigma_{Barlow} = 1$  is used i.e. every trial with  $\sigma_{Barlow} > 1$  is counted as statistically important.

As a last step, the systematic error has to be assigned. For this, the so-called *relative variation* is computed as

$$Rel.Var. = \frac{Diff}{SPC_{def}} \quad (6.11)$$

The overall relative variation of all trials is then obtained as the square root of the individual relative variations added in quadrature. To obtain the final systematic error of this trial, the relative variation has to be multiplied by the absolute value of the SPC from the default analysis.

This procedure of the Barlow test is in general applied to each data point individually. As such, the overall significance of the trial is evaluated by fitting all  $\sigma_{Barlow}$  in the centrality range of interest with a polynomial of zeroth order. If this fit returns a  $\sigma_{Barlow, fitted}$  greater than one, the relative variation is assigned. The latter is also obtained as a fit with a polynomial of zeroth order of all the individual relative variations in the same centrality range.

However, the latter strategy leads to a negligible amount of statistically significant trials, and as such another approach is finally used to obtain the systematic uncertainties. For this, the default and the trial results of SPC are rebinned separately of each other in the centrality range of interest consisting of  $N_c$  data points according to [100] as

$$SPC_{rebinned} = \frac{\sum_{i=1}^{N_c} SPC_i / \sigma_i^2}{\sum_{i=1}^{N_c} 1 / \sigma_i^2} \quad (6.12)$$

In the above equation,  $SPC_i$  are the single data points that get binned together and  $\sigma_i^2$  are their corresponding statistical error squared. The error of the rebinned  $SPC$  is obtained as

$$\sigma_{rebinned} = \sqrt{\frac{1}{N_c} \cdot \frac{1}{\sum_{i=1}^{N_c} 1/\sigma_i^2}}. \quad (6.13)$$

With the rebinned values of the default and trial, the Barlow test is then performed leading directly to one single value of  $\sigma_{Barlow}$  and the relative variation. As the obtained  $\sigma_{Barlow}$  with this method are in general very large, the critical value has been adapted to  $\sigma_{Barlow} > 2$ .

Overall, twelve systematic trials have been performed. The first part of these trials concerns the centrality and event selection. To study the effect of the centrality estimation, a trial using the V0M instead of the SPD clusters has been used. Additionally, the primary vertex in  $z$  direction has been narrowed to 8 cm and 6 cm. From these last two trials, only the largest significant check is assigned to the systematic error. Concerning the track selection, two trials for the  $DCA$  have been used, namely  $DCA_{xy} < 1$  cm and  $DCA_z < 2$  cm. The track quality is checked by varying the boundaries of the  $\chi^2/N_{TPC}$  to  $0.3 < \chi^2/N_{TPC} < 4.0$  and  $0.1 < \chi^2/N_{TPC} < 3.5$ . Three systematic trials concerning the number of TPC clusters have been performed, in particular  $N_{TPC} > 80$ ,  $N_{TPC} > 90$  and  $N_{TPC} > 100$ . From these three  $N_{TPC}$  trials, again only the largest, statically relevant trial is assigned. Lastly, the magnetic field configuration of the L3 solenoid magnet is used as a systematic trial. For this, the runs are divided into two groups with magnetic field polarity “++” and “--”. From these two trials, again only the largest relevant check is assigned.

As an example, the systematic trials of  $\langle \cos [4(\Psi_4 - \Psi_2)] \rangle$  are shown in Fig. 6.24. There, the integrated SPC between 0—50 % for the default and trial values are shown, as well as the corresponding  $\sigma_{Barlow}$  and the absolute value of relative variation for each trial. The exact values of relative variations for all SPC and the corresponding figures can be found in App. E.3.

Table 6.3 summarizes the considered ranges of centrality for each SPC combination as well as the total relative variation that was found.

Table 6.3: Summary of all measured SPC with their relevant centrality range and the total relative variation.

SPC	Centrality range	Total relative variation
$\langle \cos [4(\Psi_4 - \Psi_2)] \rangle$	0–50%	0.111
$\langle \cos [6(\Psi_2 - \Psi_3)] \rangle$	0–50%	1.373
$\langle \cos [6(\Psi_6 - \Psi_2)] \rangle$	0–50%	0.252
$\langle \cos [6(\Psi_6 - \Psi_3)] \rangle$	0–50%	0.093
$\langle \cos [2\Psi_2 + 3\Psi_3 - 5\Psi_5] \rangle$	0–50%	0.075
$\langle \cos [8\Psi_2 - 3\Psi_3 - 5\Psi_5] \rangle$	10–50%	1.341
$\langle \cos [2\Psi_2 - 6\Psi_3 + 4\Psi_4] \rangle$	0–50%	0.202
$\langle \cos [2\Psi_2 + 4\Psi_4 - 6\Psi_6] \rangle$	0–50%	0.102
$\langle \cos [2\Psi_2 - 3\Psi_3 - 4\Psi_4 + 5\Psi_5] \rangle$	5–50%	0.133

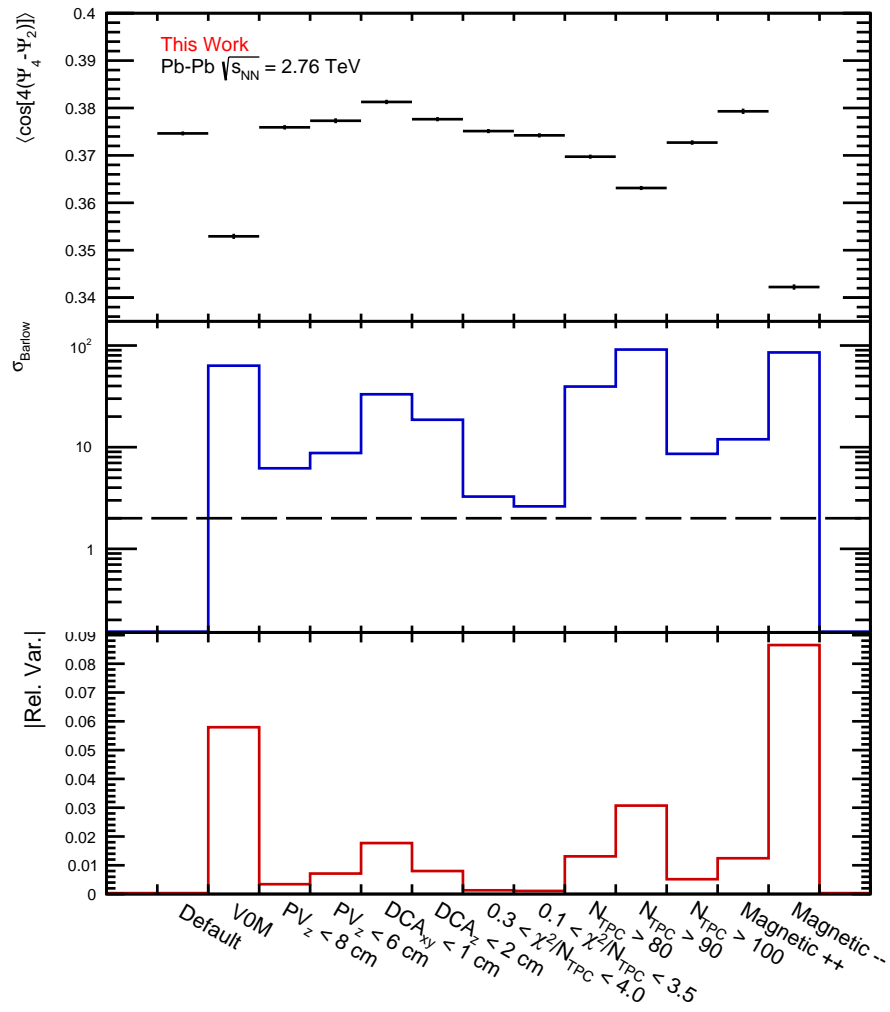


Figure 6.24: Results for  $\sigma_{Barlow}$  and the relative variation (both in absolute values) of the systematic trials for  $\langle \cos[4(\Psi_4 - \Psi_2)] \rangle$ .

# Chapter 7

## Experimental results and discussion

In this chapter, the experimental results for SPC obtained with ALICE using the GE are presented. First, the data for the SPC observable  $\langle \cos [4(\Psi_4 - \Psi_2)] \rangle$  is presented in Fig. 7.1 with a comparison to the ATLAS results [67], estimated with the SP method. The comparison of the other SPC measurements of this work to the ATLAS results can be found in App. F.1. From the results in Fig. 7.1, it can be seen that the two experimental approaches lead to a different magnitude of the final state SPC, especially for larger centralities. Focussing on the ALICE data with the GE, one can see that the signal of

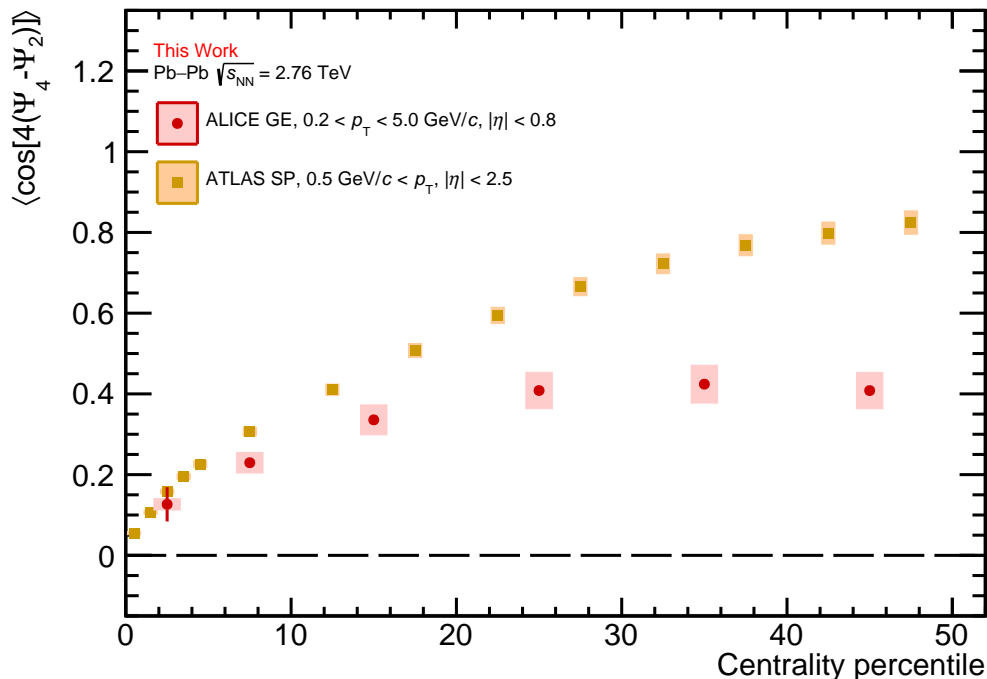


Figure 7.1: Comparison of the measured ALICE data of  $\langle \cos [4(\Psi_4 - \Psi_2)] \rangle$  as function of centrality using the GE to the ATLAS results [67] using the SP method.

SPC goes towards zero when approaching a centrality of 0%. This result indicates that the two symmetry planes  $\Psi_2$  and  $\Psi_4$  are uncorrelated to each other for these ultra-central collisions. This is expected, as in this regime no anisotropy in the initial state is present. Any participant planes, and later symmetry planes, stem from random fluctuations and are thus expected to be uncorrelated. Further, one expects that the signal of SPC goes to zero again when approaching ultra-peripheral collisions. In this regime, the initial

anisotropy cannot be translated into the final state as the system size is extremely small and the evolution time very short. Thus, the final state is mainly dominated by fluctuations for such ultra-peripheral collisions, leading again to a SPC signal compatible with zero. However, in the regime of central to mid-central collisions, one can see a non-zero signal below unity. The latter observation indicates that  $\Psi_2$  and  $\Psi_4$  are two distinct planes (otherwise the SPC would yield one), while the non-zero signal shows that the two symmetry planes are on average correlated to each other.

To further understand the origin of this correlation, the ALICE data are compared to model predictions<sup>1</sup>. For the initial state, the GE is provided by the T<sub>R</sub>ENTo model in two distinct ways. First, the participant plane correlations are obtained via the eccentricities  $\mathcal{E}_n$ , and second by the energy density cumulants  $C_n$ , which were both presented in Sec. 2.1.1. For the final state, the hydrodynamic evolution is given by VISH2+1 and the evolution in the hadronic phase by UrQMD (see Sec. 3.3).

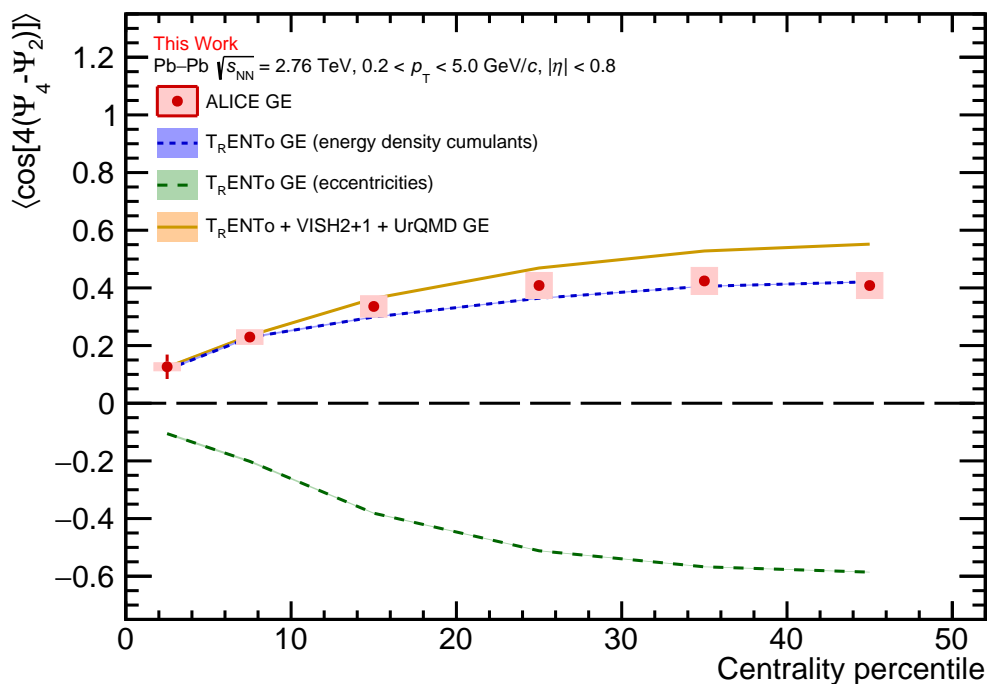


Figure 7.2: Comparison of the T<sub>R</sub>ENTo and iEBE-VISHNU models to the measured ALICE data of  $\langle \cos [4 (\Psi_4 - \Psi_2)] \rangle$ .

The first comparison of these model predictions to the experimental data is presented for the SPC  $\langle \cos [4 (\Psi_4 - \Psi_2)] \rangle$  in Fig. 7.2. As one can see, the signal of the eccentricities is of opposite sign when compared to the results of the energy density cumulants and the final state. As it was pointed out in [103], the participant planes defined via eccentricities point in the direction of the strongest pressure gradient and are thus the minor axis of the associated anisotropic shape. In contrast to that, the symmetry planes point in the direction of the largest flow and represent therefore a major axis. If no additional interferences are present, the participant plane and its corresponding symmetry plane point in the same direction. The study conducted in [104] investigated correlations between two

<sup>1</sup>The model data for the SPC is courtesy of Seyed Farid Taghavi.

participant planes in the initial state and “for a matter of convenience” shifted the minor axis participant planes  $\Phi_n$  to major axis  $\Phi_n^*$  via the transformation

$$\Phi_n^* = \Phi_n + \frac{\pi}{n}. \quad (7.1)$$

Therefore, the participant plane correlation with a numerical prefactor  $a$  is transformed as

$$a(\Phi_n^* - \Phi_m^*) = a(\Phi_n - \Phi_m) + a\left(\frac{\pi}{n} - \frac{\pi}{m}\right), \quad (7.2)$$

which introduces a phase  $\delta_{n,m} = a\pi(1/n - 1/m)$  that inverts the sign of the signal for some participant plane correlations. In particular, if  $\delta_{n,m} \bmod 2\pi = |\pi|$ , the sign of the participant plane correlation is inverted while  $\delta_{n,m} \bmod 2\pi = 0$  results in no change. Generalizing this approach presented in [104], one can express the correlation between  $k$  participant planes  $a_1\Phi_{n_1} + \dots + a_k\Phi_{n_k}$  in their major axis as

$$a_1\Phi_{n_1}^* + \dots + a_k\Phi_{n_k}^* = a_1\Phi_{n_1} + \dots + a_k\Phi_{n_k} + \pi\left(\frac{a_1}{n_1} + \dots + \frac{a_k}{n_k}\right). \quad (7.3)$$

Again, the last term in the above equation presents the phase shift  $\delta$  for the transformation of  $k$  participant planes from minor to major axis. It has to be stressed again that if  $\delta \bmod 2\pi = |\pi|$ , the sign of the participant plane correlation is inverted, while  $\delta \bmod 2\pi = 0$  does not change it. In particular, for the initial participant plane correlation  $\langle \cos [4(\Phi_4 - \Phi_2)] \rangle$ , one obtains  $\delta = \pi(4/4 - 4/2) = -\pi$ . Therefore, the transformation of the participant planes from minor to major axis introduces a sign change for this particular combination. In general, a similar transformation from minor axis participant planes to major axis symmetry planes is a possible reason for the sign change that one can observe in Fig. 7.2 from the initial state via eccentricities to the final state. Why this change of sign is not present in the description of the initial state via the energy density cumulants has to be investigated further.

Focussing on the results obtained with the energy density cumulants and the final state, one can study this signal further by employing the linear and non-linear response formalism presented in Sec. 2.1.3:

$$\begin{aligned} v_2^2 v_4 e^{i4(\Psi_4 - \Psi_2)} &= V_4 (V_2^2)^* \\ &= (\omega_4 C_4 + \omega_{422} C_2^2) \cdot \omega_2^2 (C_2^2)^* \\ &= \omega_2 \omega_4 c_2^2 c_4 e^{i4(\phi_4 - \phi_2)} + \omega_{422} \omega_2^2 c_2^2. \end{aligned} \quad (7.4)$$

As one can see from the above equation, the phase of the final state corresponds to the measured symmetry plane correlations. In the absence of non-linear response between the second and fourth order, i.e.  $\omega_{422} = 0$ , this final state SPC would be equal to the initial state participant plane correlation, while a difference can be obtained by having a non-zero non-linear coupling constant. Using this, one can see in Fig. 7.2 that the predictions for the initial state participant plane correlations via the energy density cumulants and for the final state are equal to each other for the centrality range 0–10%. With rising centrality, the difference between these predictions becomes larger, indicating an increasing non-linear response. In particular, the T<sub>R</sub>ENTo + iEBE-VISHNU model describes the measured data very well only in the regime of linear response while the predictions deviate increasingly stronger with increasing centrality and non-linear response.

As a second SPC between two planes, the correlation  $\langle \cos [6(\Psi_2 - \Psi_3)] \rangle$  is presented in Fig. 7.3. It can be observed that the measured data is compatible with zero over

the whole centrality range 0–50%, indicating that the symmetry planes  $\Psi_2$  and  $\Psi_3$  are uncorrelated. This absence of correlation between the two planes is well predicted in the final state by the employed model. This is, however, a non-trivial result. Considering the

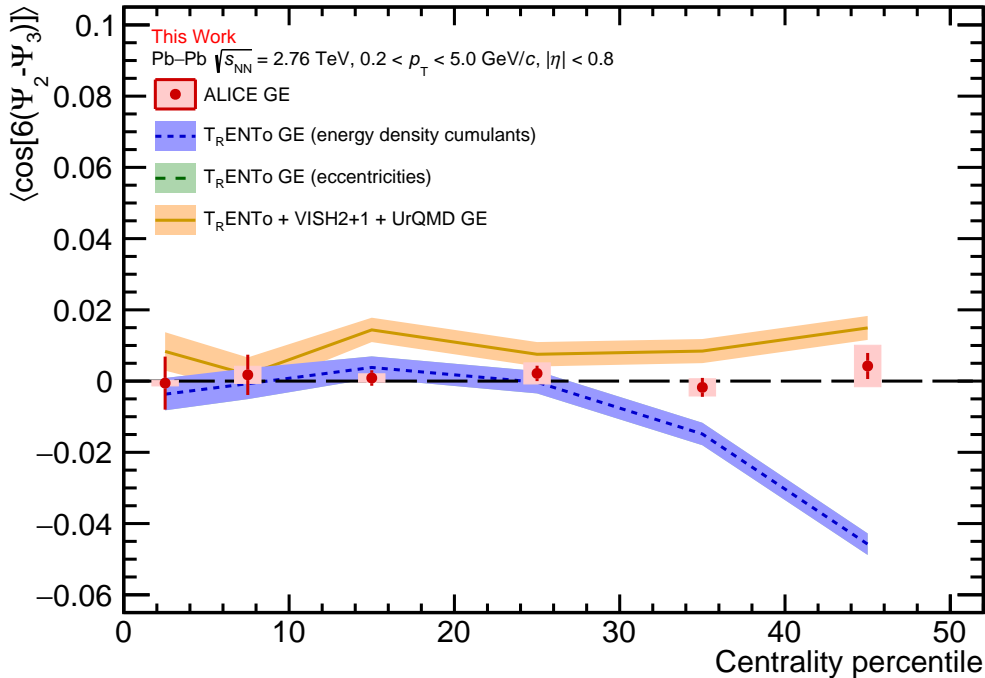


Figure 7.3: Comparison of the T<sub>R</sub>ENTo and iEBE-VISHNU models to the measured ALICE data of  $\langle \cos [6(\Psi_2 - \Psi_3)] \rangle$ .

linear and non-linear response formalism, there is no non-linear phase between the second and third harmonic, i.e.

$$\begin{aligned}
 v_2^3 v_3^2 e^{i6(\Psi_3 - \Psi_2)} &= V_3^2 (V_2^3)^* \\
 &= \omega_3^2 C_3^2 \omega_2^3 (C_2^3)^* \\
 &= \omega_2^3 \omega_3^2 c_2^3 c_3^2 e^{i6(\phi_3 - \phi_2)}.
 \end{aligned}
 \tag{7.5}$$

Thus, one would expect a direct translation of the initial state signal into the final state via this linear response. While T<sub>R</sub>ENTo first predicts participant plane correlations compatible with zero, a non-zero signal in the initial state is predicted for centralities bigger than 30%. Yet, in this regime the measured SPC signal is zero, indicated that during the hydrodynamic evolution of the system the planes get uncorrelated. This is particularly interesting, as the correlation between  $v_2$  and  $v_3$  measured via the symmetric cumulant SC(2,3) is non-zero for larger centralities [61]. This would indicate that the amplitudes themselves are correlated for larger centralities while the phases, i.e. the symmetry planes, are uncorrelated.

The last two SPC between two planes are  $\langle \cos [6(\Psi_6 - \Psi_2)] \rangle$  and  $\langle \cos [6(\Psi_6 - \Psi_3)] \rangle$  presented in Fig. 7.4 and Fig. 7.5, respectively. These results show a great difference between the model predictions and the measured data. This is, to a certain extent, not surprising as the sixth order asymmetry has multiple non-linear phases with various contributions from the second, third and fourth order initial state.

In addition to the four measured SPC between two planes, additional correlations between three symmetry planes have been extracted. The first presented SPC of this

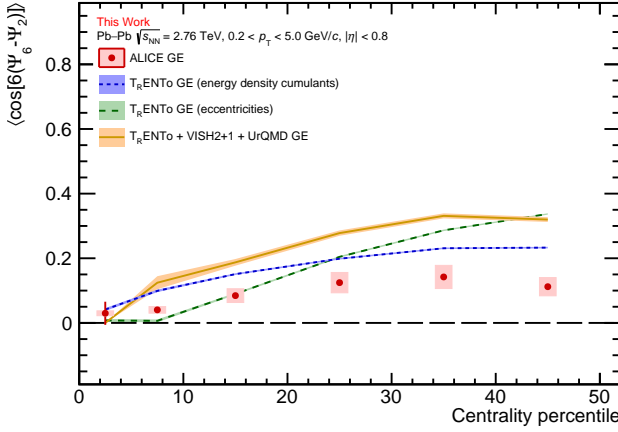


Figure 7.4: Comparison of the  $T_{\text{R}}\text{ENTo}$  and iEBE-VISHNU models to the measured ALICE data of  $\langle \cos [6 (\Psi_6 - \Psi_2)] \rangle$ .

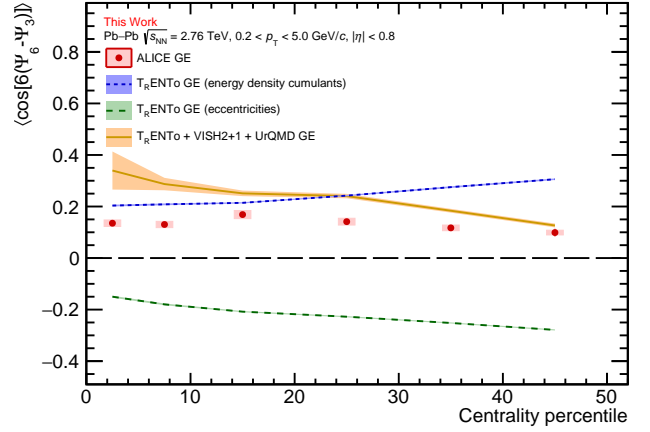


Figure 7.5: Comparison of the  $T_{\text{R}}\text{ENTo}$  and iEBE-VISHNU models to the measured ALICE data of  $\langle \cos [6 (\Psi_6 - \Psi_3)] \rangle$ .

kind is  $\langle \cos [2\Psi_2 + 3\Psi_3 - 5\Psi_5] \rangle$  shown in Fig. 7.6. Concerning the phases in the linear and non-linear response, one obtains

$$\begin{aligned} V_2 V_3 V_5^* &= v_2 v_3 v_5 e^{i(2\Psi_2 + 3\Psi_3 - 5\Psi_5)} \\ &= \omega_2 C_2 \omega_3 C_3 \cdot (\omega_5 C_5^* + \omega_{523} C_2^* C_3^*) \\ &= \omega_2 \omega_3 \omega_5 c_2 c_3 c_5 e^{i(2\phi_2 + 3\phi_3 - 5\phi_5)} + \omega_{523} \omega_2 \omega_3 c_2^2 c_3^2 \end{aligned} \quad (7.6)$$

Again a non-zero non-linear coupling constant  $\omega_{523} \neq 0$  modifies the phase between the initial and final state, leading to a difference between the participant plane and symmetry plane correlations. As one can see in Fig. 7.6, the initial and final state model predictions lie very close to each other, indicating only a weak non-linear term. In particular, the final state predictions describe the measured data extremely well. Additionally, these three particular symmetry planes have been studied further by arranging them in a different way in the SPC. The resulting combination  $\langle \cos [8\Psi_2 - 3\Psi_3 - 5\Psi_5] \rangle$  is presented in Fig. 7.7 for the centrality range 10–50 % (the lower centrality bins have been excluded due to unstable statistical errors). It has to be noted that the final state predictions for this combination could not yet be obtained but are currently under preparation. The obtained data show a signal compatible with zero, in particular when compared with the previously presented result of  $\langle \cos [2\Psi_2 + 3\Psi_3 - 5\Psi_5] \rangle$ , which was non-vanishing in the same centrality range. For the linear and non-linear response of  $\langle \cos [8\Psi_2 - 3\Psi_3 - 5\Psi_5] \rangle$  one obtains

$$\begin{aligned} V_2^4 V_3^* V_5^* &= v_2^4 v_3 v_5 e^{i(8\Psi_2 - 3\Psi_3 - 5\Psi_5)} \\ &= \omega_2^4 C_2^4 \omega_3 C_3^* \cdot (\omega_5 C_5^* + \omega_{523} C_2^* C_3^*) \\ &= \omega_2 \omega_3 \omega_5 c_2 c_3 c_5 e^{i(8\phi_2 - 3\phi_3 - 5\phi_5)} + \omega_{523} \omega_2 \omega_3 c_2^2 c_3^2 e^{i6(\phi_2 - \phi_3)}. \end{aligned} \quad (7.7)$$

The latter equation in particular shows that the non-linear part is not only governed by the hydrodynamic coupling constant  $\omega_{523}$ , but also that it has a contribution from the initial state participant plane correlation  $e^{i6(\phi_2 - \phi_3)}$ . Similar to  $\langle \cos [6 (\Psi_2 - \Psi_3)] \rangle$ , a slight correlation in the initial state can be observed for  $\langle \cos [8\Psi_2 - 3\Psi_3 - 5\Psi_5] \rangle$ , which is then lost during the hydrodynamic evolution. More investigations how the symmetry planes get uncorrelated during the hydrodynamic evolution will be addressed in further studies.

Next, the results obtained for the SPC  $\langle \cos [2\Psi_2 - 6\Psi_3 + 4\Psi_4] \rangle$  are presented in Fig. 7.8. For this combination, it can be seen that a negative signal is observed and is qualitatively

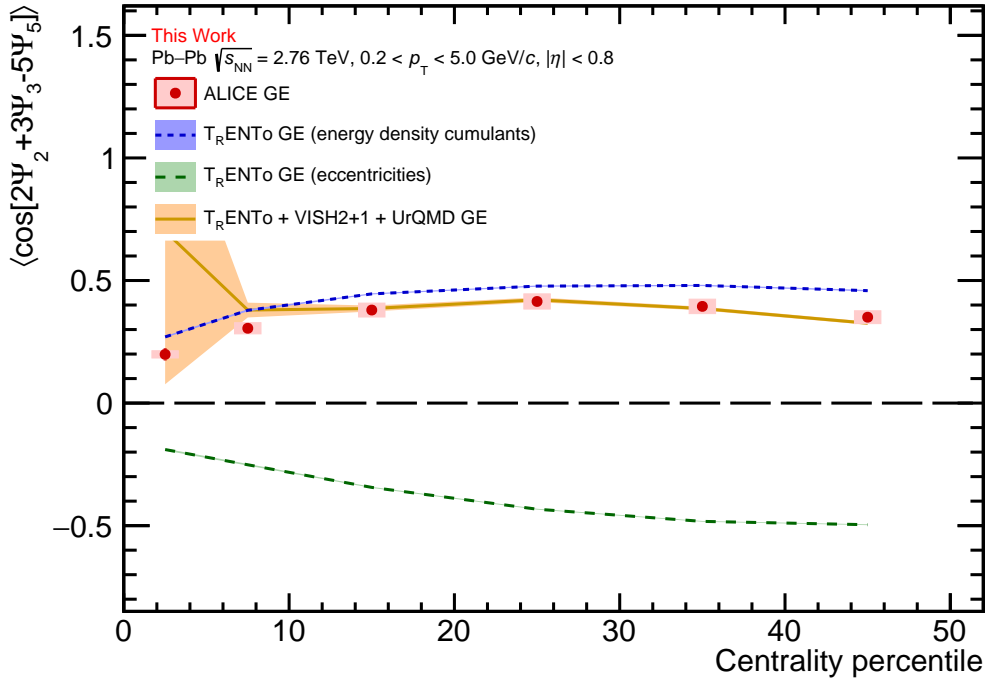


Figure 7.6: Comparison of the  $T_{\text{R}}\text{ENTo}$  and iEBE-VISHNU models to the measured ALICE data of  $\langle \cos[2\Psi_2 + 3\Psi_3 - 5\Psi_5] \rangle$ .

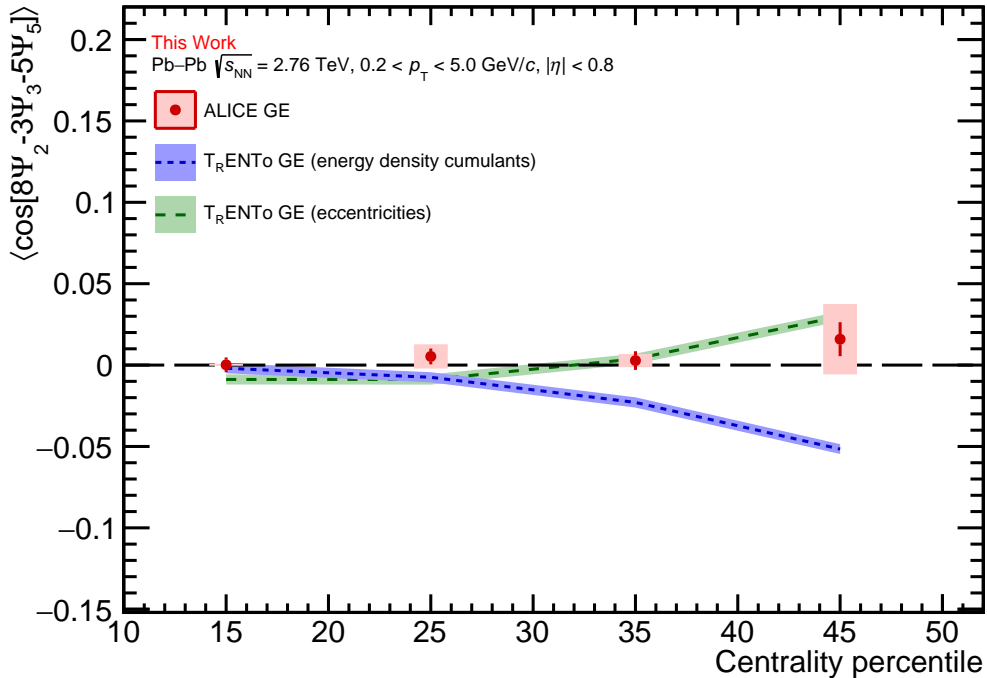


Figure 7.7: Comparison of the  $T_{\text{R}}\text{ENTo}$  and iEBE-VISHNU models to the measured ALICE data of  $\langle \cos[8\Psi_2 - 3\Psi_3 - 5\Psi_5] \rangle$ . The final state predictions for this SPC are in preparation.

very well described by the model predictions. This result is particularly interesting, as  $\Psi_3$  does not have any direct connection to  $\Psi_2$  and  $\Psi_4$  in the non-linear response model.

Thus, one would naïvely expect that  $\Psi_3$  fluctuates completely independent from the other two planes, in particular as  $\langle \cos [6(\Psi_2 - \Psi_3)] \rangle$  has been observed to be zero in the same centrality range. This independent fluctuation of  $\Psi_3$  would lead to a zero result for this SPC. However, the non-zero and negative signal indicates a correlation and thus more complex hydrodynamics beyond the leading order picture of the linear and non-linear response model.

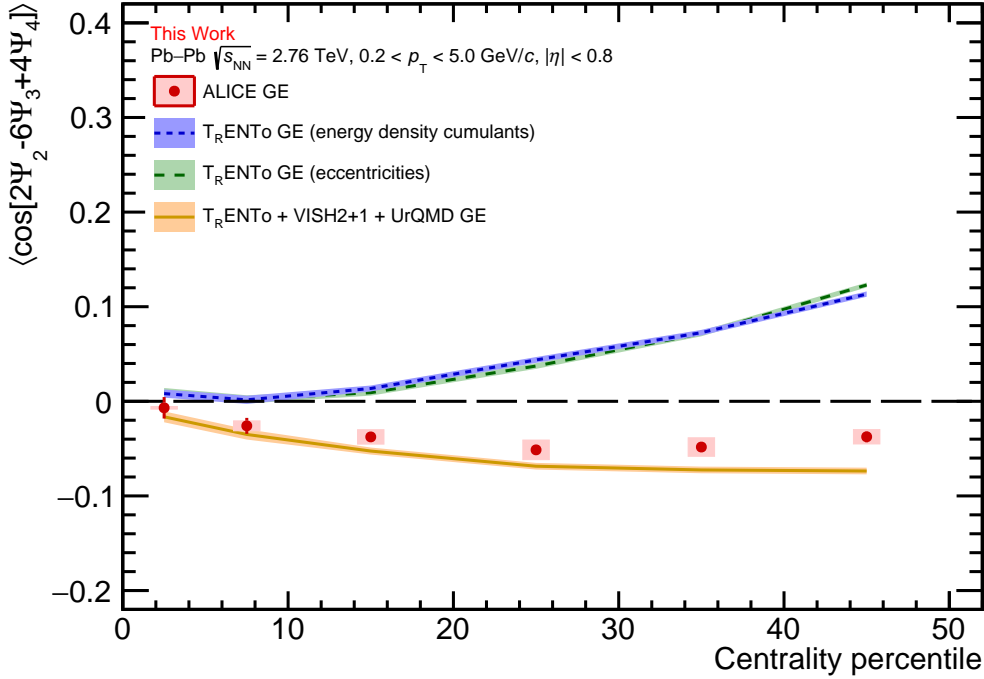


Figure 7.8: Comparison of the  $T_{R}ENTo$  and iEBE-VISHNU models to the measured ALICE data of  $\langle \cos [2\Psi_2 - 6\Psi_3 + 4\Psi_4] \rangle$ .

As a last SPC between three planes, the observable  $\langle \cos [2\Psi_2 + 4\Psi_4 - 6\Psi_6] \rangle$  is presented (Fig. 7.9). The presented results show a big discrepancy between the model predictions and the experimental data. This is not surprising, given the observation that the model fails to reproduce the SPC between two planes that involve  $\Psi_6$  as well (i.e.  $\langle \cos [6(\Psi_6 - \Psi_2)] \rangle$  and  $\langle \cos [6(\Psi_6 - \Psi_3)] \rangle$ ). These results in particular show that more detailed studies with these higher order planes are needed, and especially that the results presented here can be used as valuable input for future Bayesian analyses to constrain model parameters.

The last measured observable is the SPC between four planes, namely the combination  $\langle \cos [2\Psi_2 - 3\Psi_3 - 4\Psi_4 + 5\Psi_5] \rangle$  (see Fig. 7.10). Within the errors, the measured data show a clear non-zero signal presenting the first extraction of a SPC between four planes. The final state predictions of the model describe the data at least qualitatively. However, again due to the involvement of multiple non-linear phases, a quantitative description of the data is not achieved.

Overall, the presented results show that more studies of non-linear response are needed, as the models fail to describe the data in this regime. Additionally, the data provided here offers the opportunity to tune higher harmonics up to the sixth order, which are not reproduced by the models.

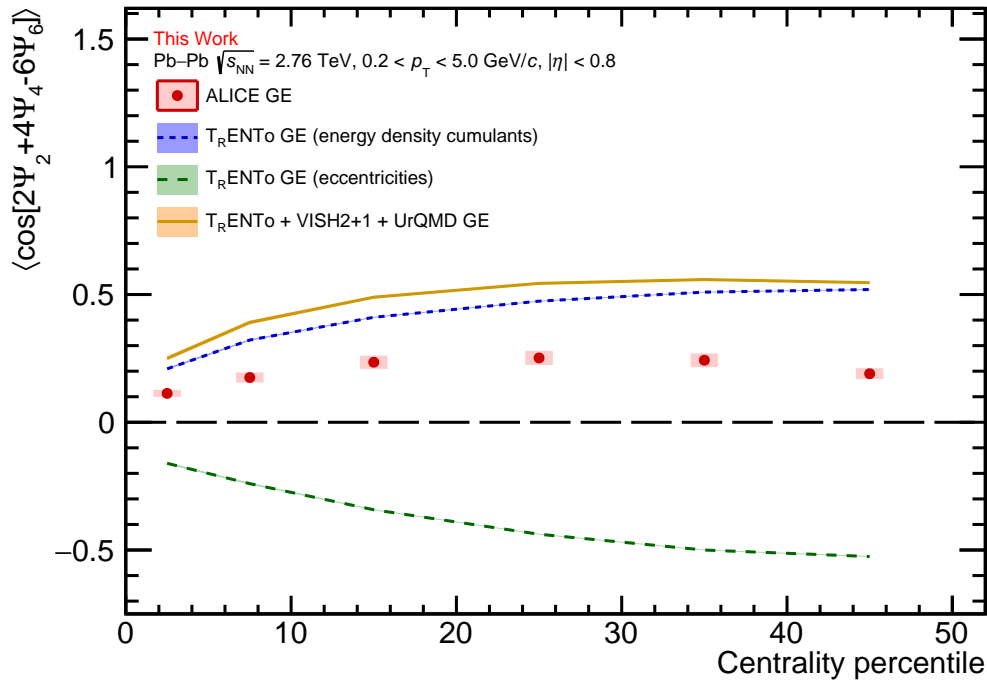


Figure 7.9: Comparison of the T<sub>R</sub>ENTo and iEBE-VISHNU models to the measured ALICE data of  $\langle \cos[2\Psi_2 + 4\Psi_4 - 6\Psi_6] \rangle$ .

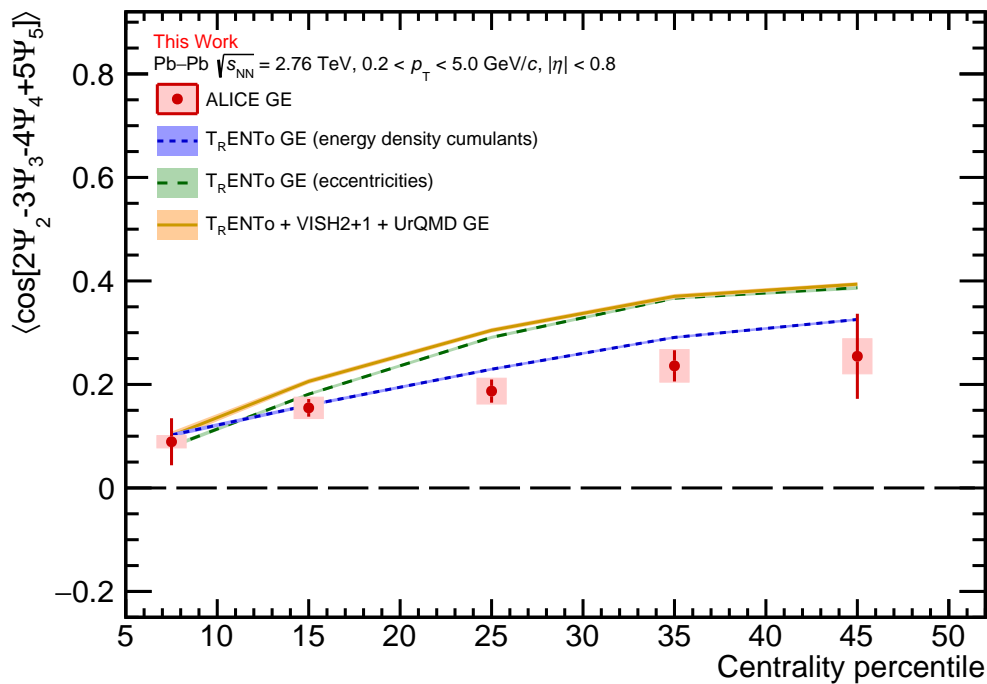


Figure 7.10: Comparison of the T<sub>R</sub>ENTo and iEBE-VISHNU model to the measured ALICE data of  $\langle \cos[2\Psi_2 - 3\Psi_3 - 4\Psi_4 + 5\Psi_5] \rangle$ .

# Chapter 8

## Summary

In this thesis, a new method for measuring symmetry plane correlations in ultrarelativistic heavy-ion collisions has been presented based on [72]. This so-called Gaussian Estimator shows a great improvement over existing estimators for SPC, which are biased due to the neglect of correlations between the flow amplitudes. The study of the symmetry planes is particularly interesting, as they are the second degree of freedom in the Fourier series used to describe the distribution of azimuthal angles of produced particles. This distribution contains the information about the initial coordinate anisotropy of the heavy-ion collision as well as the collective evolution of the QGP.

Furthermore, a new cumulant for symmetry plane correlations, abbreviated as CSC, has been discussed in this thesis. The conceptual feasibility of the CSC has been demonstrated by carefully designed toy Monte Carlo studies. Additionally, predictions from realistic Monte Carlo generators have been presented. The study of these observables would allow the access to new information on the QGP and the genuine correlations between different symmetry plane correlations.

Using the ALICE detector at the LHC, the new Gaussian Estimator has been used for the first time in Pb–Pb collisions at  $\sqrt{s_{\text{NN}}} = 2.76$  TeV recorded in 2010. In particular, the presented analysis is based on tracks reconstructed only with the information from the TPC, which has a great uniform acceptance in azimuthal angles important for flow analyses. Various detector inefficiencies have been accounted for by removing high multiplicity outliers and correcting non-uniform efficiencies for the transverse momenta  $p_{\text{T}}$  of reconstructed particles. Using the Barlow test, a total of twelve systematic checks have been performed to study the effects of the event and track selections. The statistically significant deviations between these trials and the default analysis have been accounted for in the systematic errors of the presented results. In addition to that, by using the HIJING Monte Carlo generator anchored to detector conditions from ALICE real data, it has been demonstrated that the performed analysis is not biased by non-flow contributions in the centrality range of 0–50%.

In total, four combinations for correlations between each two and three symmetry planes, as well as the first experimental measurement of a SPC between four planes, have been extracted. The results show significant lower signals for the SPC when compared to the results of previous analyses. Employing state-of-the-art models for the initial state given by  $\text{T}_\text{R} \text{E} \text{N} \text{T} \text{o}$  and for the final state by  $\text{T}_\text{R} \text{E} \text{N} \text{T} \text{o} + \text{iE} \text{B} \text{E} \text{-V} \text{I} \text{S} \text{H} \text{N} \text{U}$ , a comparison between theoretical predictions and the experimental data has been performed. Utilizing the linear and non-linear response formalism, one could in particular see that theoretical predictions describe the experimental data very well only in the region where the linear response dominates. Additionally, SPC involving higher order harmonics like  $\Psi_6$  are

only poorly described by the model. This in particular will allow to further tune model parameters using the here presented experimental data as input.

Future analyses of SPC will have to study these novel correlations differentially for different pseudorapidity  $\eta$  and transverse momentum  $p_T$  ranges. This will be feasible with the larger statistics of the LHC Run 2 data sets and beyond, which will also allow to decrease the statistical errors of the presented analysis. Further, the experimental feasibility of the CSC and its application on real data, will be addressed in future studies as well.

# Appendix A

## Basics of flow

### A.1 Proof of $\langle \exp [in (\varphi - \Psi_n)] \rangle = v_n$

In this section, the statements

$$\langle \cos [n (\varphi - \Psi_n)] \rangle = v_n, \quad (\text{A.1})$$

and

$$\langle \sin [n (\varphi - \Psi_n)] \rangle = 0, \quad (\text{A.2})$$

will be proven simultaneously by the calculation of the expectation value

$$\langle e^{in(\varphi - \Psi_n)} \rangle. \quad (\text{A.3})$$

First, the p.d.f. provided in Eq. (2.15) is rewritten as

$$f(\varphi) = \frac{1}{2\pi} \left[ 1 + 2 \sum_{n=1}^{\infty} v_n \cos [n (\varphi - \Psi_n)] \right] \quad (\text{A.4})$$

$$= \frac{1}{2\pi} \left[ 1 + \sum_{n=1}^{\infty} v_n [e^{in(\varphi - \Psi_n)} + e^{-in(\varphi - \Psi_n)}] \right] \quad (\text{A.5})$$

$$= \frac{1}{2\pi} \left[ 1 + \sum_{n=1}^{\infty} [V_n^* e^{in\varphi} + V_n e^{-in\varphi}] \right], \quad (\text{A.6})$$

where in the last line the complex flow harmonics

$$V_n = v_n e^{in\Psi_n} \quad (\text{A.7})$$

$$V_n^* = v_n e^{-in\Psi_n} \quad (\text{A.8})$$

have been used. By defining  $V_0 = 1$  [33] and using  $V_{-n} = V_n^*$  (i.e.  $v_{-n} = v_n$  and  $\Psi_{-n} = \Psi_n$ ), one can further simplify the p.d.f. to

$$f(\varphi) = \frac{1}{2\pi} \sum_{n=-\infty}^{\infty} V_n e^{-in\varphi}. \quad (\text{A.9})$$

Thus, one can compute  $\langle e^{in(\varphi-\Psi_n)} \rangle$  as

$$\langle e^{in(\varphi-\Psi_n)} \rangle = \int_0^{2\pi} d\varphi e^{in(\varphi-\Psi_n)} f(\varphi) \quad (\text{A.10})$$

$$= \int_0^{2\pi} d\varphi e^{in(\varphi-\Psi_n)} \frac{1}{2\pi} \sum_{m=-\infty}^{\infty} V_m e^{-im\varphi} \quad (\text{A.11})$$

$$= \frac{1}{2\pi} \sum_{m=-\infty}^{\infty} \int_0^{2\pi} d\varphi e^{in(\varphi-\Psi_n)} V_m e^{-im\varphi} \quad (\text{A.12})$$

$$= \frac{1}{2\pi} \sum_{m=-\infty}^{\infty} \int_0^{2\pi} d\varphi v_m e^{i(m\Psi_m-n\Psi_n)} e^{in(i\varphi(n-m))}. \quad (\text{A.13})$$

Using

$$\int_0^{2\pi} d\varphi e^{in(i\varphi(n-m))} = 2\pi \delta_{m,n}, \quad (\text{A.14})$$

with  $\delta_{m,n}$  being the Kronecker delta, leads to the final result

$$\langle e^{in(\varphi-\Psi_n)} \rangle = v_n. \quad (\text{A.15})$$

In particular, this means for the real part

$$\langle \cos [n(\varphi - \Psi_n)] \rangle = v_n, \quad (\text{A.16})$$

and the imaginary part

$$\langle \sin [n(\varphi - \Psi_n)] \rangle = 0. \quad (\text{A.17})$$

## A.2 Importance of the isotropy condition

Consider a generic flow observable  $v_{n_1} v_{n_2} \dots v_{n_k} e^{i(n_1 \Psi_{n_1} + n_2 \Psi_{n_2} + \dots + n_k \Psi_{n_k})}$  with a set of flow harmonics  $\{n_1, \dots, n_k\}$ . To calculate its all-event average, it has to be integrated over the p.d.f.  $f(v_1, \dots, \Psi_1, \dots)$ , which contains the information on how the flow amplitudes and symmetry planes fluctuate per event, i.e.

$$\begin{aligned} \langle v_{n_1} v_{n_2} \dots v_{n_k} e^{i(n_1 \Psi_{n_1} + n_2 \Psi_{n_2} + \dots + n_k \Psi_{n_k})} \rangle &= \int v_{n_1} v_{n_2} \dots v_{n_k} e^{i(n_1 \Psi_{n_1} + n_2 \Psi_{n_2} + \dots + n_k \Psi_{n_k})} \\ &\quad \cdot f(v_1, \dots, \Psi_1, \dots) dv_{n_1} \dots v_{n_k} d\Psi_{n_1} \dots \Psi_{n_k}. \end{aligned} \quad (\text{A.18})$$

In particular, the information about the symmetry planes is given relative to the impact parameter vector  $\vec{b}$ , as any physical fluctuations are only meaningful with respect to  $\vec{b}$ . However, in the experiment the orientation  $\vec{b}$  is not fixed in respect to the laboratory frame and fluctuates event-by-event. This random orientation of  $\vec{b}$  is characterised by the fluctuation of the reaction plane  $\Psi_{RP} \in [0, 2\pi)$ . To account for these fluctuations, any ‘‘measured’’ symmetry plane have to be transformed as  $\Psi_n \rightarrow \Psi_n - \Psi_{RP} \equiv \Psi_n^*$ . Therefore, in the all-event average one has to perform an additional integration

$$\frac{1}{2\pi} \int_0^{2\pi} d\Psi_{RP} \langle v_{n_1} v_{n_2} \dots v_{n_k} e^{i(n_1 \Psi_{n_1}^* + n_2 \Psi_{n_2}^* + \dots + n_k \Psi_{n_k}^*)} \rangle, \quad (\text{A.19})$$

where the factor  $1/(2\pi)$  is the proper normalisation for the p.d.f. of the fluctuations of  $\Psi_{RP}$ . In particular, the flow observable  $v_{n_1}v_{n_2}\dots v_{n_k}e^{i(n_1\Psi_{n_1}+n_2\Psi_{n_2}+\dots+n_k\Psi_{n_k})}$  transforms as

$$v_{n_1}v_{n_2}\dots v_{n_k}e^{i(n_1\Psi_{n_1}+n_2\Psi_{n_2}+\dots+n_k\Psi_{n_k})} \rightarrow v_{n_1}v_{n_2}\dots v_{n_k}e^{i(n_1\Psi_{n_1}^*+n_2\Psi_{n_2}^*+\dots+n_k\Psi_{n_k}^*)}\cdot e^{-i(n_1+\dots+n_k)\Psi_{RP}}. \quad (\text{A.20})$$

Note that the transformed flow observable only differs in the prefactor  $e^{-i(n_1+\dots+n_k)\Psi_{RP}}$ , thus

$$\begin{aligned} & \frac{1}{2\pi} \int_0^{2\pi} d\Psi_{RP} \langle v_{n_1}v_{n_2}\dots v_{n_k} e^{i(n_1\Psi_{n_1}^*+n_2\Psi_{n_2}^*+\dots+n_k\Psi_{n_k}^*)} \rangle \\ &= \langle v_{n_1}v_{n_2}\dots v_{n_k} e^{i(n_1\Psi_{n_1}+n_2\Psi_{n_2}+\dots+n_k\Psi_{n_k})} \rangle \cdot \frac{1}{2\pi} \int_0^{2\pi} d\Psi_{RP} e^{-i(n_1+\dots+n_k)\Psi_{RP}}. \end{aligned} \quad (\text{A.21})$$

If the isotropy condition  $n_1 + \dots + n_k = 0$  is fulfilled, this prefactor is trivially equal to one and the averaging over  $\Psi_{RP}$  has no effect on the final observables, i.e. its physics information is unchanged. However, if  $n_1 + \dots + n_k \equiv m \neq 0$ , the integral becomes

$$\frac{1}{2\pi} \int_0^{2\pi} d\Psi_{RP} e^{-im\Psi_{RP}} = 0, \quad (\text{A.22})$$

leading to trivial zero in the all-event average of the measured flow observable.

### A.3 P.D.F. characteristics

In this section, the basic mathematical properties of the p.d.f.

$$f(\varphi) = \frac{1}{2\pi} \left[ 1 + 2 \sum_{n=1}^{\infty} v_n \cos[n(\varphi - \Psi_n)] \right], \quad (\text{A.23})$$

are investigated. Based on the Kolmogorow axioms, a p.d.f. has to fulfil two important criteria: the p.d.f. has to be equal to 1 when integrated over the whole space (the so-called *unity*) and it has to be non-negative [100]. Both of these criteria are shown in the following for the p.d.f. in Eq. A.23:

1. Unity is trivially fulfilled, i.e. no condition on  $v_n$  and  $\Psi_n$  have to be imposed as

$$\int_0^{2\pi} d\varphi f(\varphi) \stackrel{!}{=} 1 \quad (\text{A.24})$$

$$\int_0^{2\pi} d\varphi \frac{1}{2\pi} \left[ 1 + 2 \sum_{n=1}^{\infty} v_n \cos[n(\varphi - \Psi_n)] \right] \quad (\text{A.25})$$

$$= 1 + \frac{1}{\pi} \int_0^{2\pi} d\varphi \sum_{n=1}^{\infty} v_n \cos[n(\varphi - \Psi_n)] \quad (\text{A.26})$$

$$= 1 + \frac{1}{\pi} \sum_{n=1}^{\infty} \int_0^{2\pi} d\varphi v_n \cos[n(\varphi - \Psi_n)] \quad (\text{A.27})$$

$$= 1 + \sum_{n=1}^{\infty} v_n \underbrace{\frac{\sin(n\Psi_n) - \sin(n\Psi_n - n2\pi)}{n\pi}}_{=0} \quad (\text{A.28})$$

$$= 1 \quad (\text{A.29})$$

In the latter step, the  $2\pi$  periodicity of the sinus

$$\sin(n\Psi_n - n2\pi) = \sin(n\Psi_n) \cos(2\pi n) - \sin(n2\pi) \cos(n\Psi_n) = \sin(n\Psi_n), \quad (\text{A.30})$$

has been used.

## 2. Non-Negativity

$$\forall \varphi : f(\varphi) = \frac{1}{2\pi} \left[ 1 + 2 \sum_{n=1}^{\infty} v_n \cos[n(\varphi - \Psi_n)] \right] \geq 0 \quad (\text{A.31})$$

Let's consider two extreme cases to find the uppermost and lowermost bounds, namely

$$\exists \varphi_0 \forall n : \cos[n(\varphi_0 - \Psi_n)] = 1 \quad (\text{A.32})$$

$$\exists \varphi_0 \forall n : \cos[n(\varphi_0 - \Psi_n)] = -1. \quad (\text{A.33})$$

Both cases can exist by artificially adjusting  $\Psi_n$ . Then one obtains

$$1 + 2 \sum_{n=1}^{\infty} v_n \geq 0 \quad (\text{A.34})$$

$$1 - 2 \sum_{n=1}^{\infty} v_n \geq 0. \quad (\text{A.35})$$

Therefore,

$$\sum_{n=1}^{\infty} v_n \geq -\frac{1}{2} \quad (\text{A.36})$$

$$\sum_{n=1}^{\infty} v_n \leq \frac{1}{2} \quad (\text{A.37})$$

$$\implies \left| \sum_{n=1}^{\infty} v_n \right| \leq \frac{1}{2} \quad (\text{A.38})$$

As  $v_n$  are per construction positive, the lower boundary is trivially fulfilled.

# Appendix B

## Supplements for new formalisms for SPC

### B.1 Choice of correlators in the GE

In this section<sup>1</sup>, the most general form of multiparticle correlators is used to derive constraints for their application in the GE. This procedure generates rules for the coefficients  $a_i$  used in Eq. (5.11).

Considering two general multiparticle correlators  $\langle k \rangle_{n_1, n_2, \dots, n_k}$  ( $k$ -particle correlator with set of harmonics  $\{n_1, n_2, \dots, n_k\}$ ) and  $\langle l \rangle_{p_1, p_2, \dots, p_l}$  ( $l$ -particle correlator with set of harmonics  $\{p_1, p_2, \dots, p_l\}$ ), their all-event ratio can in general be written as

$$\frac{\langle \langle k \rangle_{n_1, n_2, \dots, n_k} \rangle}{\sqrt{\langle \langle l \rangle_{p_1, p_2, \dots, p_l} \rangle}} \propto \frac{\langle v_{n_1} \dots v_{n_k} e^{i(n_1 \Psi_{n_1} + \dots + n_k \Psi_{n_k})} \rangle}{\sqrt{\langle v_{p_1} \dots v_{p_l} e^{i(p_1 \Psi_{p_1} + \dots + p_l \Psi_{p_l})} \rangle}}. \quad (\text{B.1})$$

The above equation presents the most general ratio in terms of multiparticle correlators as it is given in the GE (Eq. (5.11)). Utilizing this general ansatz, the following constraints have to be satisfied to obtain the desired GE:

$$\sum_{j=1}^k n_j = 0 \quad (\text{B.2})$$

$$\sum_{j=1}^l p_j = 0 \quad (\text{B.3})$$

$$\sum_{j=1}^k n_j \cdot \Psi_{n_j} \neq 0 \quad (\text{B.4})$$

$$\sum_{j=1}^l p_j \cdot \Psi_{p_j} = 0 \quad (\text{B.5})$$

$$\prod_{i=1}^k v_{n_i}^2 = \prod_{i=1}^l v_{p_i}. \quad (\text{B.6})$$

The constraints (B.2) and (B.3) ensure the isotropy condition, which has to be fulfilled for any non-trivial multiparticle correlator. The constraint (B.4) leads to a non-vanishing

---

<sup>1</sup>This section is based on [72].

contribution of symmetry planes in the numerator, while the constraint (B.5) ensures that the denominator does not depend explicitly on symmetry planes. The last constraint (B.6) enforces that the product of flow amplitudes in numerator is equal to the product of flow amplitudes squared in the denominator. In particular, from the constraint (B.6), it follows directly that  $l = 2k$ . Therefore, the numerator uses a  $k$ -particle correlator while the one in the denominator is of order  $2k$ . To obtain a particular SPC, one has to choose specific sets of correlators  $\{n_1, n_2, \dots, n_k\}$  and  $\{p_1, p_2, \dots, p_{2k}\}$ , which have to fulfil the constraints in Eqs. (B.2) - (B.6). In the following, this approach is discussed for the SPC between two symmetry planes  $\Psi_m$  and  $\Psi_n$ . It will be shown that strict constraints for the coefficients  $a_i$  emerge for the case of two planes. The presented formalism can be generalized for correlations between any number of symmetry planes, which will be further demonstrated in the case for three symmetry planes.

### B.1.1 Correlators between two symmetry planes

Focussing on the SPC between two planes  $\Psi_m$  and  $\Psi_n$ , the general sets of harmonics with  $m$  and  $n$  (where  $m \neq n$ ) can be set up as

$$\left\{ \underbrace{m, \dots, m}_{a_m \text{ times}}, \underbrace{-n, \dots, -n}_{a_n \text{ times}} \right\} \quad (\text{numerator}) \quad (\text{B.7})$$

$$\left\{ \underbrace{m, -m, \dots, m, -m}_{2a_m \text{ times}}, \underbrace{n, -n, \dots, n, -n}_{2a_n \text{ times}} \right\} \quad (\text{denominator}), \quad (\text{B.8})$$

where  $a_m, a_n \in \mathbb{N}$ . These sets explicitly fulfil the constraints in Eq. (B.4) to Eq. (B.6). Given the constraints Eq. (B.2) and Eq. (B.3), the following rules for  $a_m$  and  $a_n$  have to be satisfied

$$\sum_{j=1}^{a_m} m + \sum_{k=1}^{a_n} (-n) = a_m m - a_n n = 0 \implies \frac{a_m}{n} = \frac{a_n}{m}, \quad (\text{B.9})$$

and

$$\sum_{j=1}^{2a_m} (-1)^j \cdot m + \sum_{k=1}^{2a_n} (-1)^k \cdot n = 0 \implies 2a_m \wedge 2a_n \text{ even}. \quad (\text{B.10})$$

In the latter equation,  $\wedge$  denotes the logical AND. With this, the constraints from Eq. (B.2) and Eq. (B.3) are fulfilled as well. In particular, Eq. (B.10) is true for any choice of  $a_m$  and  $a_n$ .

With this approach, the smallest possible valid choice of the coefficients  $a_m$  and  $a_n$  for the SPC between two planes is given as

$$a_m = \frac{l_{mn}}{m}, \quad (\text{B.11})$$

$$a_n = \frac{l_{mn}}{n}, \quad (\text{B.12})$$

where  $l_{mn}$  denotes the least common multiple between  $m$  and  $n$ . With this, the order of the multiparticle correlator in the numerator is given as

$$l_{mn} \left( \frac{1}{m} + \frac{1}{n} \right), \quad (\text{B.13})$$

while the denominator has an order twice that large. Any other choice of the coefficients will exhibit higher order of correlators. Thus, the lowest order GE for two symmetry planes is given as

$$\langle \cos [l_{mn} (\Psi_m - \Psi_n)] \rangle_{\text{GE}} \propto \frac{\langle v_m^{a_m} v_n^{a_n} \cos [l_{mn} (\Psi_m - \Psi_n)] \rangle}{\sqrt{\langle v_m^{2a_m} v_n^{2a_n} \rangle}}. \quad (\text{B.14})$$

Although this method of using the least common multiple presents the lowest possible order correlators, any multiple  $k \in \mathbb{N}$  of this method results in a valid correlator as well. Thus, one can expand the set of correlators by transforming  $a_m \rightarrow ka_m$  and  $a_n \rightarrow ka_n$ , resulting in the more general expression

$$\langle \cos [kl_{mn} (\Psi_m - \Psi_n)] \rangle_{\text{GE}} \propto \frac{\langle v_m^{ka_m} v_n^{ka_n} \cos [kl_{mn} (\Psi_m - \Psi_n)] \rangle}{\sqrt{\langle v_m^{2ka_m} v_n^{2ka_n} \rangle}}. \quad (\text{B.15})$$

### B.1.2 Correlators between three symmetry planes

Consider three symmetry planes of distinct harmonics  $m$ ,  $n$  and  $p$ . Satisfying the constraints in Eq. (B.4) to Eq. (B.6), the following general choice for the set of harmonics can be made:

$$\left\{ \underbrace{m, \dots, m}_{a_m \text{ times}}, \underbrace{-n, \dots, -n}_{a_n \text{ times}}, \underbrace{-p, \dots, -p}_{a_p \text{ times}} \right\} \quad (\text{numerator}) \quad (\text{B.16})$$

$$\left\{ \underbrace{m, -m, \dots, m, -m}_{2a_m \text{ times}}, \underbrace{n, -n, \dots, n, -n}_{2a_n \text{ times}}, \underbrace{p, -p, \dots, p, -p}_{2a_p \text{ times}} \right\} \quad (\text{denominator}) \quad (\text{B.17})$$

Following the same approach as for the SPC between two planes, the following constraints on  $a_m$ ,  $a_n$  and  $a_p$

$$\sum_{j=1}^{a_m} m + \sum_{k=1}^{a_n} (-n) + \sum_{l=1}^{a_p} (-p) = a_m m - a_n n - a_p p = 0 \quad (\text{B.18})$$

$$\sum_{j=1}^{2a_m} (-1)^j \cdot m + \sum_{k=1}^{2a_n} (-1)^k \cdot n + \sum_{l=1}^{2a_p} (-1)^l \cdot p = 0 \implies 2a_m \wedge 2a_n \wedge 2a_p \text{ even}, \quad (\text{B.19})$$

are derived. Again, the second constraint is fulfilled trivially. The correlators for the SPC between three planes will, in general, be of high order, limiting the experimental feasibility. Due to the large amount of possible combinatorial solutions for Eq. (B.18), a closed formula for the coefficients  $a_i$  cannot be found as it was the case for two symmetry planes. However, a trivial example for the special case  $m = n + p$  can be found as  $a_m = a_n = a_p = 1$ . In particular, in this case the GE takes the following form

$$\langle \cos [m\Psi_m - n\Psi_n - p\Psi_p] \rangle_{\text{GE}} \propto \frac{\langle v_m v_n v_p \cos [m\Psi_m - n\Psi_n - p\Psi_p] \rangle}{\sqrt{\langle v_m^2 v_n^2 v_p^2 \rangle}}. \quad (\text{B.20})$$

## B.2 Cumulant properties of CSC

In this section, the cumulant properties of

$$\text{CSC}(b\delta_{c,d}, k\delta_{l,m}) = \left\langle e^{i(b\delta_{c,d} + k\delta_{l,m})} \right\rangle - \langle e^{ib\delta_{c,d}} \rangle \langle e^{ik\delta_{l,m}} \rangle. \quad (\text{B.21})$$

are demonstrated according to [97].

### B.2.1 Statistical independence

Assuming that the variables  $\delta_{c,d}$  and  $\delta_{l,m}$  are independent from each other, one obtains

$$\begin{aligned} \text{CSC}(b\delta_{c,d}, k\delta_{l,m}) &= \left\langle e^{i(b\delta_{c,d} + k\delta_{l,m})} \right\rangle - \left\langle e^{ib\delta_{c,d}} \right\rangle \left\langle e^{ik\delta_{l,m}} \right\rangle \\ &= \left\langle e^{ib\delta_{c,d}} \right\rangle \left\langle e^{ik\delta_{l,m}} \right\rangle - \left\langle e^{ib\delta_{c,d}} \right\rangle \left\langle e^{ik\delta_{l,m}} \right\rangle \\ &= 0. \end{aligned} \quad (\text{B.22})$$

Thus, the statistical independence is fulfilled.

### B.2.2 Reduction

Considering the equality  $e^{ib\delta_{c,d}} = e^{ik\delta_{l,m}}$ , the reduction is fulfilled as

$$\text{CSC}(b\delta_{c,d}, b\delta_{c,d}) = \left\langle e^{i2b\delta_{c,d}} \right\rangle - \left( \left\langle e^{ib\delta_{c,d}} \right\rangle \right)^2. \quad (\text{B.23})$$

The above equation presents the equation for  $\kappa_2$ .

### B.2.3 Semi-invariance

Using two constants  $c_1$  and  $c_2$ , the semi-invariance is proven by

$$\begin{aligned} &\left\langle (e^{ib\delta_{c,d}} + c_1) (e^{ik\delta_{l,m}} + c_2) \right\rangle - \left\langle (e^{ib\delta_{c,d}} + c_1) \right\rangle \left\langle (e^{ik\delta_{l,m}} + c_2) \right\rangle \\ &= \left\langle e^{i(b\delta_{c,d} + k\delta_{l,m})} \right\rangle + c_1 \left\langle e^{ik\delta_{l,m}} \right\rangle + c_2 \left\langle e^{ib\delta_{c,d}} \right\rangle + c_1 c_2 - \\ &\quad \left( \left\langle e^{ib\delta_{c,d}} \right\rangle \left\langle e^{ik\delta_{l,m}} \right\rangle + c_1 \left\langle e^{ik\delta_{l,m}} \right\rangle + c_2 \left\langle e^{ib\delta_{c,d}} \right\rangle + c_1 c_2 \right) \\ &= \left\langle e^{i(b\delta_{c,d} + k\delta_{l,m})} \right\rangle - \left\langle e^{ib\delta_{c,d}} \right\rangle \left\langle e^{ik\delta_{l,m}} \right\rangle \\ &= \text{CSC}(b\delta_{c,d}, k\delta_{l,m}). \end{aligned} \quad (\text{B.24})$$

### B.2.4 Homogeneity

Considering the two constants  $c_1$  and  $c_2$ , one obtains

$$\begin{aligned} &\left\langle (c_1 e^{ib\delta_{c,d}}) (c_2 e^{ik\delta_{l,m}}) \right\rangle - \left\langle (c_1 e^{ib\delta_{c,d}}) \right\rangle \left\langle (c_2 e^{ik\delta_{l,m}}) \right\rangle \\ &= c_1 c_2 \text{CSC}(b\delta_{c,d}, k\delta_{l,m}), \end{aligned} \quad (\text{B.25})$$

and therefore, the homogeneity requirement is fulfilled.

### B.2.5 Multilinearity

The multilinearity condition is proven correct by using an additional stochastic observable  $e^{ix\delta_{y,z}}$ . Then, one can see

$$\begin{aligned} &\left\langle e^{ib\delta_{c,d}} (e^{ik\delta_{l,m}} + e^{ix\delta_{y,z}}) \right\rangle - \left\langle e^{ib\delta_{c,d}} \right\rangle \left\langle (e^{ik\delta_{l,m}} + e^{ix\delta_{y,z}}) \right\rangle \\ &= \left\langle e^{i(b\delta_{c,d} + k\delta_{l,m})} \right\rangle + \left\langle e^{i(b\delta_{c,d} + x\delta_{y,z})} \right\rangle - \left( \left\langle e^{ib\delta_{c,d}} \right\rangle \left\langle e^{ik\delta_{l,m}} \right\rangle + \left\langle e^{ib\delta_{c,d}} \right\rangle \left\langle e^{ix\delta_{y,z}} \right\rangle \right) \\ &= \left( \left\langle e^{i(b\delta_{c,d} + k\delta_{l,m})} \right\rangle - \left\langle e^{ib\delta_{c,d}} \right\rangle \left\langle e^{ik\delta_{l,m}} \right\rangle \right) + \left( \left\langle e^{i(b\delta_{c,d} + x\delta_{y,z})} \right\rangle - \left\langle e^{ib\delta_{c,d}} \right\rangle \left\langle e^{ix\delta_{y,z}} \right\rangle \right) \\ &= \text{CSC}(b\delta_{c,d}, k\delta_{l,m}) + \text{CSC}(b\delta_{c,d}, x\delta_{y,z}). \end{aligned} \quad (\text{B.26})$$

# Appendix C

## Non-flow studies

In this section, the non-flow studies of the multiparticle correlators of the numerator and denominator in the GE are present. The results concerning the correlations between two symmetry planes are shown in Figs.C.1-C.3, between three planes in Figs. C.4-C.7 and for the SPC between four planes in Fig. C.8. All of the provided results show that non-flow is not significant and compatible with zero when compared to the signal of the real data.

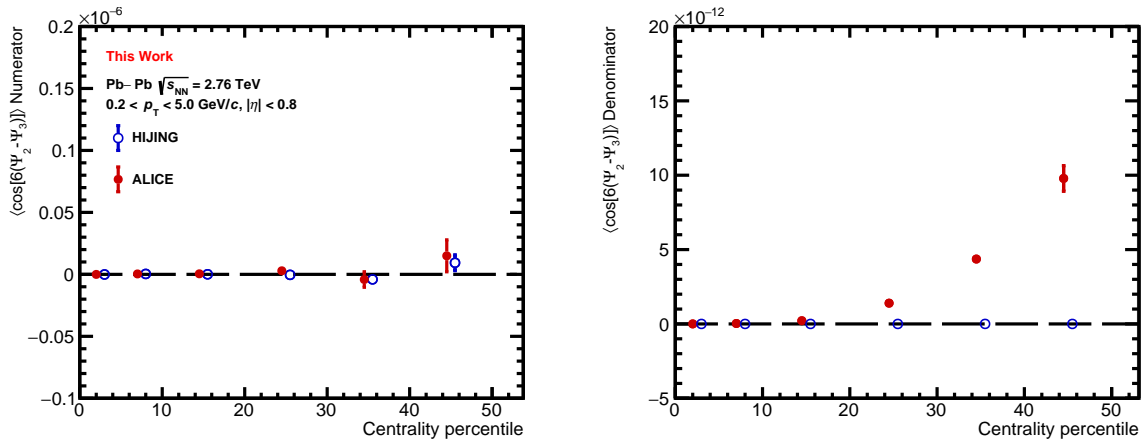


Figure C.1: Comparison of the multiparticle correlators from the numerator and denominator in the GE of  $\langle \cos [4 (\Psi_4 - \Psi_2)] \rangle$  obtained with HIJING and the real experimental data.

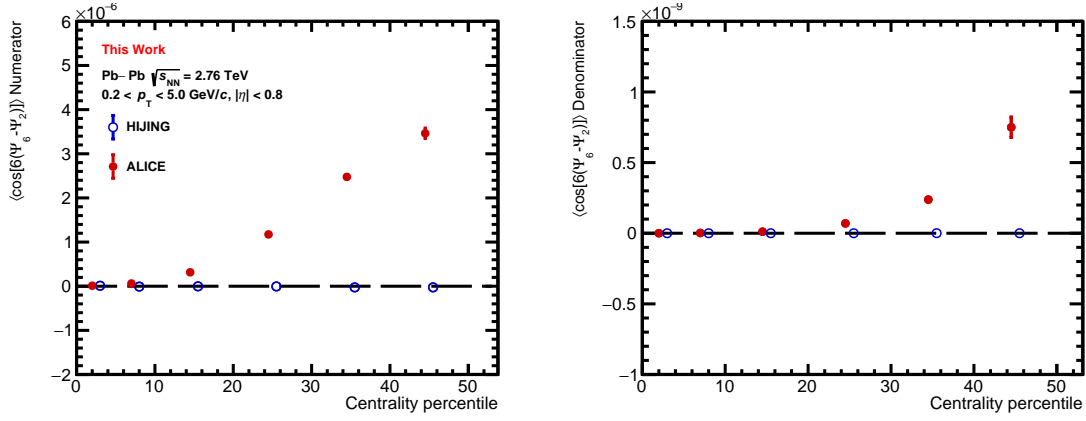


Figure C.2: Comparison of the multiparticle correlators from the numerator and denominator in the GE of  $\langle \cos [6(\Psi_6 - \Psi_2)] \rangle$  obtained with HIJING and the real experimental data.

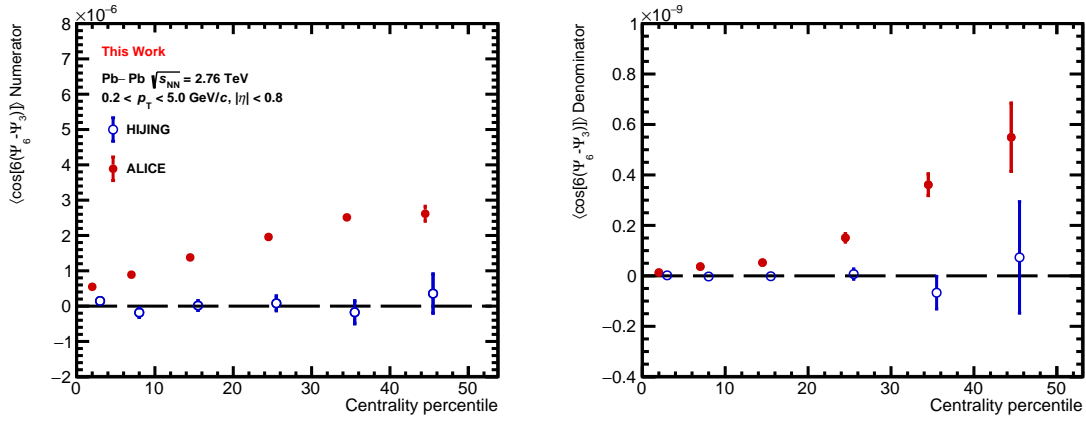


Figure C.3: Comparison of the multiparticle correlators from the numerator and denominator in the GE of  $\langle \cos [6(\Psi_6 - \Psi_3)] \rangle$  obtained with HIJING and the real experimental data.

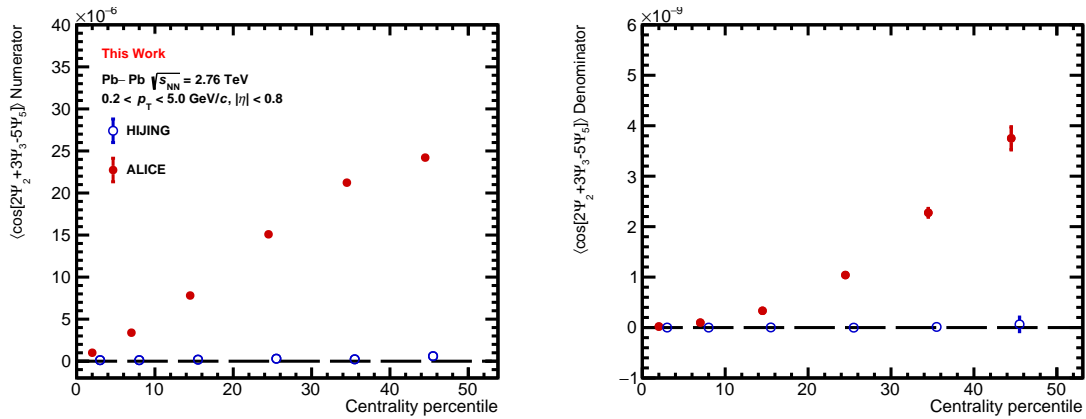


Figure C.4: Comparison of the multiparticle correlators from the numerator and denominator in the GE of  $\langle \cos [2\Psi_2 + 3\Psi_3 - 5\Psi_5] \rangle$  obtained with HIJING and the real experimental data.

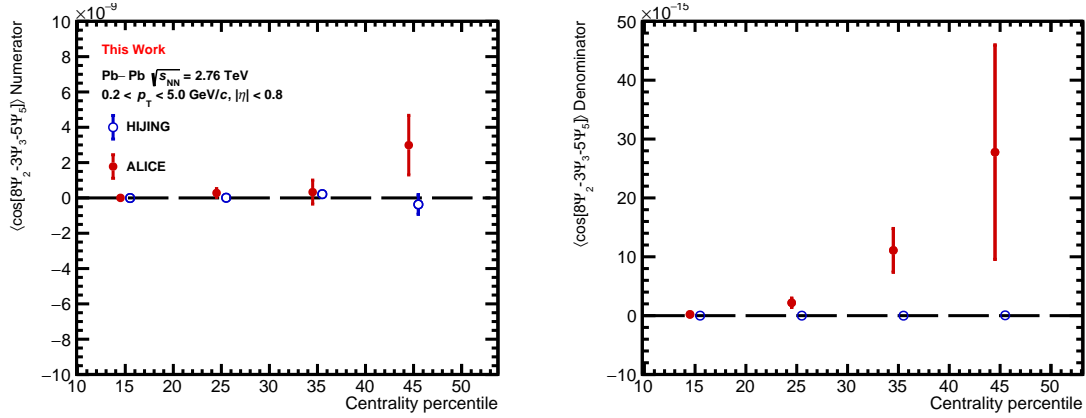


Figure C.5: Comparison of the multiparticle correlators from the numerator and denominator in the GE of  $\langle \cos [8\Psi_2 - 3\Psi_3 - 5\Psi_5] \rangle$  obtained with HIJING and the real experimental data.

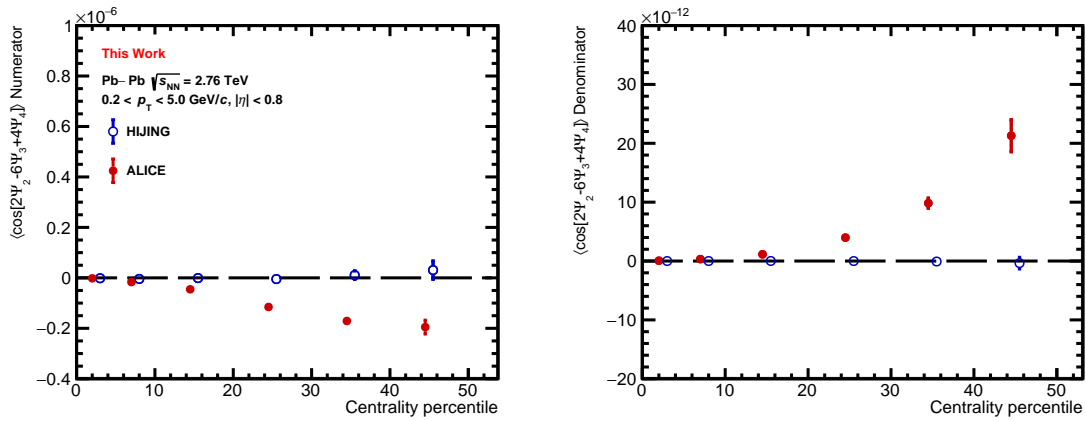


Figure C.6: Comparison of the multiparticle correlators from the numerator and denominator in the GE of  $\langle \cos [2\Psi_2 - 6\Psi_3 + 4\Psi_4] \rangle$  obtained with HIJING and the real experimental data.

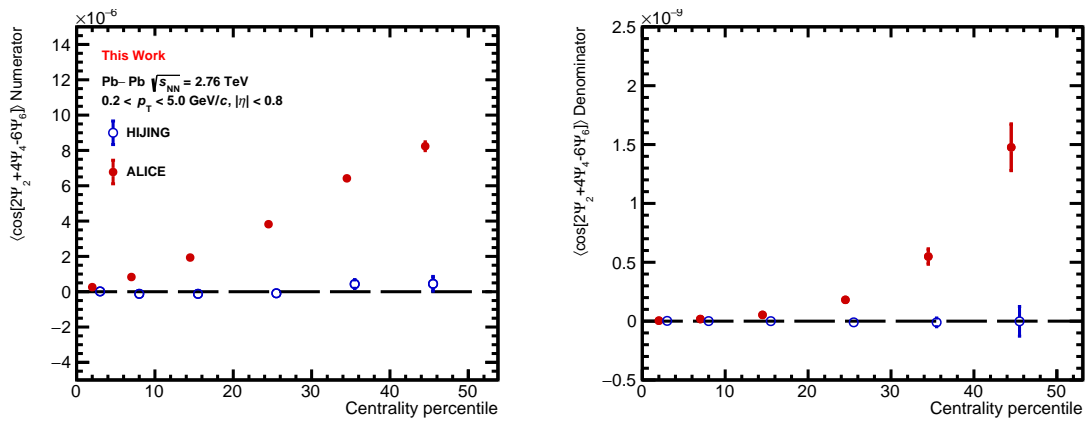


Figure C.7: Comparison of the multiparticle correlators from the numerator and denominator in the GE of  $\langle \cos [2\Psi_2 + 4\Psi_4 - 6\Psi_6] \rangle$  obtained with HIJING and the real experimental data.

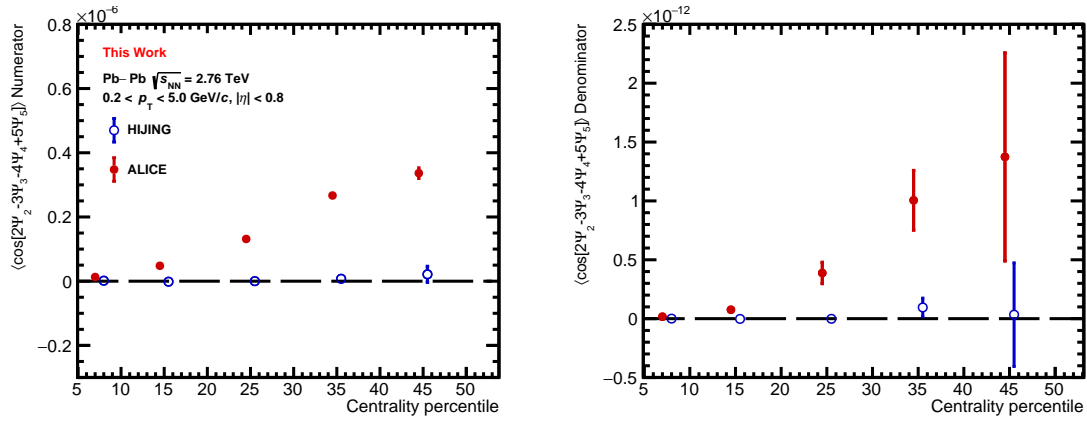


Figure C.8: Comparison of the multiparticle correlators from the numerator and denominator in the GE of  $\langle \cos[2\Psi_2 - 3\Psi_3 - 4\Psi_4 + 5\Psi_5] \rangle$  obtained with HIJING and the real experimental data.

# Appendix D

## Statistical error propagation

In this chapter, the basics of the statistical errors and the error propagation are discussed for the most general case. After this, the specific error propagation for the GE is presented.

### D.1 Errors of one-dimensional variables

Consider a one-dimensional, random variable  $x$  with a p.d.f.  $f(x)$ . Two of the most important characteristics of this p.d.f. are its mean  $\mu_x$  and its variance  $\sigma_x^2$  (also written as  $V[x]$ ) which are defined as

$$\mu_x = E[x] = \int_{-\infty}^{\infty} x f(x) dx, \quad (\text{D.1})$$

and

$$\sigma_x^2 = V[x] = E[(x - E[x])^2] = E[x^2] - E[x]^2 = \int_{-\infty}^{\infty} (x - \mu_x)^2 f(x) dx. \quad (\text{D.2})$$

In the above equations  $E(g(x))$  denotes the expectation value of a function  $g(x)$  depending on the random variable  $x$ . In general, the p.d.f. of the random variable  $x$  is unknown. To infer onto a property  $\theta$  of the p.d.f., the so-called estimators  $\hat{\theta}$  are used. These estimators are general functions of a set of  $n$  independent observations of  $x$  (a so-called sample) [100]. As the estimator  $\hat{\theta}$  is a function of the random variable  $x$ , it is itself a random variable following a sampling p.d.f.  $g(\hat{\theta}; \theta)$ . The expectation value of the estimator can thus be expressed as [100]

$$\begin{aligned} E[\hat{\theta}(\mathbf{x})] &= \int \hat{\theta} g(\hat{\theta}; \theta) d\hat{\theta} \\ &= \int \hat{\theta}(\mathbf{x}) f(x_1, \theta) \cdots f(x_n, \theta) dx_1 \cdots dx_n. \end{aligned} \quad (\text{D.3})$$

The *bias* of an estimator is defined as

$$b = E[\hat{\theta}] - \theta. \quad (\text{D.4})$$

An estimator with  $b = 0$  independent of the sample size is called *unbiased*.

With these definitions, the *sample mean*  $\langle x \rangle$  is introduced as the unbiased estimator of the mean  $\mu_x$ . It is defined as

$$\langle x \rangle = \frac{\sum_{i=1}^N (\omega_x)_i x_i}{\sum_{i=1}^N (\omega_x)_i}, \quad (\text{D.5})$$

where the sample size is  $N$  and  $(\omega_x)_i$  is the weight attributed to the  $i$ th measurement  $x_i$ . The proof that it is unbiased goes as the following

$$\begin{aligned} E[\langle x \rangle] &= E \left[ \frac{\sum_{i=1}^N (\omega_x)_i x_i}{\sum_{i=1}^N (\omega_x)_i} \right] = \frac{E \left[ \sum_{i=1}^N (\omega_x)_i x_i \right]}{\sum_{i=1}^N (\omega_x)_i} \\ &= \frac{\sum_{i=1}^N (\omega_x)_i E[x_i]}{\sum_{i=1}^N (\omega_x)_i} = \frac{\sum_{i=1}^N (\omega_x)_i \mu_x}{\sum_{i=1}^N (\omega_x)_i} = \mu_x. \end{aligned} \quad (\text{D.6})$$

An unbiased estimator for the variance  $\sigma_x^2$  is given as [16]

$$s_x^2 = \left[ \frac{\sum_{i=1}^N (\omega_x)_i x_i^2}{\sum_{i=1}^N (\omega_x)_i} - \left( \frac{\sum_{i=1}^N (\omega_x)_i x_i}{\sum_{i=1}^N (\omega_x)_i} \right)^2 \right] \times \left[ \frac{1}{1 - \frac{\sum_{i=1}^N (\omega_x)_i^2}{(\sum_{i=1}^N (\omega_x)_i)^2}} \right]. \quad (\text{D.7})$$

The proof that this estimator is not biased is

$$\begin{aligned} E[s_x^2] &= E \left[ \frac{\sum_{i=1}^N (\omega_x)_i x_i^2}{\sum_{i=1}^N (\omega_x)_i} - \left( \frac{\sum_{i=1}^N (\omega_x)_i x_i}{\sum_{i=1}^N (\omega_x)_i} \right)^2 \right] \times \left[ \frac{1}{1 - \frac{\sum_{i=1}^N (\omega_x)_i^2}{(\sum_{i=1}^N (\omega_x)_i)^2}} \right] \\ &= \left[ \frac{\sum_{i=1}^N (\omega_x)_i E[x_i^2]}{\sum_{i=1}^N (\omega_x)_i} - \frac{E \left[ \sum_{i=1}^N (\omega_x)_i x_i \sum_{j=1}^N (\omega_x)_j x_j \right]}{\sum_{i=1}^N (\omega_x)_i \sum_{j=1}^N (\omega_x)_j} \right] \times \left[ \frac{1}{1 - \frac{\sum_{i=1}^N (\omega_x)_i^2}{(\sum_{i=1}^N (\omega_x)_i)^2}} \right] \\ &= \left[ E[x^2] - \frac{\sum_{i \neq j}^N (\omega_x)_i (\omega_x)_j E[x_i x_j] + \sum_{i=1}^N (\omega_x)_i^2 E[x_i^2]}{\sum_{i=1}^N (\omega_x)_i \sum_{j=1}^N (\omega_x)_j} \right] \times \left[ \frac{1}{1 - \frac{\sum_{i=1}^N (\omega_x)_i^2}{(\sum_{i=1}^N (\omega_x)_i)^2}} \right] \\ &= \left[ \frac{\sum_{i,j=1}^N (\omega_x)_i (\omega_x)_j E[x^2] - \sum_{i \neq j}^N (\omega_x)_i (\omega_x)_j E[x]^2 - \sum_{i=1}^N (\omega_x)_i^2 E[x^2]}{\sum_{i=1}^N (\omega_x)_i \sum_{j=1}^N (\omega_x)_j} \right] \times \left[ \frac{1}{1 - \frac{\sum_{i=1}^N (\omega_x)_i^2}{(\sum_{i=1}^N (\omega_x)_i)^2}} \right] \\ &= \left[ \frac{\sum_{i \neq j}^N (\omega_x)_i (\omega_x)_j (E[x^2] - E[x]^2)}{\sum_{i=1}^N (\omega_x)_i \sum_{j=1}^N (\omega_x)_j} \right] \times \left[ \frac{1}{1 - \frac{\sum_{i=1}^N (\omega_x)_i^2}{(\sum_{i=1}^N (\omega_x)_i)^2}} \right] \\ &= \sigma_x^2 \left[ \frac{\sum_{i \neq j}^N (\omega_x)_i (\omega_x)_j}{\sum_{i,j=1}^N (\omega_x)_i} \right] \times \left[ \frac{1}{1 - \frac{\sum_{i=1}^N (\omega_x)_i^2}{(\sum_{i=1}^N (\omega_x)_i)^2}} \right] \\ &= \sigma_x^2 \left[ 1 - \frac{\sum_{i=1}^N (\omega_x)_i^2}{(\sum_{i=1}^N (\omega_x)_i (\omega_x)_j)^2} \right] \times \left[ \frac{1}{1 - \frac{\sum_{i=1}^N (\omega_x)_i^2}{(\sum_{i=1}^N (\omega_x)_i)^2}} \right] \\ &= \sigma_x^2, \end{aligned} \quad (\text{D.8})$$

where  $E[x_i^2] = E[x^2]$ ,  $E[x_i x_j] = E[x_i]E[x_j] = \mu_x^2$  and the abbreviation  $\sum_{i=1}^N (\omega_x)_i \sum_{j=1}^N (\omega_y)_j = \sum_{i,j}^N (\omega_x)_i (\omega_y)_j$  was used

As the sample mean  $\langle x \rangle$  is the unbiased estimator of the mean  $\mu_x$ , its final error is reported as [16]

$$\langle x \rangle \pm \sqrt{V[\langle x \rangle]}, \quad (\text{D.9})$$

where  $V[\langle x \rangle]$  is the sample variance (also denoted by  $\sigma_{\langle x \rangle}^2$ ). This sample variance is given as

$$\sigma_{\langle x \rangle}^2 = V[\langle x \rangle] = \frac{\sum_{i=1}^N (\omega_x)_i^2}{\left(\sum_{i=1}^N (\omega_x)_i\right)^2} \sigma_x^2. \quad (\text{D.10})$$

The proof of the latter equation is

$$\begin{aligned} \sigma_{\langle x \rangle}^2 &= E[\langle x \rangle^2] - E[\langle x \rangle]^2 \\ &= E\left[\frac{\sum_{i=1}^N (\omega_x)_i x_i}{\sum_{i=1}^N (\omega_x)_i} \cdot \frac{\sum_{j=1}^N (\omega_x)_j x_j}{\sum_{j=1}^N (\omega_x)_j}\right] - \mu_x^2 \\ &= \frac{1}{\left(\sum_{i=1}^N (\omega_x)_i\right)^2} \left( E\left[\sum_{i,j=1}^N (\omega_x)_i (\omega_x)_j x_i x_j\right] - \sum_{i,j=1}^N (\omega_x)_i (\omega_x)_j \mu_x^2 \right) \\ &= \frac{1}{\left(\sum_{i=1}^N (\omega_x)_i\right)^2} \left( \sum_{i,j=1}^N (\omega_x)_i (\omega_x)_j E[x_i x_j] - \sum_{i,j=1}^N (\omega_x)_i (\omega_x)_j \mu_x^2 \right) \\ &= \frac{1}{\left(\sum_{i=1}^N (\omega_x)_i\right)^2} \left( \sum_{\substack{i,j=1 \\ i \neq j}}^N (\omega_x)_i (\omega_x)_j \mu_x^2 + \sum_{i=1}^N (\omega_x)_i (\omega_x)_i \mu_x^2 - \sum_{i,j=1}^N (\omega_x)_i (\omega_x)_j \mu_x^2 \right) \\ &= \frac{\sum_i (\omega_x)_i (\omega_x)_i}{\left(\sum_{i=1}^N (\omega_x)_i\right)^2} (\mu_x^2 - \mu_x^2) \\ &= \frac{\sum_i (\omega_x)_i^2}{\left(\sum_{i=1}^N (\omega_x)_i\right)^2} \cdot \sigma_x^2. \end{aligned} \quad (\text{D.11})$$

Thus, the estimate of the sample mean  $\langle x \rangle$  and its error are reported as [16]

$$\langle x \rangle \pm \sqrt{\frac{\sum_{i=1}^N (\omega_x)_i^2}{\left(\sum_{i=1}^N (\omega_x)_i\right)^2} s_x^2}, \quad (\text{D.12})$$

where the unbiased estimator  $s_x^2$  for the variance has been used. The term

$$s_{\langle x \rangle}^2 = \frac{\sum_{i=1}^N (\omega_x)_i^2}{\left(\sum_{i=1}^N (\omega_x)_i\right)^2} s_x^2 \quad (\text{D.13})$$

will be referred to as the unbiased estimator for the sample variance.

## D.2 General error propagation

Consider a function  $h(x, y)$  of two random variables  $x$  and  $y$  that follow a p.d.f.  $f(x, y)$ . Using leading order error propagation [100], the mean of  $h$ ,  $\mu_h$ , is given as

$$\mu_h = E[h(x, y)] \approx h(\mu_x, \mu_y). \quad (\text{D.14})$$

The corresponding, first order term of the variance  $\sigma_h^2$  is

$$\begin{aligned} \sigma_h^2 \approx & \left[ \left( \frac{\partial h}{\partial x} \right) \Big|_{x=\mu_x, y=\mu_y} \cdot \sigma_x \right]^2 + \left[ \left( \frac{\partial h}{\partial y} \right) \Big|_{x=\mu_x, y=\mu_y} \cdot \sigma_y \right]^2 \\ & + 2 \left( \frac{\partial h}{\partial x} \frac{\partial h}{\partial y} \right) \Big|_{x=\mu_x, y=\mu_y} V_{xy} \end{aligned} \quad (\text{D.15})$$

In the above equation,  $V_{xy}$  denotes the covariance between the two random variables  $x$  and  $y$ , and is defined as

$$V_{xy} = E[(x - \mu_x)(y - \mu_y)] = E[xy] - E[x]E[y]. \quad (\text{D.16})$$

An unbiased estimator of this covariance is given as [16]

$$Cov(x, y) = \frac{\frac{\sum_{i=1}^N (\omega_x)_i (\omega_y)_i x_i y_i}{\sum_{i=1}^N (\omega_x)_i (\omega_y)_i} - \frac{\sum_{i=1}^N (\omega_x)_i x_i}{\sum_{i=1}^N (\omega_x)_i} \frac{\sum_{j=1}^N (\omega_y)_j y_j}{\sum_{j=1}^N (\omega_y)_j}}{1 - \frac{\sum_{i=1}^N (\omega_x)_i (\omega_y)_i}{\sum_{i=1}^N (\omega_x)_i \sum_{j=1}^N (\omega_y)_j}}, \quad (\text{D.17})$$

where  $(\omega_x)_i$  and  $(\omega_y)_i$  are the weights for the  $i$ th measurement  $x_i$  and  $y_i$ , respectively. The proof that this estimator is unbiased is the generalisation of the proof for  $s_x^2$

$$\begin{aligned} E[Cov(x, y)] &= E \left[ \frac{\sum_{i=1}^N (\omega_x)_i (\omega_y)_i x_i y_i}{\sum_{i=1}^N (\omega_x)_i (\omega_y)_i} - \frac{\sum_{i=1}^N (\omega_x)_i x_i}{\sum_{i=1}^N (\omega_x)_i} \frac{\sum_{j=1}^N (\omega_y)_j y_j}{\sum_{j=1}^N (\omega_y)_j} \right] \times \left[ \frac{1}{1 - \frac{\sum_{i=1}^N (\omega_x)_i (\omega_y)_i}{\sum_{i=1}^N (\omega_x)_i \sum_{j=1}^N (\omega_y)_j}} \right] \\ &= \frac{\left[ \sum_{i,j=1}^N (\omega_x)_i (\omega_y)_j \mu_{xy} - \sum_{\substack{i,j=1 \\ i \neq j}}^N (\omega_x)_i (\omega_y)_j \mu_x \mu_y - \sum_{i=1}^N (\omega_x)_i (\omega_y)_i \mu_{xy} \right]}{\sum_{i,j=1}^N (\omega_x)_i (\omega_y)_j} \\ &\times \left[ \frac{1}{1 - \frac{\sum_{i=1}^N (\omega_x)_i (\omega_y)_i}{\sum_{i=1}^N (\omega_x)_i \sum_{j=1}^N (\omega_y)_j}} \right] \\ &= \frac{(\mu_{xy} - \mu_x \mu_y) \sum_{\substack{i,j=1 \\ i \neq j}}^N (\omega_x)_i (\omega_y)_j}{\sum_{i,j=1}^N (\omega_x)_i (\omega_y)_j} \times \left[ \frac{1}{1 - \frac{\sum_{i=1}^N (\omega_x)_i (\omega_y)_i}{\sum_{i=1}^N (\omega_x)_i \sum_{j=1}^N (\omega_y)_j}} \right] \\ &= V_{xy} \left[ 1 - \frac{\sum_{i=1}^N (\omega_x)_i (\omega_y)_i}{\sum_{i=1}^N (\omega_x)_i \sum_{j=1}^N (\omega_y)_j} \right] \times \left[ \frac{1}{1 - \frac{\sum_{i=1}^N (\omega_x)_i (\omega_y)_i}{\sum_{i=1}^N (\omega_x)_i \sum_{j=1}^N (\omega_y)_j}} \right] \\ &= V_{xy} \end{aligned} \quad (\text{D.18})$$

The final result on the measurement of  $h$  is reported as  $\langle h \rangle$ , and it is to leading order given as

$$\langle h \rangle \approx h(\langle x \rangle, \langle y \rangle) \quad (\text{D.19})$$

The error on this measurement is given according to [16] as

$$\sigma_{\langle h \rangle}^2 \approx \left[ \left( \frac{\partial h}{\partial x} \right) \Big|_{x=\mu_x, y=\mu_y} \cdot \sigma_{\langle x \rangle} \right]^2 + \left[ \left( \frac{\partial h}{\partial y} \right) \Big|_{x=\mu_x, y=\mu_y} \cdot \sigma_{\langle y \rangle} \right]^2 + 2 \left( \frac{\partial h}{\partial x} \frac{\partial h}{\partial y} \right) \Big|_{x=\mu_x, y=\mu_y} V_{\langle x \rangle \langle y \rangle}, \quad (\text{D.20})$$

where  $\sigma_{\langle x \rangle}$  and  $\sigma_{\langle y \rangle}$  are the variances of the sample means  $\langle x \rangle$  and  $\langle y \rangle$ , respectively. In the above equation,  $V_{\langle x \rangle \langle y \rangle}$  is used to denote the sample covariance, which can be obtained as

$$V_{\langle x \rangle \langle y \rangle} = \frac{\sum_{i=1}^N (\omega_x)_i (\omega_y)_i}{\sum_{i=1}^N (\omega_x)_i \sum_{j=1}^N (\omega_y)_j} V_{xy}. \quad (\text{D.21})$$

The later equality can be proven as

$$\begin{aligned} V_{\langle x \rangle \langle y \rangle} &= E[\langle x \rangle \langle y \rangle] - E[\langle x \rangle] E[\langle y \rangle] \\ &= E \left[ \frac{\sum_{i=1}^N (\omega_x)_i x_i}{\sum_{i=1}^N (\omega_x)_i} \cdot \frac{\sum_{j=1}^N (\omega_y)_j y_j}{\sum_{j=1}^N (\omega_y)_j} \right] - \mu_x \mu_y \\ &= \frac{1}{\sum_{i=1}^N (\omega_x)_i \sum_{j=1}^N (\omega_y)_j} \left( E \left[ \sum_{i,j}^N (\omega_x)_i (\omega_y)_j x_i y_j \right] - \sum_{i,j}^N (\omega_x)_i (\omega_y)_j \mu_x \mu_y \right) \\ &= \frac{1}{\sum_{i=1}^N (\omega_x)_i \sum_{j=1}^N (\omega_y)_j} \left( \sum_{i,j}^N (\omega_x)_i (\omega_y)_j E[x_i y_j] - \sum_{i,j}^N (\omega_x)_i (\omega_y)_j \mu_x \mu_y \right) \\ &= \frac{1}{\sum_{i=1}^N (\omega_x)_i \sum_{j=1}^N (\omega_y)_j} \left( \sum_{\substack{i,j \\ i \neq j}}^N (\omega_x)_i (\omega_y)_j \mu_x \mu_y + \sum_i^N (\omega_x)_i (\omega_y)_i \mu_{xy} - \sum_{i,j}^N (\omega_x)_i (\omega_y)_j \mu_x \mu_y \right) \\ &= \frac{\sum_i^N (\omega_x)_i (\omega_y)_i}{\sum_{i=1}^N (\omega_x)_i \sum_{j=1}^N (\omega_y)_j} (\mu_{xy} - \mu_x \mu_y) \\ &= \frac{\sum_i^N (\omega_x)_i (\omega_y)_i}{\sum_{i=1}^N (\omega_x)_i \sum_{j=1}^N (\omega_y)_j} V_{xy}, \end{aligned} \quad (\text{D.22})$$

where the abbreviation  $\sum_{i=1}^N (\omega_x)_i \sum_{j=1}^N (\omega_y)_j = \sum_{i,j}^N (\omega_x)_i (\omega_y)_j$  has been used. Using the unbiased estimator for the covariance  $V_{xy}$ , one thus obtains the unbiased estimator for the sample covariance  $Cov(\langle x \rangle \langle y \rangle)$  as

$$Cov(\langle x \rangle \langle y \rangle) = \frac{\sum_{i=1}^N (\omega_x)_i (\omega_y)_i}{\sum_{i=1}^N (\omega_x)_i \sum_{j=1}^N (\omega_y)_j} Cov(xy). \quad (\text{D.23})$$

With this, one reports the estimate on the error of  $\langle h \rangle$  as

$$\begin{aligned} s_{\langle h \rangle}^2 &\approx \left[ \left( \frac{\partial h}{\partial x} \right) \Big|_{x=\langle x \rangle, y=\langle y \rangle} \cdot s_{\langle x \rangle} \right]^2 + \left[ \left( \frac{\partial h}{\partial y} \right) \Big|_{x=\langle x \rangle, y=\langle y \rangle} \cdot s_{\langle y \rangle} \right]^2 \\ &\quad + 2 \left( \frac{\partial h}{\partial x} \frac{\partial h}{\partial y} \right) \Big|_{x=\langle x \rangle, y=\langle y \rangle} Cov\langle x \rangle \langle y \rangle, \end{aligned} \quad (\text{D.24})$$

where the unbiased estimators for the sample variances  $s_{\langle x \rangle}^2$  and  $s_{\langle y \rangle}^2$  have been used.

### D.3 SPC specific error propagation

Using the previously defined estimators for the sample variance and covariance, this section presents the final error propagation on the measurement for the Gaussian Estimator. For this purpose, the final SPC is written as

$$SPC = \sqrt{\frac{\pi}{4} \frac{\langle N \rangle}{\sqrt{\langle D \rangle}}}, \quad (\text{D.25})$$

where  $\langle N \rangle$  and  $\langle D \rangle$  are the measured unbiased estimators for the observables in the numerator and denominator, respectively. Thus, the partial derivatives are obtained as

$$\left( \frac{\partial SPC}{\partial N} \right) \Big|_{N=\langle N \rangle, D=\langle D \rangle} = \sqrt{\frac{\pi}{4}} \frac{1}{\sqrt{\langle D \rangle}} = \frac{SPC}{\langle N \rangle}, \quad (\text{D.26})$$

$$\left( \frac{\partial SPC}{\partial D} \right) \Big|_{N=\langle N \rangle, D=\langle D \rangle} = -\frac{1}{2} \sqrt{\frac{\pi}{4}} \frac{1}{\sqrt{\langle D \rangle}^3} = -\frac{1}{2} \frac{SPC}{\langle N \rangle}. \quad (\text{D.27})$$

Using the unbiased estimates for the sample variance on the numerator and denominator  $s_{\langle N \rangle}$  and  $s_{\langle D \rangle}$  as well as the estimate for the sample covariance between numerator and denominator  $Cov(\langle N \rangle \langle D \rangle)$ , one obtains for the estimate of the variance on the SPC  $s_{SPC}^2$

$$s_{SPC}^2 = \left( \frac{SPC}{\langle N \rangle} \cdot s_{\langle N \rangle} \right)^2 + \left( \frac{1}{2} \frac{SPC}{\langle D \rangle} \cdot s_{\langle D \rangle} \right)^2 - \frac{1}{2} \frac{SPC^2}{\langle N \rangle \langle D \rangle} Cov(\langle N \rangle \langle D \rangle). \quad (\text{D.28})$$

# Appendix E

## Supplements data analysis

### E.1 Run-by-run trending

Figure E.1 shows an example of run-by-run trending of the multiparticle correlators used in the GE for the SPC  $\langle \cos [6(\Psi_6 - \Psi_3)] \rangle$ , while Fig E.2 shows the average multiplicity and the number of events. Both figures are a trending for the 0-5 % centrality range. Based on this run-by-run trending, four runs with extremely low amount of events have been excluded, leading to an improvement of the stability of the statistical uncertainties.

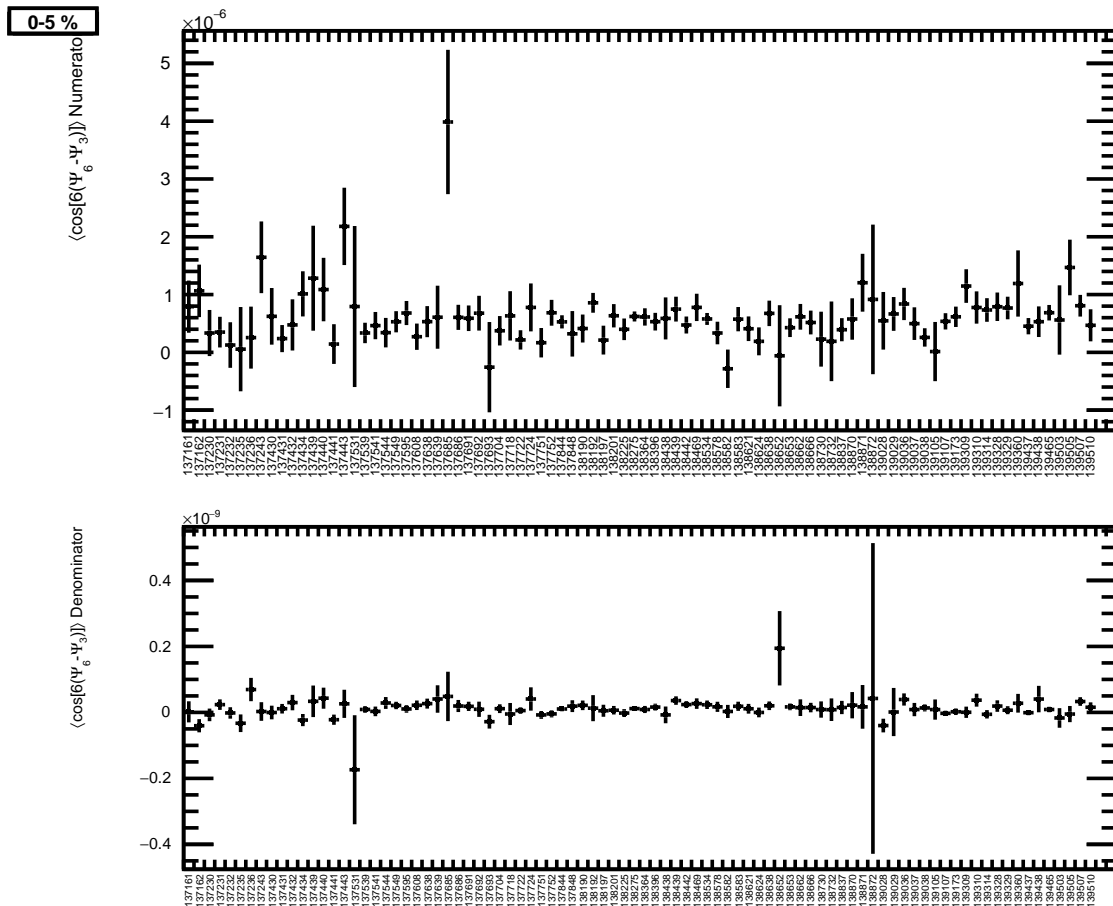


Figure E.1: Example of run-by-run trending of the multiparticle correlators of numerator and denominator of  $\langle \cos [6(\Psi_6 - \Psi_3)] \rangle$  for the centrality 0–5 %.

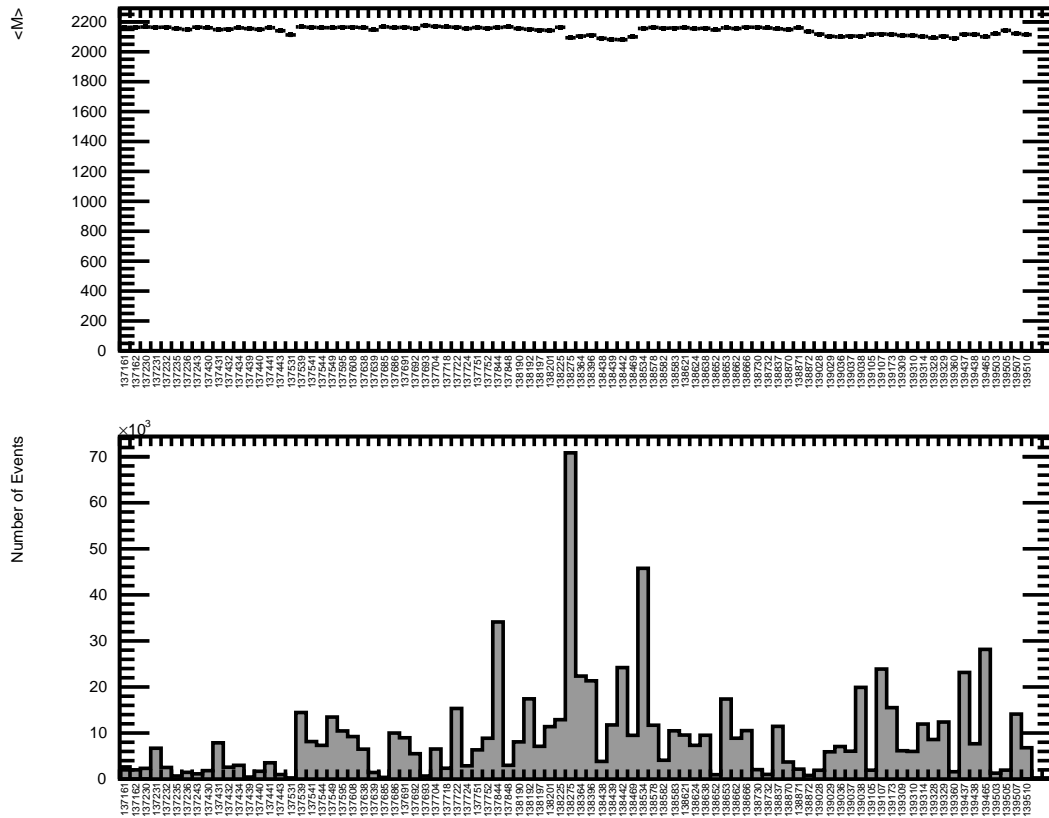


Figure E.2: Example of run-by-run trending of the average multiplicity and the amount of events for the centrality 0–5 %.

## E.2 Comparison of statistical errors

In this section, the comparisons between the classical and alternative approaches for the covariance term in the error propagation are provided for the remaining SPC (see Sec. 6.6). The results for SPC between two planes are presented in Fig. E.3 and Fig. E.4, between three planes in Figs. E.5-E.7 and between four planes in Fig. E.8. The results show that the deviation between the two approaches is usually at most around 5%, while the maximum of deviation is found especially in the region where the error to signal ratio is extremely small. This study could not be performed for the SPC  $\langle \cos[6(\Psi_2 - \Psi_3)] \rangle$  as the order of the multiparticle correlator for the alternative approach is too large.

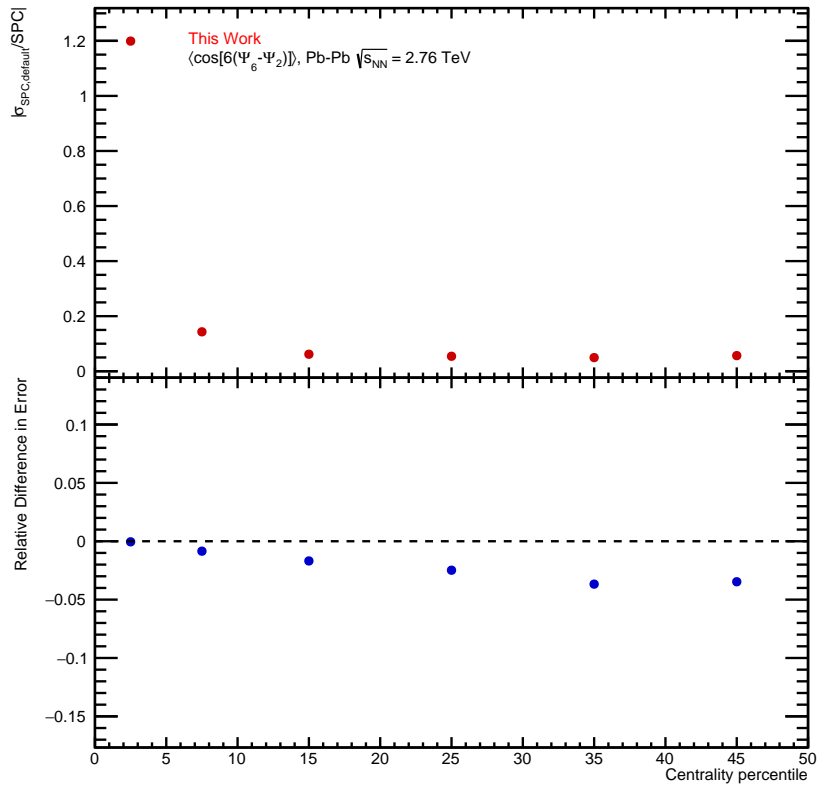


Figure E.3: Comparison between classical and alternative approach in error propagation for  $\langle \cos[6(\Psi_6 - \Psi_2)] \rangle$ .

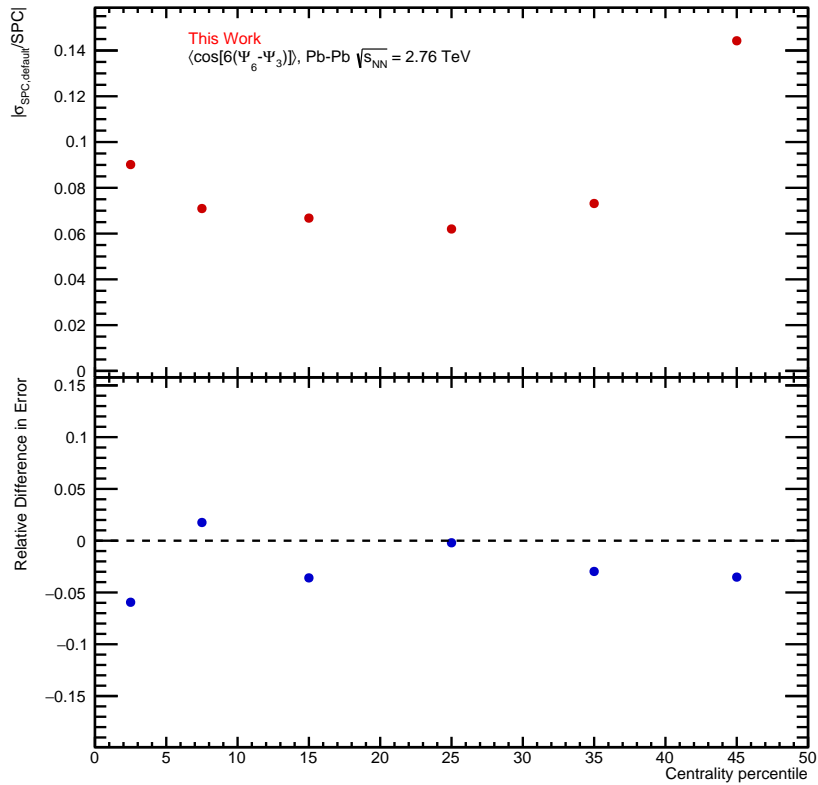


Figure E.4: Comparison between classical and alternative approach in error propagation for  $\langle \cos[6(\Psi_2 - \Psi_3)] \rangle$ .

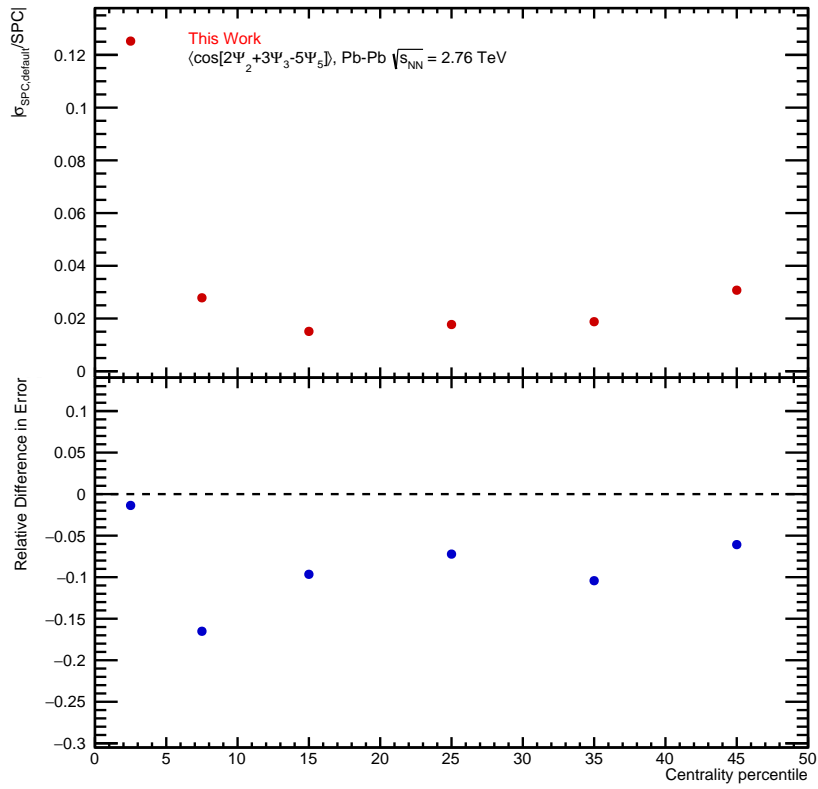


Figure E.5: Comparison between classical and alternative approach in error propagation for  $\langle \cos[2\Psi_2 + 3\Psi_3 - 5\Psi_5] \rangle$ .

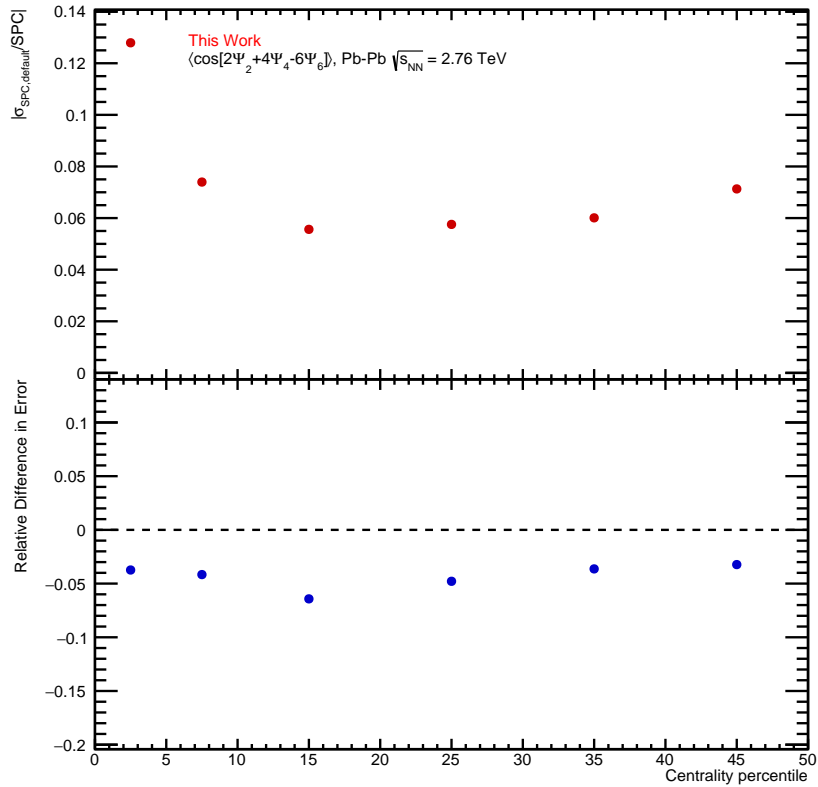


Figure E.6: Comparison between classical and alternative approach in error propagation for  $\langle \cos[2\Psi_2 + 4\Psi_4 - 6\Psi_6] \rangle$ .

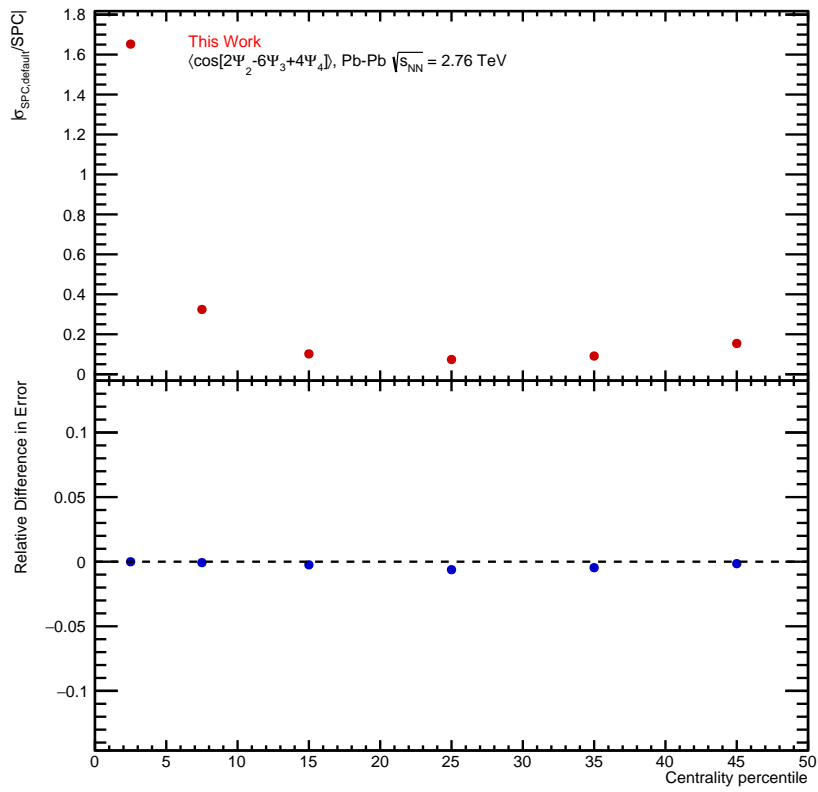


Figure E.7: Comparison between classical and alternative approach in error propagation for  $\langle \cos[2\Psi_2 - 6\Psi_3 + 4\Psi_4] \rangle$ .

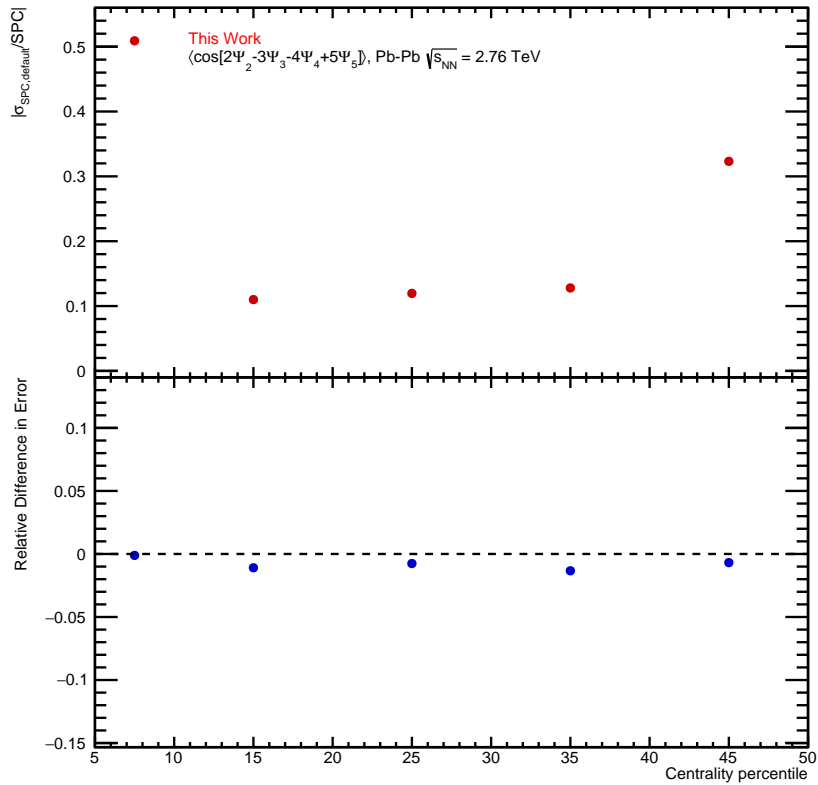


Figure E.8: Comparison between classical and alternative approach in error propagation for  $\langle \cos[2\Psi_2 - 3\Psi_3 - 4\Psi_4 + 5\Psi_5] \rangle$ .

### E.3 Systematic Errors

In this section, the results of the systematic errors for the measured SPC are provided. The results for the SPC between two planes are summarized in Tab. E.1 and E.2 and shown in Fig. E.9-E.11. Similarly, the results for three planes are presented in Tab. E.3 and Tab. E.4 as well as in the Figs. E.12-E.15. Table E.5 and Fig. E.16 present the results concerning the systematic errors measured for the SPC between four planes. An em-dash “—” in the tables shows that a systematic trial was found to be statistically insignificant, i.e. its corresponding  $\sigma_{Barlow}$  is below two, indicated by the horizontal line in the corresponding figures.

Table E.1: Summary of the statistically significant relative variations (absolute values) per systematic trial and the total relative variation for  $\langle \cos [4 (\Psi_4 - \Psi_2)] \rangle$  and  $\langle \cos [6 (\Psi_2 - \Psi_3)] \rangle$ .

Systematic Variation	SPC	
	$\langle \cos [4 (\Psi_4 - \Psi_2)] \rangle$	$\langle \cos [6 (\Psi_2 - \Psi_3)] \rangle$
V0M	0.058	—
$PV_z < 8$ cm	0.003	—
$PV_z < 6$ cm	0.007	—
$DCA_{xy} < 1$ cm	0.018	—
$DCA_z < 2$ cm	0.008	—
$0.3 < \chi^2/N_{TPC} < 4.0$	0.001	0.442
$0.1 < \chi^2/N_{TPC} < 3.5$	0.001	0.545
$N_{TPC} > 80$	0.013	0.333
$N_{TPC} > 90$	0.031	0.372
$N_{TPC} > 100$	0.005	—
Magnetic ++	0.012	1.025
Magnetic --	0.086	1.120
Total Rel. Var.	0.111	1.373
Figure	6.24	E.9

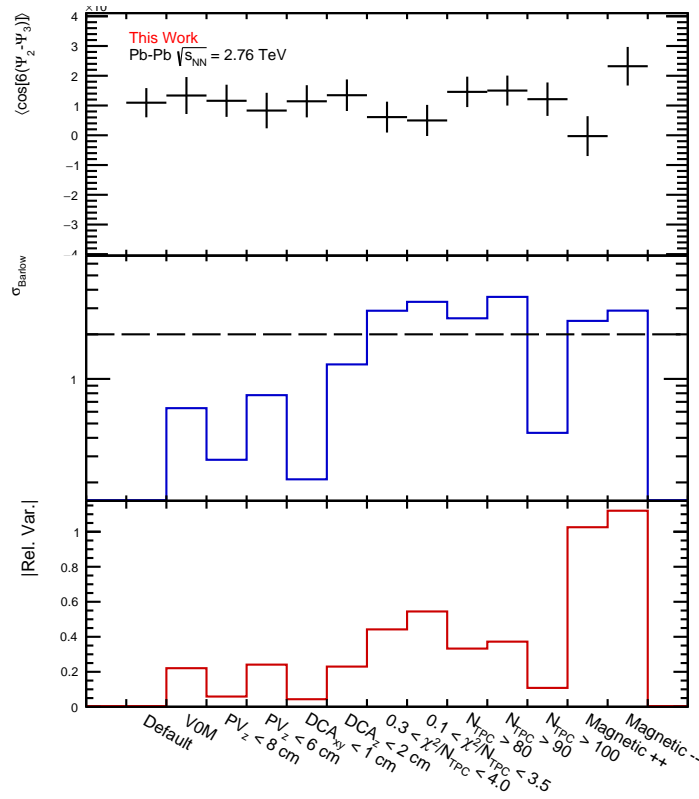


Figure E.9: Results for  $\sigma_{Barlow}$  and the relative variation (absolute values) of the systematic trials for  $\langle \cos [6 (\Psi_2 - \Psi_3)] \rangle$ .

Table E.2: Summary of the statistically significant relative variations (absolute values) per systematic trial and the total relative variation for  $\langle \cos [6 (\Psi_6 - \Psi_2)] \rangle$  and  $\langle \cos [6 (\Psi_6 - \Psi_3)] \rangle$ .

Systematic Variation	SPC	
	$\langle \cos [6 (\Psi_6 - \Psi_2)] \rangle$	$\langle \cos [6 (\Psi_6 - \Psi_3)] \rangle$
V0M	0.194	0.068
$PV_z < 8 \text{ cm}$	0.045	—
$PV_z < 6 \text{ cm}$	0.052	—
$DCA_{xy} < 1 \text{ cm}$	0.030	0.063
$DCA_z < 2 \text{ cm}$	—	—
$0.3 < \chi^2/N_{TPC} < 4.0$	0.038	—
$0.1 < \chi^2/N_{TPC} < 3.5$	0.047	—
$N_{TPC} > 80$	—	—
$N_{TPC} > 90$	0.008	0.011
$N_{TPC} > 100$	0.016	—
Magnetic ++	0.049	—
Magnetic --	0.137	—
Total Rel. Var.	0.252	0.093
Figure	E.10	E.11

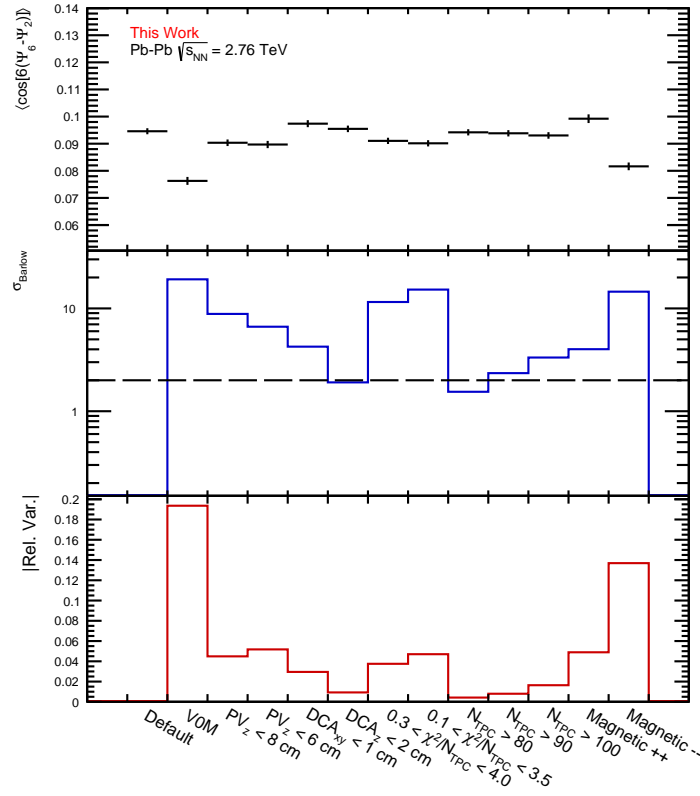


Figure E.10: Results for  $\sigma_{Barlow}$  and the relative variation (absolute values) of the systematic trials for  $\langle \cos[\delta(\Psi_6 - \Psi_2)] \rangle$ .

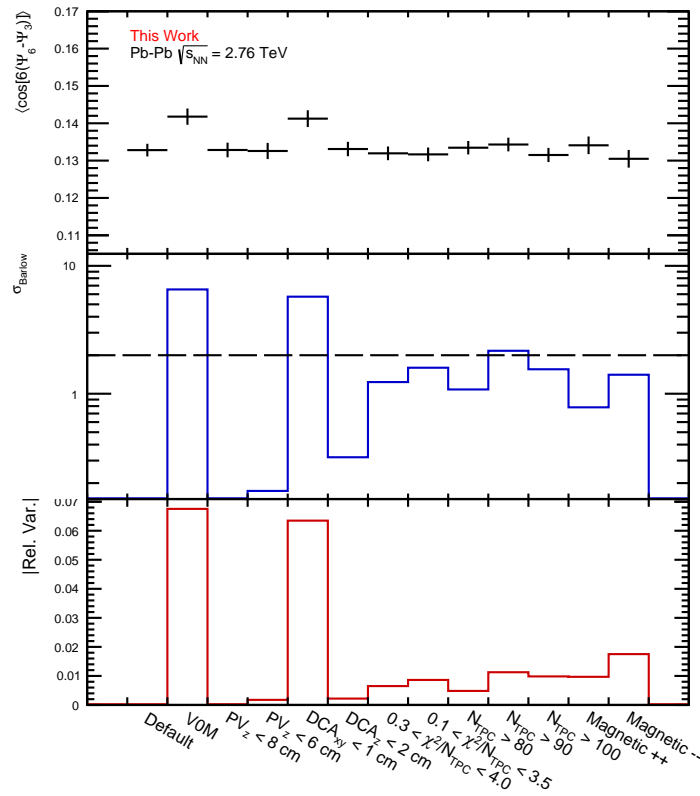


Figure E.11: Results for  $\sigma_{Barlow}$  and the relative variation (absolute values) of the systematic trials for  $\langle \cos[\delta(\Psi_6 - \Psi_3)] \rangle$ .

Table E.3: Summary of the statistically significant relative variations (absolute values) per systematic trial and the total relative variation for  $\langle \cos [2\Psi_2 + 3\Psi_3 - 5\Psi_5] \rangle$  and  $\langle \cos [8\Psi_2 - 3\Psi_3 - 5\Psi_5] \rangle$ .

Systematic Variation	SPC	
	$\langle \cos [2\Psi_2 + 3\Psi_3 - 5\Psi_5] \rangle$	$\langle \cos [8\Psi_2 - 3\Psi_3 - 5\Psi_5] \rangle$
V0M	0.012	—
$PV_z < 8$ cm	0.019	—
$PV_z < 6$ cm	0.022	—
$DCA_{xy} < 1$ cm	0.054	0.422
$DCA_z < 2$ cm	0.030	—
$0.3 < \chi^2/N_{TPC} < 4.0$	—	0.407
$0.1 < \chi^2/N_{TPC} < 3.5$	0.004	—
$N_{TPC} > 80$	—	—
$N_{TPC} > 90$	0.010	—
$N_{TPC} > 100$	0.033	—
Magnetic ++	0.009	0.962
Magnetic --	—	1.206
Total Rel. Var.	0.075	1.341
Figure	E.12	E.13

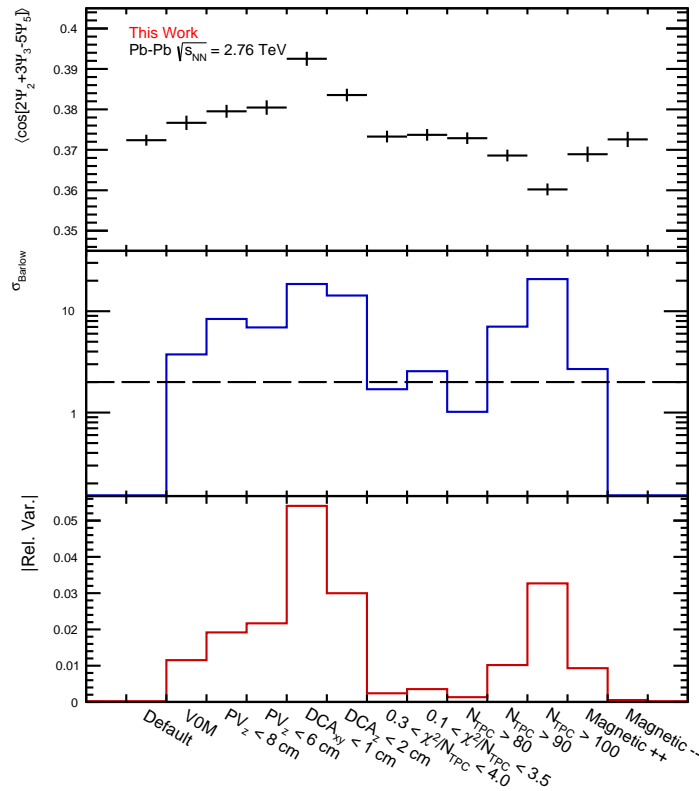


Figure E.12: Results for  $\sigma_{Barlow}$  and the relative variation (absolute values) of the systematic trials for  $\langle \cos [2\Psi_2 + 3\Psi_3 - 5\Psi_5] \rangle$ .

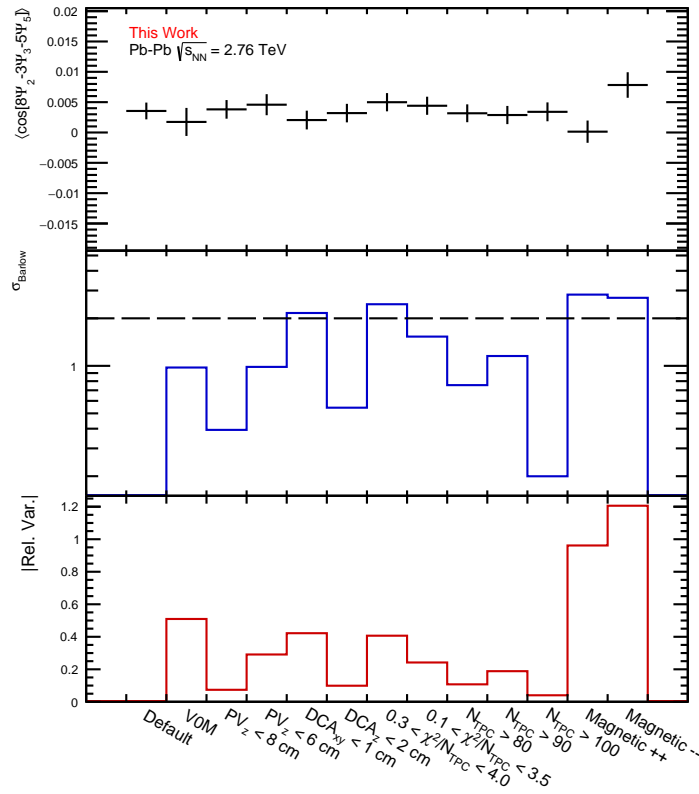


Figure E.13: Results for  $\sigma_{\text{Barlow}}$  and the relative variation (absolute values) of the systematic trials for  $\langle \cos [8\Psi_2 - 3\Psi_3 - 5\Psi_5] \rangle$ .

Table E.4: Summary of the statistically significant relative variations (absolute values) per systematic trial and the total relative variation for  $\langle \cos [2\Psi_2 - 6\Psi_3 + 4\Psi_4] \rangle$  and  $\langle \cos [2\Psi_2 + 4\Psi_4 - 6\Psi_6] \rangle$ .

Systematic Variation	SPC	
	$\langle \cos [2\Psi_2 - 6\Psi_3 + 4\Psi_4] \rangle$	$\langle \cos [2\Psi_2 + 4\Psi_4 - 6\Psi_6] \rangle$
V0M	0.064	—
$PV_z < 8 \text{ cm}$	—	0.018
$PV_z < 6 \text{ cm}$	0.056	—
$DCA_{xy} < 1 \text{ cm}$	0.030	0.076
$DCA_z < 2 \text{ cm}$	0.019	0.054
$0.3 < \chi^2/N_{TPC} < 4.0$	—	0.020
$0.1 < \chi^2/N_{TPC} < 3.5$	0.019	0.015
$N_{TPC} > 80$	0.029	0.011
$N_{TPC} > 90$	0.079	—
$N_{TPC} > 100$	—	0.026
Magnetic ++	0.051	—
Magnetic --	0.161	—
Total Rel. Var.	0.202	0.102
Figure	E.14	E.15

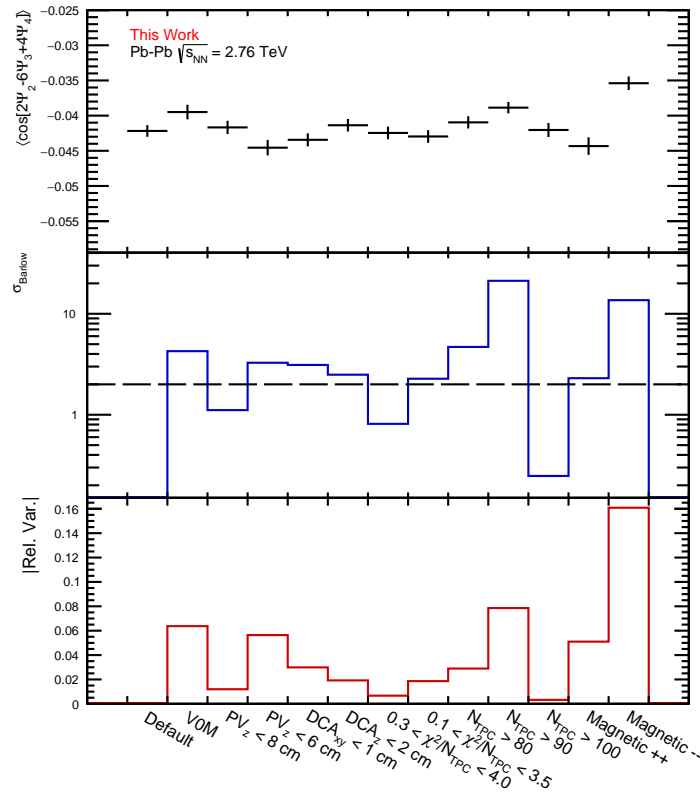


Figure E.14: Results for  $\sigma_{Barlow}$  and the relative variation (absolute values) of the systematic trials for  $\langle \cos[2\Psi_2 - 6\Psi_3 + 4\Psi_4] \rangle$ .

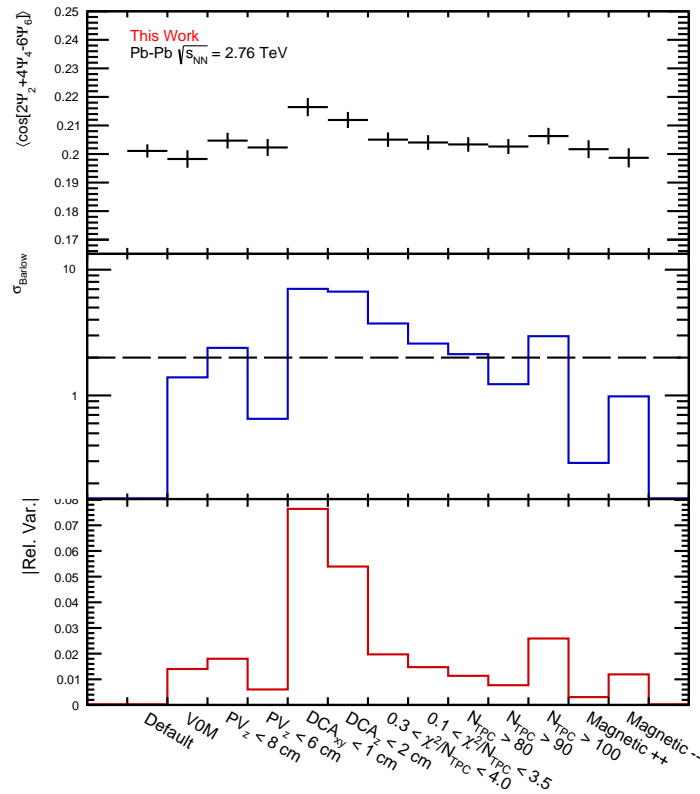


Figure E.15: Results for  $\sigma_{Barlow}$  and the relative variation (absolute values) of the systematic trials for  $\langle \cos[2\Psi_2 + 4\Psi_4 - 6\Psi_6] \rangle$ .

Table E.5: Summary of the statistically significant relative variations (absolute values) per systematic trial and the total relative variation for  $\langle \cos [2\Psi_2 - 3\Psi_3 - 4\Psi_4 + 5\Psi_5] \rangle$ .

Systematic Variation	SPC
	$\langle \cos [2\Psi_2 - 3\Psi_3 - 4\Psi_4 + 5\Psi_5] \rangle$
V0M	0.084
$PV_z < 8$ cm	—
$PV_z < 6$ cm	—
$DCA_{xy} < 1$ cm	0.091
$DCA_z < 2$ cm	—
$0.3 < \chi^2/N_{TPC} < 4.0$	0.025
$0.1 < \chi^2/N_{TPC} < 3.5$	0.013
$N_{TPC} > 80$	—
$N_{TPC} > 90$	0.040
$N_{TPC} > 100$	—
Magnetic ++	—
Magnetic --	—
Total Rel. Var.	0.133
Figure	E.16

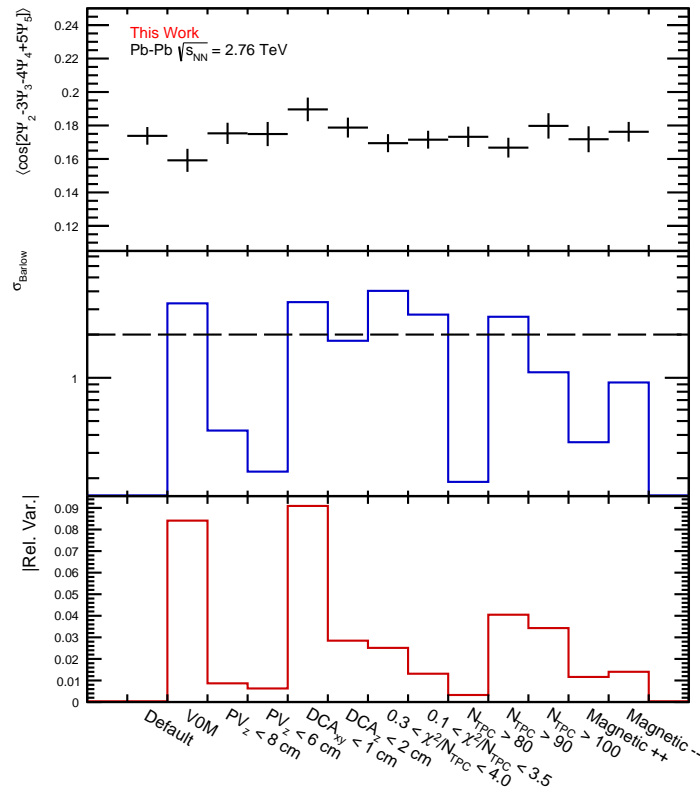


Figure E.16: Results for  $\sigma_{Barlow}$  and the relative variation (absolute values) of the systematic trials for  $\langle \cos [2\Psi_2 - 3\Psi_3 - 4\Psi_4 + 5\Psi_5] \rangle$ .

# Appendix F

## Supplements experimental results

### F.1 Comparison between ALICE and ATLAS data

In this section, the comparisons between the ALICE results using the GE and the ATLAS results [67] using the SP method are provided. Figures F.1-F.3 present the results for correlations between two symmetry planes, while Figs. F.4-F.7 are for correlations between three planes. Overall it can be seen that, especially in case of strongly correlated symmetry planes (i.e. non-zero values), the results from the GE lead to far smaller values than those reported by the ATLAS Collaboration using the SP method. This observation is in agreement with the observed difference between GE and SP method in the Glauber and iEBE-VISHNU model (see Sec. 5.1.3).

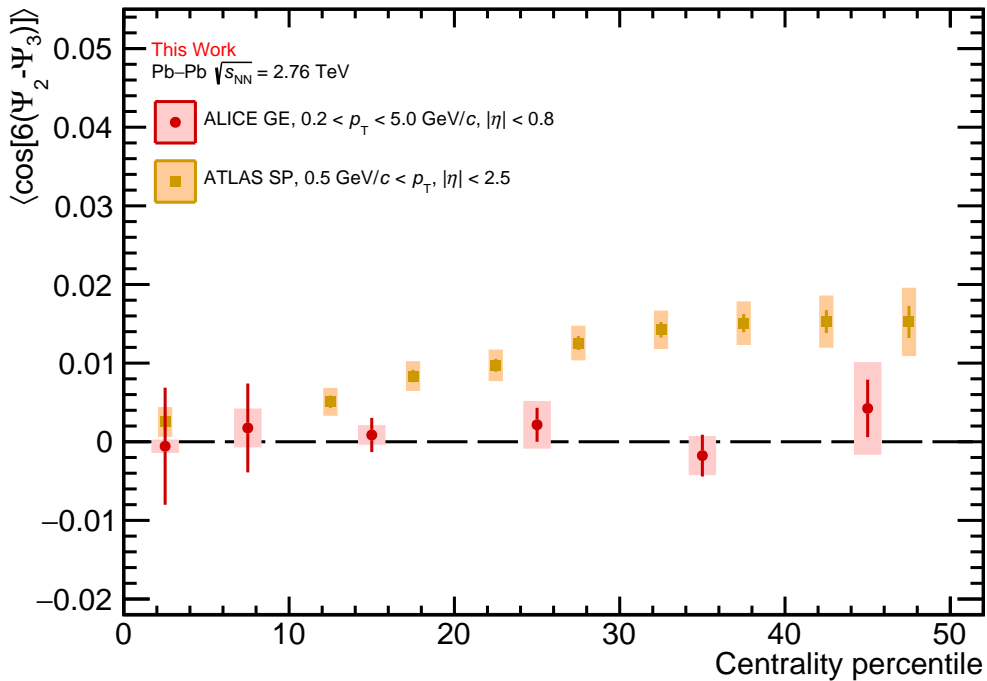


Figure F.1: Comparison of the measured ALICE data of  $\langle \cos[6(\Psi_2 - \Psi_3)] \rangle$  as function of centrality using the GE to the ATLAS results [67] using the SP method.

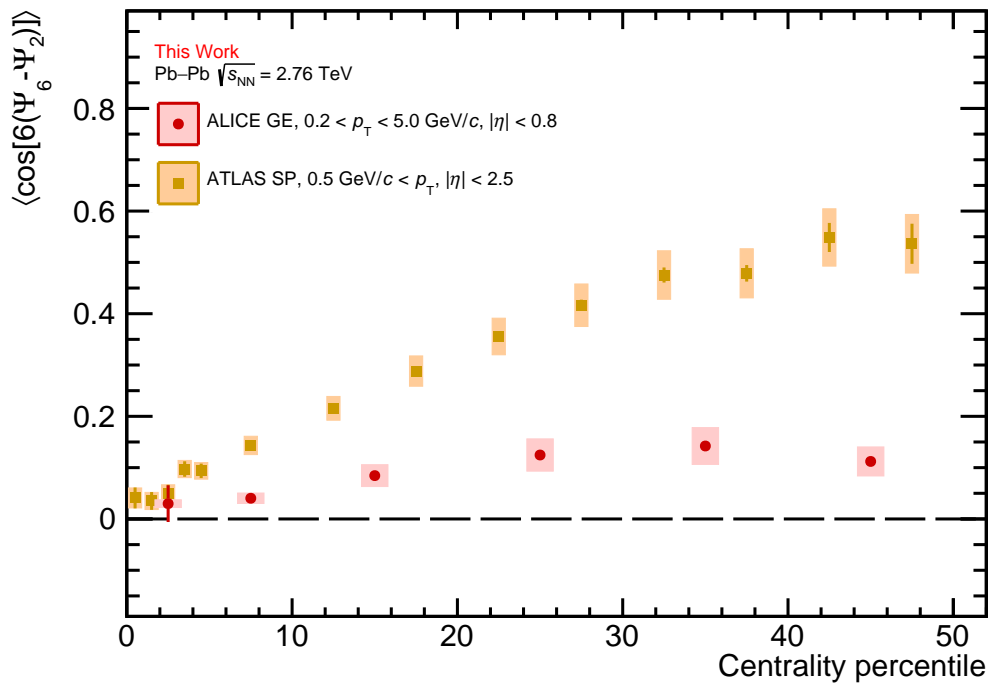


Figure F.2: Comparison of the measured ALICE data of  $\langle \cos[6(\Psi_6 - \Psi_2)] \rangle$  as function of centrality using the GE to the ATLAS results [67] using the SP method.

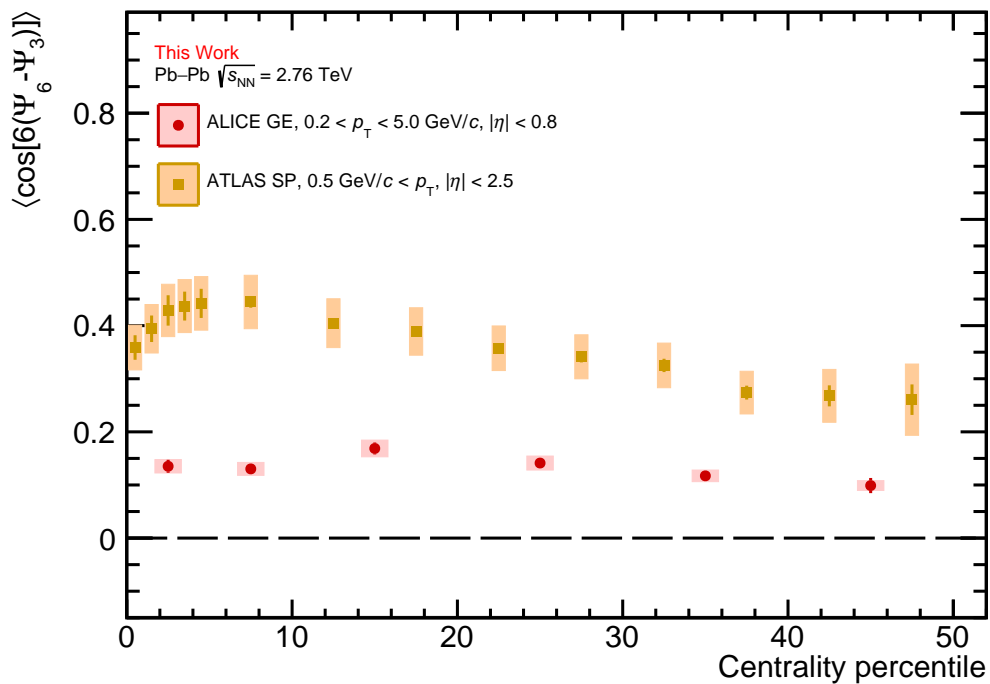


Figure F.3: Comparison of the measured ALICE data of  $\langle \cos[6(\Psi_6 - \Psi_3)] \rangle$  as function of centrality using the GE to the ATLAS results [67] using the SP method.

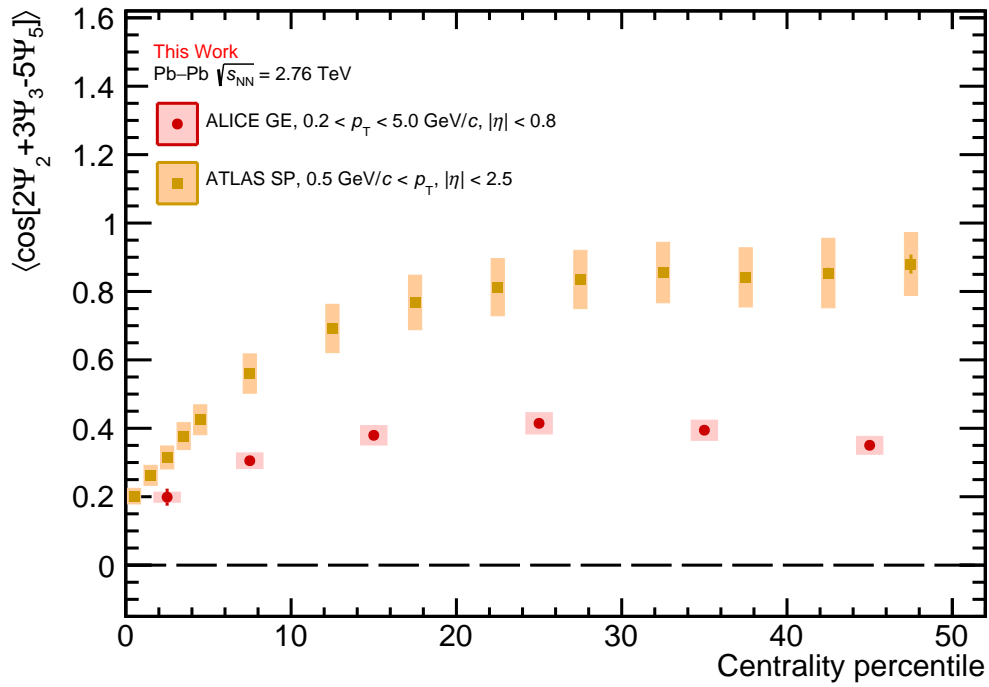


Figure F.4: Comparison of the measured ALICE data of  $\langle \cos[2\Psi_2 + 3\Psi_3 - 5\Psi_5] \rangle$  as function of centrality using the GE to the ATLAS results [67] using the SP method.

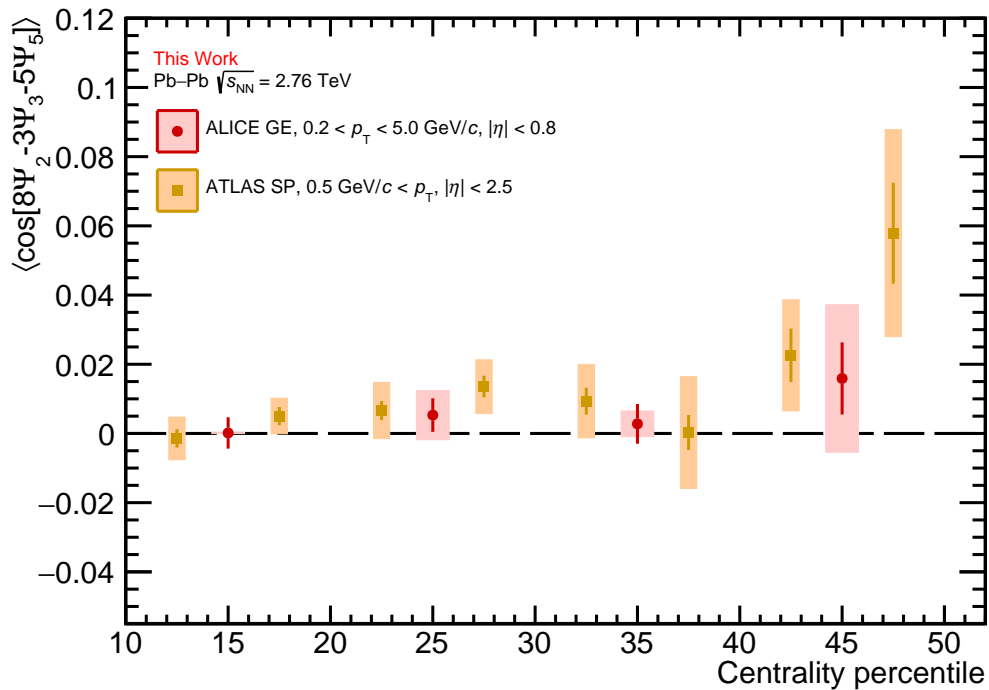


Figure F.5: Comparison of the measured ALICE data of  $\langle \cos[8\Psi_2 - 3\Psi_3 - 5\Psi_5] \rangle$  as function of centrality using the GE to the ATLAS results [67] using the SP method.

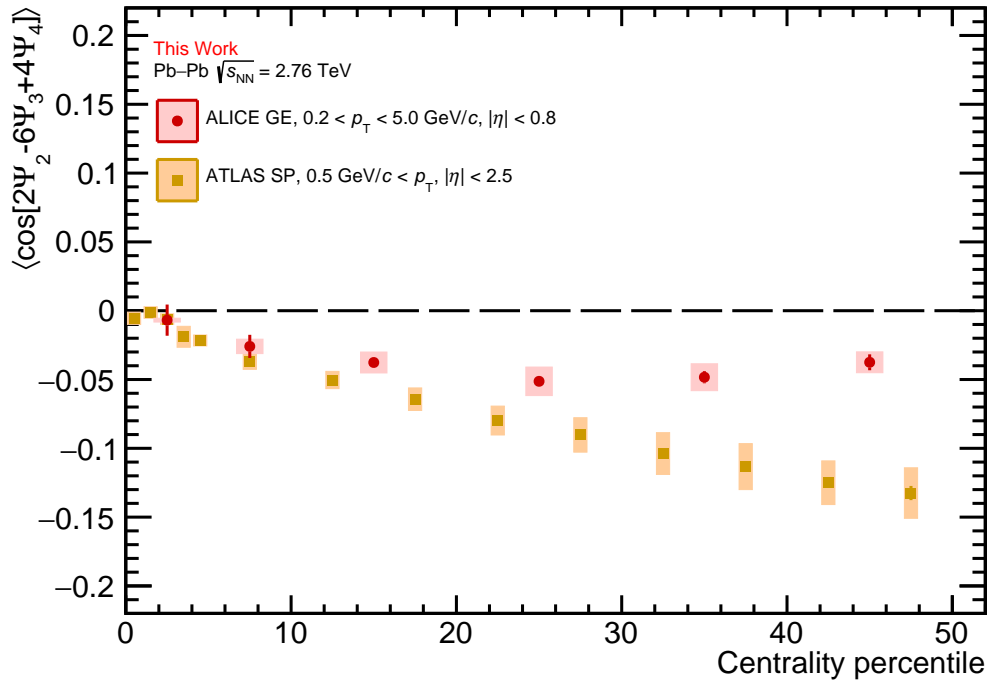


Figure F.6: Comparison of the measured ALICE data of  $\langle \cos[2\Psi_2 - 6\Psi_3 + 4\Psi_4] \rangle$  as function of centrality using the GE to the ATLAS results [67] using the SP method.

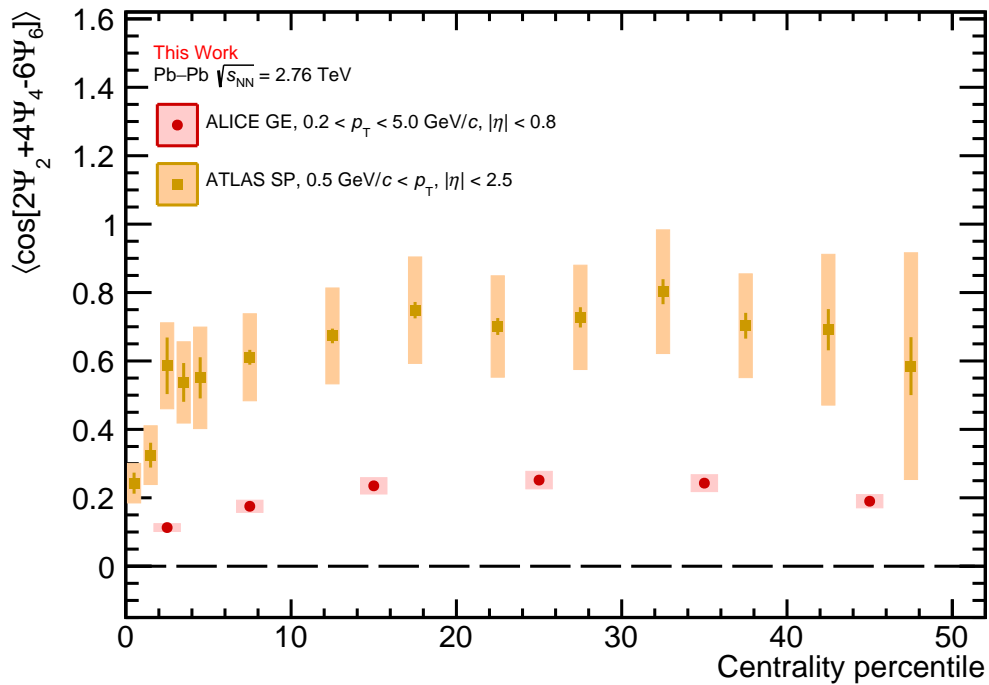


Figure F.7: Comparison of the measured ALICE data of  $\langle \cos[2\Psi_2 + 4\Psi_4 - 6\Psi_6] \rangle$  as function of centrality using the GE to the ATLAS results [67] using the SP method.

# Bibliography

- [1] David Griffiths, *Introduction to Elementary Particles (Second, Revised Edition)*. WILEY-VCH, 2008.  
Cited on pages 1 and 2.
- [2] A. Purcell, “Go on a particle quest at the first CERN webfest. Le premier webfest du CERN se lance à la conquête des particules,”  
<https://cds.cern.ch/record/1473657>.  
Cited on page 1.
- [3] S. Chatrchyan, V. Khachatryan, A. Sirunyan, A. Tumasyan, W. Adam, E. Aguilo, T. Bergauer, M. Dragicevic, J. Erö, C. Fabjan, and et al. (CMS Collaboration), “Observation of a new boson at a mass of 125 GeV with the CMS experiment at the LHC,” *Physics Letters B* **716** no. 1, (Sep, 2012) 30–61.  
<http://dx.doi.org/10.1016/j.physletb.2012.08.021>.  
Cited on page 2.
- [4] G. Aad, T. Abajyan, B. Abbott, J. Abdallah, S. Abdel Khalek, A. Abdelalim, O. Abdinov, R. Aben, B. Abi, M. Abolins, and et al. (ATLAS Collaboration), “Observation of a new particle in the search for the Standard Model Higgs boson with the ATLAS detector at the LHC,” *Physics Letters B* **716** no. 1, (Sep, 2012) 1–29. <http://dx.doi.org/10.1016/j.physletb.2012.08.020>.  
Cited on page 2.
- [5] F. Englert and R. Brout, “Broken Symmetry and the Mass of Gauge Vector Mesons,” *Phys. Rev. Lett.* **13** (Aug, 1964) 321–323.  
<https://link.aps.org/doi/10.1103/PhysRevLett.13.321>.  
Cited on page 2.
- [6] P. Higgs, “Broken symmetries, massless particles and gauge fields,” *Physics Letters* **12** no. 2, (1964) 132–133.  
<https://www.sciencedirect.com/science/article/pii/0031916364911369>.  
Cited on page 2.
- [7] P. W. Higgs, “Broken Symmetries and the Masses of Gauge Bosons,” *Phys. Rev. Lett.* **13** (Oct, 1964) 508–509.  
<https://link.aps.org/doi/10.1103/PhysRevLett.13.508>.  
Cited on page 2.
- [8] G. S. Guralnik, C. R. Hagen, and T. W. B. Kibble, “Global Conservation Laws and Massless Particles,” *Phys. Rev. Lett.* **13** (Nov, 1964) 585–587.  
<https://link.aps.org/doi/10.1103/PhysRevLett.13.585>.  
Cited on page 2.

- [9] E. Corbelli and P. Salucci, “The Extended Rotation Curve and the Dark Matter Halo of M33,” *Mon. Not. Roy. Astron. Soc.* **311** (2000) 441–447, arXiv:astro-ph/9909252.  
Cited on page 2.
- [10] V. A. et al. (D0 Collaboration and T. Collaboration), “Comparison of  $pp$  and  $p\bar{p}$  differential elastic cross sections and observation of the exchange of a colorless  $C$ -odd gluonic compound,” 2021.  
Cited on page 2.
- [11] N. B. Łukaszuk, L., “A possible interpretation of  $pp$  rising total cross-sections,” *Lett. Nuovo Cimento* **8**, 405–413 (1973).  
<https://doi.org/10.1007/BF02824484>.  
Cited on page 2.
- [12] **Particle Data Group** Collaboration, M. T. et al., “Review of Particle Physics,” *Phys. Rev. D* **98** (Aug, 2018) 030001.  
<https://link.aps.org/doi/10.1103/PhysRevD.98.030001>.  
Cited on page 3.
- [13] D. J. Gross and F. Wilczek, “Ultraviolet Behavior of Non-Abelian Gauge Theories,” *Phys. Rev. Lett.* **30** (Jun, 1973) 1343–1346.  
<https://link.aps.org/doi/10.1103/PhysRevLett.30.1343>.  
Cited on page 2.
- [14] H. D. Politzer, “Reliable Perturbative Results for Strong Interactions?,” *Phys. Rev. Lett.* **30** (Jun, 1973) 1346–1349.  
<https://link.aps.org/doi/10.1103/PhysRevLett.30.1346>.  
Cited on page 2.
- [15] H. David Politzer, “Asymptotic freedom: An approach to strong interactions,” *Physics Reports* **14** no. 4, (1974) 129–180.  
<https://www.sciencedirect.com/science/article/pii/0370157374900143>.  
Cited on page 2.
- [16] Ante Bilandzic, PhD Thesis, *Anisotropic Flow Measurements in ALICE at the Large Hadron Collider*. Utrecht University, 2012.  
Cited on pages 3, 10, 17, 58, 86, 87, and 88.
- [17] S. LEUPOLD, V. METAG, and U. MOSEL, “HADRONS IN STRONGLY INTERACTING MATTER,” *International Journal of Modern Physics E* **19** no. 02, (Feb, 2010) 147–224. <http://dx.doi.org/10.1142/S0218301310014728>.  
Cited on page 3.
- [18] S. Klimt, M. Lutz, and W. Weise, “Chiral phase transition in the SU(3) Nambu and Jona-Lasinio model,” *Physics Letters B* **249** no. 3, (1990) 386–390.  
<https://www.sciencedirect.com/science/article/pii/037026939091003T>.  
Cited on page 4.
- [19] E.V. Shuryak, *Theory of Hadronic Plasma*, vol. 27. Sov. Phys. JETP , 1978.  
Cited on page 4.

- [20] N. Itoh, “Hydrostatic Equilibrium of Hypothetical Quark Stars,” *Prog. Theor. Phys.* **44** (1970) 291.  
Cited on page 4.
- [21] D. M. Lee, “Probing the Big Bang at the Relativistic Heavy Ion Collider (RHIC) (or Probing the Big Bang 13.7 billion years later),” *Journal of Physics: Conference Series* **213** (Mar, 2010) 012012.  
<https://doi.org/10.1088/1742-6596/213/1/012012>.  
Cited on page 4.
- [22] S. M. Sanches, D. A. Fogaça, and F. S. Navarra, “The time evolution of the quark gluon plasma in the early Universe,” *Journal of Physics: Conference Series* **630** (Jul, 2015) 012028. <https://doi.org/10.1088/1742-6596/630/1/012028>.  
Cited on page 4.
- [23] E. Shuryak, “Strongly coupled quark-gluon plasma in heavy ion collisions,” *Rev. Mod. Phys.* **89** (Jul, 2017) 035001.  
<https://link.aps.org/doi/10.1103/RevModPhys.89.035001>.  
Cited on pages 4 and 7.
- [24] A. Chodos, R. L. Jaffe, K. Johnson, C. B. Thorn, and V. F. Weisskopf, “New extended model of hadrons,” *Phys. Rev. D* **9** (Jun, 1974) 3471–3495.  
<https://link.aps.org/doi/10.1103/PhysRevD.9.3471>.  
Cited on page 4.
- [25] W. Florkowski, *Phenomenology of Ultra-Relativistic Heavy-Ion Collisions*. 3, 2010.  
Cited on page 4.
- [26] **HotQCD** Collaboration, A. Bazavov, T. Bhattacharya, M. Cheng, C. DeTar, H.-T. Ding, S. Gottlieb, R. Gupta, P. Hegde, U. M. Heller, F. Karsch, E. Laermann, L. Levkova, S. Mukherjee, P. Petreczky, C. Schmidt, R. A. Soltz, W. Soeldner, R. Sugar, D. Toussaint, W. Unger, and P. Vranas, “Chiral and deconfinement aspects of the QCD transition,” *Phys. Rev. D* **85** (Mar, 2012) 054503. <https://link.aps.org/doi/10.1103/PhysRevD.85.054503>.  
Cited on page 4.
- [27] ALICE Collaboration, “Direct photon production in Pb–Pb collisions at  $\sqrt{s_{NN}}=2.76$  TeV,” *Physics Letters B* **754** (2016) 235–248.  
<https://www.sciencedirect.com/science/article/pii/S0370269316000320>.  
Cited on pages 4 and 5.
- [28] P. K. Kovtun, D. T. Son, and A. O. Starinets, “Viscosity in Strongly Interacting Quantum Field Theories from Black Hole Physics,” *Physical Review Letters* **94** no. 11, (Mar, 2005) . <http://dx.doi.org/10.1103/PhysRevLett.94.111601>.  
Cited on page 4.
- [29] Cindy Mordasini, PhD Thesis, *Generalisation of the Cumulants of Flow Amplitudes to the higher orders*. Technische Universität München, 2021.  
Cited on pages 5, 39, 49, 50, and 58.
- [30] **STAR** Collaboration, G. Odyniec, “Beam Energy Scan Program at RHIC (BES I and BES II) – Probing QCD Phase Diagram with Heavy-Ion Collisions,” *PoS CORFU2018* (2019) 151.  
Cited on page 4.

- [31] D. Tlusty, “The RHIC Beam Energy Scan Phase II: Physics and Upgrades,” 2018. Cited on page 4.
- [32] J. Brewer, A. Mazeliauskas, and W. van der Schee, “Opportunities of OO and  $pO$  collisions at the LHC,” 2021. Cited on page 4.
- [33] R. S. Bhalerao, “Collectivity in large and small systems formed in ultrarelativistic collisions,” *The European Physical Journal Special Topics* **230** no. 3, (Apr, 2021) 635–654. <http://dx.doi.org/10.1140/epjs/s11734-021-00019-x>. Cited on pages 5, 6, and 73.
- [34] W. Broniowski and W. Florkowski, “Geometric relation between centrality and the impact parameter in relativistic heavy-ion collisions,” *Physical Review C* **65** no. 2, (Jan, 2002) . <http://dx.doi.org/10.1103/PhysRevC.65.024905>. Cited on page 6.
- [35] Sourav Sarkar, Helmut Satz, Bikash Sinha, *The Physics of the Quark-Gluon Plasma*, vol. 785. Springer-Verlag Berlin Heidelberg, 2010. <https://doi.org/10.1007/978-3-642-02286-9>. Cited on page 7.
- [36] M. Luzum, “Flow fluctuations and long-range correlations: elliptic flow and beyond,” *Journal of Physics G: Nuclear and Particle Physics* **38** no. 12, (Nov, 2011) 124026. <http://dx.doi.org/10.1088/0954-3899/38/12/124026>. Cited on page 7.
- [37] M. L. Miller, K. Reygers, S. J. Sanders, and P. Steinberg, “Glauber Modeling in High-Energy Nuclear Collisions,” *Annual Review of Nuclear and Particle Science* **57** no. 1, (Nov, 2007) 205–243. <http://dx.doi.org/10.1146/annurev.nucl.57.090506.123020>. Cited on pages 7 and 21.
- [38] E. Iancu, “QCD in heavy ion collisions,” 2012. Cited on pages 7, 8, and 52.
- [39] P. Braun-Munzinger and B. Dönigus, “Loosely-bound objects produced in nuclear collisions at the LHC,” *Nuclear Physics A* **987** (Jul, 2019) 144–201. <http://dx.doi.org/10.1016/j.nuclphysa.2019.02.006>. Cited on pages 7 and 8.
- [40] U. W. Heinz, “The Strongly coupled quark-gluon plasma created at RHIC,” *J. Phys. A* **42** (2009) 214003, [arXiv:0810.5529](https://arxiv.org/abs/0810.5529) [nucl-th]. Cited on page 7.
- [41] A. Majumder and M. van Leeuwen, “The theory and phenomenology of perturbative QCD based jet quenching,” *Progress in Particle and Nuclear Physics* **66** no. 1, (2011) 41–92. <https://www.sciencedirect.com/science/article/pii/S0146641010000542>. Cited on page 9.
- [42] **JET** Collaboration, K. M. Burke, A. Buzzatti, N. Chang, C. Gale, M. Gyulassy, U. Heinz, S. Jeon, A. Majumder, B. Müller, G.-Y. Qin, B. Schenke, C. Shen, X.-N. Wang, J. Xu, C. Young, and H. Zhang, “Extracting the jet transport coefficient

- from jet quenching in high-energy heavy-ion collisions,” *Phys. Rev. C* **90** (Jul, 2014) 014909. <https://link.aps.org/doi/10.1103/PhysRevC.90.014909>.  
Cited on page 9.
- [43] J. Rafelski and B. Müller, “Strangeness Production in the Quark-Gluon Plasma,” *Phys. Rev. Lett.* **48** (Apr, 1982) 1066–1069.  
<https://link.aps.org/doi/10.1103/PhysRevLett.48.1066>.  
Cited on page 9.
- [44] L. Yan, “A flow paradigm in heavy-ion collisions,” *Chinese Physics C* **42** no. 4, (Apr, 2018) 042001. <http://dx.doi.org/10.1088/1674-1137/42/4/042001>.  
Cited on pages 9 and 12.
- [45] D. Teaney and L. Yan, “Triangularity and dipole asymmetry in relativistic heavy ion collisions,” *Physical Review C* **83** no. 6, (Jun, 2011) .  
<http://dx.doi.org/10.1103/PhysRevC.83.064904>.  
Cited on page 10.
- [46] D. Teaney and L. Yan, “Event-plane correlations and hydrodynamic simulations of heavy ion collisions,” *Physical Review C* **90** no. 2, (Aug, 2014) .  
<http://dx.doi.org/10.1103/PhysRevC.90.024902>.  
Cited on page 10.
- [47] D. Teaney and L. Yan, “Nonlinearities in the harmonic spectrum of heavy ion collisions with ideal and viscous hydrodynamics,” *Physical Review C* **86** no. 4, (Oct, 2012) . <http://dx.doi.org/10.1103/PhysRevC.86.044908>.  
Cited on page 10.
- [48] S. Taghavi, “A Fourier-cumulant analysis for multiharmonic flow fluctuation,” *Eur. Phys. J. C* **81**, **652** (July, 2021) .  
<https://doi.org/10.1140/epjc/s10052-021-09413-0>.  
Cited on pages 10 and 12.
- [49] A. M. Poskanzer and S. A. Voloshin, “Methods for analyzing anisotropic flow in relativistic nuclear collisions,” *Physical Review C* **58** no. 3, (Sep, 1998) 1671–1678.  
<http://dx.doi.org/10.1103/PhysRevC.58.1671>.  
Cited on pages 11 and 13.
- [50] B.-A. Li and A. T. Sustich, “Differential Flow in Heavy-Ion Collisions at Balance Energies,” *Physical Review Letters* **82** no. 25, (Jun, 1999) 5004–5007.  
<http://dx.doi.org/10.1103/PhysRevLett.82.5004>.  
Cited on page 11.
- [51] K. Aamodt, B. Abelev, A. Abrahantes Quintana, D. Adamová, A. M. Adare, M. M. Aggarwal, G. Aglieri Rinella, A. G. Agocs, S. Aguilar Salazar, Z. Ahammed, and et al. (ALICE Collaboration), “Elliptic Flow of Charged Particles in Pb-Pb Collisions at  $\sqrt{s_{NN}}=2.76$  TeV,” *Physical Review Letters* **105** no. 25, (Dec, 2010) . <http://dx.doi.org/10.1103/PhysRevLett.105.252302>.  
Cited on pages 11, 18, and 56.
- [52] N. Borghini, P. M. Dinh, and J.-Y. Ollitrault, “Flow analysis from multiparticle azimuthal correlations,” *Physical Review C* **64** no. 5, (Sep, 2001) .  
<http://dx.doi.org/10.1103/PhysRevC.64.054901>.  
Cited on pages 11, 16, 19, and 41.

- [53] M. Luzum and J.-Y. Ollitrault, “Eliminating experimental bias in anisotropic-flow measurements of high-energy nuclear collisions,” *Physical Review C* **87** no. 4, (Apr, 2013) . <http://dx.doi.org/10.1103/PhysRevC.87.044907>.  
Cited on page 13.
- [54] R. S. Bhalerao, M. Luzum, and J.-Y. Ollitrault, “Determining initial-state fluctuations from flow measurements in heavy-ion collisions,” *Physical Review C* **84** no. 3, (Sep, 2011) . <http://dx.doi.org/10.1103/PhysRevC.84.034910>.  
Cited on pages 13 and 14.
- [55] A. Bilandzic, C. H. Christensen, K. Gulbrandsen, A. Hansen, and Y. Zhou, “Generic framework for anisotropic flow analyses with multiparticle azimuthal correlations,” *Physical Review C* **89** no. 6, (Jun, 2014) .  
<http://dx.doi.org/10.1103/PhysRevC.89.064904>.  
Cited on pages 15, 16, 19, and 41.
- [56] P. Danielewicz and G. Odnycie, “Transverse Momentum Analysis of Collective Motion in Relativistic Nuclear Collisions,” *Phys. Lett. B* **157** (1985) 146,  
[arXiv:2109.05308](https://arxiv.org/abs/2109.05308) [nucl-th].  
Cited on page 16.
- [57] S. Voloshin and Y. Zhang, “Flow study in relativistic nuclear collisions by Fourier expansion of Azimuthal particle distributions,” *Z. Phys. C* **70** (1996) 665–672,  
[arXiv:hep-ph/9407282](https://arxiv.org/abs/hep-ph/9407282).  
Cited on page 16.
- [58] C. Mordasini, A. Bilandzic, D. Karakoç, and S. F. Taghavi, “Higher order symmetric cumulants,” *Physical Review C* **102** no. 2, (Aug, 2020) .  
<http://dx.doi.org/10.1103/PhysRevC.102.024907>.  
Cited on pages 17, 19, and 41.
- [59] A. Bilandzic, R. Snellings, and S. Voloshin, “Flow analysis with cumulants: Direct calculations,” *Physical Review C* **83** no. 4, (Apr, 2011) .  
<http://dx.doi.org/10.1103/PhysRevC.83.044913>.  
Cited on pages 17, 19, and 41.
- [60] N. Borghini, P. M. Dinh, and J.-Y. Ollitrault, “New method for measuring azimuthal distributions in nucleus-nucleus collisions,” *Physical Review C* **63** no. 5, (Apr, 2001) . <http://dx.doi.org/10.1103/PhysRevC.63.054906>.  
Cited on pages 17, 19, and 41.
- [61] Adam, J. et al. (ALICE Collaboration), “Correlated Event-by-Event Fluctuations of Flow Harmonics in Pb-Pb Collisions at  $\sqrt{s_{NN}}=2.76$  TeV,” *Physical Review Letters* **117** no. 18, (Oct, 2016) .  
<http://dx.doi.org/10.1103/PhysRevLett.117.182301>.  
Cited on pages 19, 56, 57, and 66.
- [62] Acharya, S. et al. (ALICE Collaboration), “Multiharmonic Correlations of Different Flow Amplitudes in Pb-Pb Collisions at  $\sqrt{s_{NN}}=2.76$  TeV,” *Physical Review Letters* **127** no. 9, (Aug, 2021) .  
<http://dx.doi.org/10.1103/PhysRevLett.127.092302>.  
Cited on pages 19 and 41.

- [63] **E877** Collaboration, J. e. a. Barrette, “Energy and charged particle flow in 10.8A GeV/c Au+Au collisions,” *Phys. Rev. C* **55** (Mar, 1997) 1420–1430.  
<https://link.aps.org/doi/10.1103/PhysRevC.55.1420>.  
Cited on page 19.
- [64] **PHENIX** Collaboration, S. e. a. Afanasiev, “Systematic studies of elliptic flow measurements in Au + Au collisions at  $\sqrt{s_{NN}} = 200$  GeV,” *Phys. Rev. C* **80** (Aug, 2009) 024909. <https://link.aps.org/doi/10.1103/PhysRevC.80.024909>.  
Cited on page 20.
- [65] **PHENIX** Collaboration, A. e. a. Adare, “Measurements of Higher Order Flow Harmonics in Au + Au Collisions at  $\sqrt{s_{NN}} = 200$  GeV,” *Phys. Rev. Lett.* **107** (Dec, 2011) 252301.  
<https://link.aps.org/doi/10.1103/PhysRevLett.107.252301>.  
Cited on page 20.
- [66] **ALICE** Collaboration, K. e. a. Aamodt, “Higher Harmonic Anisotropic Flow Measurements of Charged Particles in Pb-Pb Collisions at  $\sqrt{s_{NN}} = 2.76$  TeV,” *Phys. Rev. Lett.* **107** (Jul, 2011) 032301.  
<https://link.aps.org/doi/10.1103/PhysRevLett.107.032301>.  
Cited on page 20.
- [67] **ATLAS** Collaboration, G. e. a. Aad, “Measurement of event-plane correlations in  $\sqrt{s_{NN}} = 2.76$  TeV lead-lead collisions with the ATLAS detector,” *Phys. Rev. C* **90** (Aug, 2014) 024905. <https://link.aps.org/doi/10.1103/PhysRevC.90.024905>.  
Cited on pages 20, 34, 63, 103, 104, 105, and 106.
- [68] J. Jia, “Measurement of Event Plane Correlations in Pb–Pb Collisions at  $\sqrt{s_{NN}}=2.76$ TeV with the ATLAS Detector,” *Nuclear Physics A* **910-911** (2013) 276–280.  
<https://www.sciencedirect.com/science/article/pii/S0375947412003661>.  
Hard Probes 2012.  
Cited on page 20.
- [69] S. Mohapatra, “Measurement of vn coefficients and event plane correlations in 2.76 TeV Pb–Pb collisions with ATLAS,” *Nuclear Physics A* **910-911** (2013) 75–82.  
<https://www.sciencedirect.com/science/article/pii/S0375947412003879>.  
Hard Probes 2012.  
Cited on page 20.
- [70] Adler, C. et al. (STAR Collaboration), “Elliptic flow from two- and four-particle correlations in Au+Au collisions at  $\sqrt{s_{NN}} = 130$ GeV,” *Phys. Rev. C* **66** (Sep, 2002) 034904. <https://link.aps.org/doi/10.1103/PhysRevC.66.034904>.  
Cited on pages 20 and 34.
- [71] R. S. Bhalerao, J.-Y. Ollitrault, and S. Pal, “Event-plane correlators,” *Phys. Rev. C* **88** (Aug, 2013) 024909.  
<https://link.aps.org/doi/10.1103/PhysRevC.88.024909>.  
Cited on pages 20 and 34.
- [72] A. Bilandzic, M. Lesch, and S. F. Taghavi, “New estimator for symmetry plane correlations in anisotropic flow analyses,” *Physical Review C* **102** no. 2, (Aug, 2020) . <http://dx.doi.org/10.1103/PhysRevC.102.024910>.  
Cited on pages 20, 25, 33, 34, 38, 71, and 77.

- [73] S. Acharya et al. (ALICE Collaboration), “Linear and non-linear flow mode in Pb–Pb collisions at  $\sqrt{s_{NN}}=2.76$  TeV,” *Physics Letters B* **773** (2017) 68–80.  
<https://www.sciencedirect.com/science/article/pii/S0370269317306160>.  
Cited on page 20.
- [74] H. Petersen, G.-Y. Qin, S. A. Bass, and B. Müller, “Triangular flow in event-by-event ideal hydrodynamics in Au+Au collisions at  $\sqrt{s_{NN}}=200$  AGeV,” *Physical Review C* **82** no. 4, (Oct, 2010) .  
<http://dx.doi.org/10.1103/PhysRevC.82.041901>.  
Cited on page 22.
- [75] M. Lesch, “Symmetry-Planes Correlations in Flow Analyses,” 2019.  
[https://www.das.ktas.ph.tum.de/DasDocs/Public/Bachelor\\_Theses/MarcelLesch\\_bachelor.pdf](https://www.das.ktas.ph.tum.de/DasDocs/Public/Bachelor_Theses/MarcelLesch_bachelor.pdf). Bachelor thesis.  
Cited on pages 22, 33, 34, and 38.
- [76] ALICE Collaboration, “Centrality determination in heavy ion collisions,”  
<http://cds.cern.ch/record/2636623>.  
Cited on pages 22, 23, and 24.
- [77] C. Shen, Z. Qiu, H. Song, J. Bernhard, S. Bass, and U. Heinz, “The iEBE-VISHNU code package for relativistic heavy-ion collisions,” 2015.  
Cited on pages 22 and 24.
- [78] J. S. Moreland, J. E. Bernhard, and S. A. Bass, “Alternative ansatz to wounded nucleon and binary collision scaling in high-energy nuclear collisions,” *Physical Review C* **92** no. 1, (Jul, 2015) .  
<http://dx.doi.org/10.1103/PhysRevC.92.011901>.  
Cited on page 23.
- [79] P. Huovinen and P. Petreczky, “QCD equation of state and hadron resonance gas,” *Nuclear Physics A* **837** no. 1-2, (Jun, 2010) 26–53.  
<http://dx.doi.org/10.1016/j.nuclphysa.2010.02.015>.  
Cited on page 24.
- [80] F. Cooper and G. Frye, “Single-particle distribution in the hydrodynamic and statistical thermodynamic models of multiparticle production,” *Phys. Rev. D* **10** (Jul, 1974) 186–189. <https://link.aps.org/doi/10.1103/PhysRevD.10.186>.  
Cited on page 24.
- [81] S. Bass, “Microscopic models for ultrarelativistic heavy ion collisions,” *Progress in Particle and Nuclear Physics* **41** (1998) 255–369.  
[http://dx.doi.org/10.1016/S0146-6410\(98\)00058-1](http://dx.doi.org/10.1016/S0146-6410(98)00058-1).  
Cited on page 24.
- [82] M. Bleicher, E. Zabrodin, C. Spieles, S. A. Bass, C. Ernst, S. Soff, L. Bravina, M. Belkacem, H. Weber, H. Stöcker, and et al., “Relativistic hadron-hadron collisions in the ultra-relativistic quantum molecular dynamics model,” *Journal of Physics G: Nuclear and Particle Physics* **25** no. 9, (Sep, 1999) 1859–1896.  
<http://dx.doi.org/10.1088/0954-3899/25/9/308>.  
Cited on page 24.

- [83] J. E. Bernhard, J. S. Moreland, and S. A. Bass, “Bayesian estimation of the specific shear and bulk viscosity of quark–gluon plasma,” *Nature Phys.* **15** no. 11, (2019) 1113–1117.  
Cited on page 25.
- [84] X.-N. Wang and M. Gyulassy, “hijing: A Monte Carlo model for multiple jet production in pp, pA, and AA collisions,” *Phys. Rev. D* **44** (Dec, 1991) 3501–3516.  
<https://link.aps.org/doi/10.1103/PhysRevD.44.3501>.  
Cited on page 25.
- [85] M. Gyulassy and X.-N. Wang, “HIJING 1.0: A Monte Carlo program for parton and particle production in high energy hadronic and nuclear collisions,” *Computer Physics Communications* **83** no. 2-3, (Dec, 1994) 307–331.  
[http://dx.doi.org/10.1016/0010-4655\(94\)90057-4](http://dx.doi.org/10.1016/0010-4655(94)90057-4).  
Cited on page 25.
- [86] CERN Press Office, “CERN Accelerating science,” 2017.  
<https://home.cern/resources/brochure/cern/lhc-guide>.  
Cited on page 27.
- [87] R. Aßmann, M. Lamont, and S. Myers, “A brief history of the LEP collider,” *Nuclear Physics B - Proceedings Supplements* **109** no. 2, (2002) 17–31.  
<https://www.sciencedirect.com/science/article/pii/S0920563202900058>.  
Proceedings of the 7th Topical Seminar.  
Cited on page 27.
- [88] **ALICE** Collaboration, P. Cortese *et al.*, “ALICE: Physics performance report, volume I,” *J. Phys. G* **30** (2004) 1517–1763.  
Cited on pages 28, 30, and 31.
- [89] **ALICE** Collaboration, C. W. Fabjan *et al.*, “ALICE: Physics performance report, volume II,” *J. Phys. G* **32** (2006) 1295–2040.  
Cited on page 28.
- [90] “3D ALICE Schematic RUN2 - with Description.”  
<https://alice-figure.web.cern.ch/>.  
Cited on page 29.
- [91] **ALICE** Collaboration, K. Aamodt *et al.*, “Alignment of the ALICE Inner Tracking System with cosmic-ray tracks,” *JINST* **5** (2010) P03003,  
arXiv:1001.0502 [physics.ins-det].  
Cited on page 30.
- [92] **ALICE TPC** Collaboration, P. Gasik, “Development of GEM-based Read-Out Chambers for the upgrade of the ALICE TPC,” *JINST* **9** (2014) C04035.  
Cited on page 31.
- [93] **ALICE TPC** Collaboration, M. Aggarwal *et al.*, “Particle identification studies with a full-size 4-GEM prototype for the ALICE TPC upgrade,” *Nucl. Instrum. Meth. A* **903** (2018) 215–223, arXiv:1805.03234 [physics.ins-det].  
Cited on page 31.

- [94] **E877** Collaboration, J. Barrette *et al.*, “Observation of anisotropic event shapes and transverse flow in Au + Au collisions at AGS energy,” *Phys. Rev. Lett.* **73** (1994) 2532–2535, [arXiv:hep-ex/9405003](https://arxiv.org/abs/hep-ex/9405003).  
Cited on page 34.
- [95] S. A. Voloshin, A. M. Poskanzer, A. Tang, and G. Wang, “Elliptic flow in the Gaussian model of eccentricity fluctuations,” *Phys. Lett. B* **659** (2008) 537–541, [arXiv:0708.0800](https://arxiv.org/abs/0708.0800) [nucl-th].  
Cited on page 34.
- [96] R. Kubo, “Generalized Cumulant Expansion Method,” *Journal of the Physical Society of Japan* **17** no. 7, (1962) 1100–1120.  
Cited on page 39.
- [97] A. Bilandzic, M. Lesch, C. Mordasini, and S. F. Taghavi, “Multivariate cumulants in flow analyses: The Next Generation,” 2021.  
Cited on pages 39, 41, 42, 44, 45, and 79.
- [98] P. Bonnier and H. Oberhauser, “Signature cumulants, ordered partitions, and independence of stochastic processes,” *Bernoulli* **26** no. 4, (2020) 2727 – 2757.  
<https://doi.org/10.3150/20-BEJ1205>.  
Cited on page 40.
- [99] Toia, Alberica (ALICE Collaboration), “Bulk properties of Pb–Pb collisions at  $\sqrt{s_{NN}}=2.76$  TeV measured by ALICE,” *Journal of Physics G: Nuclear and Particle Physics* **38** no. 12, (Nov, 2011) 124007.  
<http://dx.doi.org/10.1088/0954-3899/38/12/124007>.  
Cited on page 49.
- [100] G. Cowan, *Statistical Data Analysis*. Clarendon (Oxford), Oxford, 1998 (ISBN: 0-19-850156-0 or 0-19-850155-2 in paperback).  
Cited on pages 58, 60, 75, 85, and 87.
- [101] R. J. Barlow, *Statistics: A Guide to the Use of Statistical Methods in the Physical Sciences (Manchester Physics Series)*. WileyBlackwell, reprint ed., 1989.  
Cited on page 60.
- [102] R. Barlow, “Systematic errors: Facts and fictions,” in *Conference on Advanced Statistical Techniques in Particle Physics*, pp. 134–144. 2002.  
[arXiv:hep-ex/0207026](https://arxiv.org/abs/hep-ex/0207026).  
Cited on page 60.
- [103] Z. Qiu and U. Heinz, “Event-by-event shape and flow fluctuations of relativistic heavy-ion collision fireballs,” *Physical Review C* **84** no. 2, (Aug, 2011) .  
<http://dx.doi.org/10.1103/PhysRevC.84.024911>.  
Cited on page 64.
- [104] J. Jia and S. Mohapatra, “A method for studying initial geometry fluctuations via event plane correlations in heavy ion collisions,” *The European Physical Journal C* **73** no. 7, (Jul, 2013) . <http://dx.doi.org/10.1140/epjc/s10052-013-2510-y>.  
Cited on pages 64 and 65.

# Acknowledgements

Firstly, I would like to thank my supervisor and head of the “MuPa” group, Dr. Ante Bilandzic. Four years ago, he introduced me to the world of heavy-ion collisions and flow. It has been a long road, a lot to learn and there is still a lot ahead. But in this time, I got the amazing chance to be part of two papers with the next one already in the pipeline. For all of these great opportunities, the fruitful discussions, his help and all the great advise (“Do your thing”, “Never seek perfection”, ... ), I want to greatly thank him.

Next, I would like to thank my “teammate”, Dr. Cindy Mordasini. It goes without saying that the analysis wouldn’t have reached its current status without her hard earned experience from her PhD that she shared with me. All the amazing discussions we had and our great teamwork really deserve a big thanks.

Continuing this list, I want to thank Dr. Seyed Farid Taghavi for all the great discussions and the work we did together on the Gaussian Estimator. And in particular for all the model data he always provides to me. For all this help and everything I learned from him also a big thanks.

I also would like to thank Dr. Dong Jo Kim for all his help in the analysis, in particular with setting up the JCorran framework, the implementation of the corrections maps and all the great discussions we had so far.